

TOWARDS MULTI-WAVELENGTH OBSERVATIONS OF RELATIVISTIC JETS
FROM GENERAL RELATIVISTIC MAGNETOHYDRODYNAMIC
SIMULATIONS

A DISSERTATION
SUBMITTED TO THE DEPARTMENT OF PHYSICS
AND THE COMMITTEE ON GRADUATE STUDIES
OF STANFORD UNIVERSITY
IN PARTIAL FULFILLMENT OF THE REQUIREMENTS
FOR THE DEGREE OF
DOCTOR OF PHILOSOPHY

Richard Jude Anantua
August 2016

Abstract

A methodology for reverse engineering current and anticipated observations of astrophysical relativistic jets using self-consistent, general relativistic magnetohydrodynamic (GRMHD) simulations is detailed from data-hosting and manipulation to mimicking instrument-specific properties such as point spread function convolution. This pipeline handles particle acceleration prescriptions, synchrotron and inverse Compton emission and absorption, Doppler boosting, time-dependent transfer of polarized radiation and light-travel time effects. Application of this pipeline to low-frequency radio observations is exemplified using the famous jet in the giant elliptical galaxy M87. High-frequency gamma-ray observations are represented by the powerful quasar 3C 279. Though the work presented here focuses on a single simulation of a magnetically arrested disk and a wind-collimated, approximately force-free jet, it can readily be adapted to simulations with different spatiotemporal resolutions and/or plasma initial conditions. Stationary, axisymmetric semi-analytic models are also developed, providing a quantitative understanding of the simulated jet flow and its electromagnetic properties. Using the 3D time-dependent “observing” routines for synchrotron models, predictions such as bilateral asymmetry of intensity maps and enhanced limb brightening for models with high velocity shear are advanced. Using gamma ray prescriptions in the routines resulted in rapid variability. User-friendly Python and UNIX guides are included for didactic purposes. With the advent of the state-of-the-art gamma ray Cerenkov Telescope Array, the Event Horizon Telescope– which promises to resolve Schwarzschild radius (r_S) scale features at the Galactic Center and M87– and more sophisticated GRMHD simulations with similar resolution coupled with dynamical range $10^0 r_S$ – $10^5 r_S$, direct comparison of simulation and observation in this work may facilitate the understanding and prediction of the physical nature of relativistic jets in the near future.

Acknowledgments

Stanford is a uniquely amazing, amazingly unique place. Where else can you take classes from Fields medalists and Nobel laureates in the same semester as going to college football home games that matter? Stanford is also a place of apparent contradictions. At times such as teaching Ph 17 Black Holes to non-physics majors, I have witnessed the institution transcend its self-adopted techy/fuzzy dichotomy, hosting both under the same roof. The longer I am a member of the Stanford community, the better I am able to make sense of these facts by subsuming them within the Stanford Philosophy (Dorde Radicevic already coined the term “Stanford Model” at our commencement): to re-imagine what is possible. The reality still stands that not many U.S. academic institutions enlist students from less advantaged backgrounds to work towards the physics Ph.D. alongside the world’s leading experts. I am immensely grateful that Stanford has given me the opportunity to offer my thesis as part of its long legacy of finding achievement in places few others could imagine.

First of all, I would like to thank my mother, Bernadette Anantua. By simply reminding me to feed and clothe myself, you contributed to my academic performance more than any other. A special shout goes out to Kate Alper, whose loving support changed my life.

Among the people who contributed directly to this work, my supportive research group members Yajie Yuan, Paul Simeon and Adviser Roger Blanford have enabled me to complete a doctorate in 5 years and go on to UC Berkeley— a position that would have been unthinkable without their help. I thank my committee, Steve Allen, Greg Madejski, Peter Michleson, Vahe Petrosian and Reginald Mitchell, for holding my dissertation to the highest standard. I sincerely thank Roman Sherbakov for his patient guidance while I was an incipient programmer, as well as collaborators Jonathan McKinney and Alexander Tchekhovskoy. I thank Ramesh Narayan for his mentorship during my course at the Harvard-Smithsonian Center for Astrophysics. I am deeply grateful to fellow astrophysics Ph.D. Robert Moffatt for thesis formatting tips and being a good friend.

I also thank my friends Danjie Wenren, Jonathan Maltz and Victoria Martin back in SITP for being cool people to talk, lift or otherwise hang out with.

Finally, I gratefully acknowledge the sponsorship offered by the Stanford Humanities and Sciences (H&S), Achievement Rewards for College Scientists (ARCS) and Diversifying Academia, Recruiting Excellence (DARE) Fellowships.

Contents

Abstract	iv
Acknowledgments	v
1 Introduction	1
1.1 Historical Considerations	1
1.1.1 Active Galactic Nuclei	1
1.1.2 Gamma Ray Bursts	3
1.1.3 Black Hole X-Ray Binaries	3
1.1.4 Theory	3
1.2 Current Observations	4
1.3 Looking Forward	6
1.3.1 Cherenkov Array Telescope	6
1.3.2 Event Horizon Telescope	6
1.3.3 Observing Jet Simulations	7
1.3.4 This Thesis	8
2 Radiative Processes	10
2.1 Synchrotron Radiation and Gas Dynamics	10
2.1.1 Synchrotron Self-Absorption	12
2.1.2 Polarization of Synchrotron Radiation	13
2.1.3 Polarized Radiative Transfer Equations with Opacity	18
2.2 Equipartition of Energy	19
2.3 Inverse Compton Radiation	20
2.3.1 Single-Electron Case	20
2.3.2 Multi-Electron Population Case	20
2.3.3 Klein-Nishina Regime	22
2.3.4 Pair Production	24

3	3D General Relativistic Magnetohydrodynamic Simulations	26
3.1	Idumps Investigations	26
3.2	General Relativistic Magnetohydrodynamic Equations	28
3.2.1	Simulation Kinematic and Dynamic Variables	29
3.3	Code Coordinates to Physical Units	40
3.3.1	Relating Quantities to the Black Hole for Particle Jet	40
3.3.2	Relating Quantities to the Black Hole for Electromagnetic Jet	42
3.4	Inner vs. Outer Jet Simulations	43
4	Self-Similar Stationary Axisymmetric Model	44
4.1	Reference Case: $z=50M$	45
4.2	Near the Hole: $z=10M-100M$	48
4.3	Outer Jet: Beyond $100M$	48
4.3.1	Velocity Field: Bead on a Wire	49
4.4	Observing Self-Similar Model	49
5	Emission, Particle Acceleration and Dissipation	52
5.1	Synchrotron Emissivity Prescriptions	52
5.1.1	Beta Model	53
5.1.2	Bias Model: Scaling Gas Pressure to Powers of Magnetic Field	53
5.2	Synchrotron Particle Acceleration Prescriptions with Dissipation	54
5.2.1	Alpha Model	54
5.2.2	Velocity Gradient Model	56
5.2.3	Current Density Model	57
5.2.4	Synchrotron Prescription in Convenient Observational Units	58
5.3	Inverse Compton Prescriptions	59
6	Radiative Transfer and Imaging Pipeline	61
6.1	Solving Radiative Transfer Equation	61
6.2	Interpolation	63
6.3	Adding an Observer	64
6.4	Image-Making Procedure	64
6.4.1	C and C++ Routines	64
6.4.2	Mathematica Routines	68
6.5	Connecting with Observation	69
6.5.1	Superluminal Motion	69
6.6	Instrumentation and Convolution	71

7	Application I. Comparison with M87	72
7.1	M87 - Prototypical Unbeamed BL-Lac	72
7.1.1	Radio Observations of M87	73
7.2	Comparing Simulated Intensity Maps with Observations	74
7.2.1	Collimation	74
7.2.2	Comparing Simulation and Observation Scales	74
7.2.3	Comparing Prescriptions with Dissipation	78
7.3	Comparison with Polarization Observations	81
8	Application II. Comparison with 3C 279	85
8.1	3C 279 - Flat Spectrum Radio Quasar	85
8.1.1	Accretion Disk	85
8.1.2	Spectrum and Variability	86
8.1.3	Superluminal Motion	86
8.2	Absorption and Emission Processes in 3C 279	87
8.2.1	Pair Production Opacity	87
8.2.2	Inverse Compton Scenario	88
8.2.3	Synchrotron Scenario	90
8.3	3C 279 Gamma Ray Models	91
8.4	Alternative Emission Mechanisms	93
9	Data Analysis	95
9.1	Stationary Axisymmetric Model from Velocity and Magnetic Field Fits	98
9.2	Individual Source Statistics	101
9.2.1	Radio versus Gamma-Ray Light Curves	101
9.2.2	Stationarity	101
9.3	Survey Statistics	102
9.3.1	Azimuthal Variation and Averages	102
9.3.2	Polar Variation	103
9.3.3	Flux Limited Samples	104
10	Future Directions	106
10.1	Observing Accretion Disk Simulations	106
10.2	Incorporating General Relativity into Radiative Transfer	107
10.3	Mrk 421 - Beamed Version of M87	107
10.4	Observing Jet Simulations To-Do List	108
10.5	What's Next?	108

A	Checks of Observing Jet Simulations Computational Pipeline	110
A.1	Projection of Doppler Factor Test	110
B	UNIX and Python Guides for Observing Jet Simulations	113
B.1	UNIX Guide for Observing Jet Simulations	114
B.2	Python Guide for Observing Jet Simulations	125

List of Tables

1	Datablock Size Specification	27
2	File Formats for Datablocks on Remote Server	27
3	egs Unit Conversions Based on $M \equiv M_{\text{M87}} = 6.6 \cdot 10^9 M_{\odot}$ and Fundamental Constants	41
4	Unit Conversions for Simulation Outputs	41
5	Convenient Conversions for Simulation Inputs	42
6	Convenient Conversions for EM Jet Simulation Inputs	42
1	M87 Dimensions	73
2	M87 Location and Orientation	73
3	Code Scale M to Physical Units for M87	73
1	Common UNIX Commands	115
2	More UNIX Commands	116

List of Figures

1.1	Cygnus A	2
1.2	M87 43GHz VLA Jet and Counterjet Observation	4
1.3	3C 279 Gamma Ray Variability	5
1.4	Observing Jet Simulations Analysis Pipeline	9
2.1	Synchrotron Emission Isocontours	11
2.2	Synchrotron Emission and Absorption p-Dependence	16
2.3	Polarization Axes on the Sky	17
2.4	Inverse Compton Scattering Setup	21
2.5	Inverse Compton Scattering in Different Frames	23
3.1	Simulation Outputs on Equatorial Plane at $T_{Gal}=1500M$	31
3.2	Simulation Outputs on Equatorial Plane at $T_{Gal}=2000M$	31
3.3	Simulation Outputs on $z=50M$ Plane at $T_{Gal}=2000M$	32
3.4	Transverse Variation of ρ , at $z=25M$ at $T=2000M$ and $2500M$	32
3.5	Simulation Outputs on Longitudinal Plane at $T_{Gal}=2000M$	33
3.6	Simulation Outputs on Longitudinal Plane at $T_{Gal}=2500M$	34
3.7	Transverse Variation of v_z at $T=2000M$ at $z=25M$, $50M$ and $z=75M$	34
3.8	Transverse Variation of ρ , v_z and B_z at $z=100M$	35
3.9	Lorentz Factor On Longitudinal Plane	36
3.10	IDumps 1 Velocity Field	36
3.11	Doppler Factor On Longitudinal Planes	37
3.12	3D Vector Plot of Magnetic Field	37
3.13	Velocity Field 3D Plots	38
3.14	Lab Frame Magnetic Field Component Plots	39
3.15	Square of Curl B	39
3.16	Z-Component of Curl B	40
4.1	Electric and Magnetic Field Variation with s in Self-Similar Model	46

4.2	Magnetic Flux, Fieldline Angular Speed, Current and Voltage Variation with s in Self-Similar Model	47
4.3	Poynting Flux, GEM and LEM Variation with s in Self-Similar Model	47
4.4	Streamplot of Magnetic Field between 10M and 100M in Self-Similar Model	48
4.5	Streamplot of Magnetic Field between 100M and 1000M in Self-Similar Model	48
4.6	Streamplot of Magnetic Field between 100M and 1000M in Self-Similar Model	49
4.7	Polarization Map between 0 mas and 1 mas in Self-Similar Model	50
4.8	Polarization Map between 0 mas and 10 mas in Self-Similar Model	50
4.9	Convolved Intensity Map between 0 mas and 10 mas in Self-Similar Model	51
5.1	Simulation Gas to Magnetic Pressure	53
5.2	Alpha Model Spectral Pressure Profile	56
5.3	Velocity Gradient Model Spectral Pressure Profile	57
5.4	Current Density Model Spectral Pressure Profile	58
6.1	Geometry for Optically Thin Polarization Ray Tracing	63
6.2	Rotating Observer Plane with Lines of Sight	65
6.3	Rotating Observer Coordinates.	66
6.4	BSqToThreeFourths Intensity Map	66
6.5	Jet Isolation Isocontours	67
6.6	Mathematica ArrayPlot and DensityPlot Formats	69
6.7	Superluminal Projection Geometry	70
6.8	Moving Blob	70
6.9	Convolved Intensity Map	71
7.1	Simulated Bias and Beta Model Intensity Maps	74
7.2	M87 43GHz VLA Observation	77
7.3	Alpha, Shear and Current Density Models	79
7.4	243 GHz JSq Model Intensity Map	80
7.5	Synchrotron Self-Absorbed Intensity Map	81
7.6	Model Jet EHT Base at 243 GHz and 345 GHz.	81
7.7	VLA M87 Electric Field Map	82
7.8	Simulation Q and U Maps To One-Third	83
7.9	Simulation Q and U Maps	84
8.1	Quasar 3C 279	87
8.2	Opacity Integrand Term and Analytic Approximation	88
8.3	Optical Depth vs. Altitude and Energy	89
8.4	Inverse Compton Geometry for 3C 379	90

8.5	Inverse Compton Simulated Light Curves Alpha and JSq Models Midcut 70M	92
8.6	Inverse Compton Light Curve for Alpha Model Midcut 210M	92
8.7	Synchrotron Light Curve for Alpha Model Midcut 210M	93
9.1	Azimuthal Averages T=2000M, z=50M	96
9.2	Azimuthal Averages T=2000M, z=100M	96
9.3	Azimuthal Averages T=2100M, z=50M	97
9.4	Azimuthal Averages T=2100M, z=100M	97
9.5	B Field Azimuthal Averages T=2000M, z=50M in Cylindrical Coordinates	99
9.6	Velocity Azimuthal Averages T=2000M,2100M, z=50M Cylindrical Coordinates . .	100
9.7	Fieldline Angular Speed Variation with s in Semi-Analytic Model	100
9.8	Temporal Averages	102
9.9	Azimuthal Variation 0Deg, 90Deg, 180Deg and 270Deg	103
9.10	Vector Plots of Magnetic Field	104
9.11	Polar Variation 15Deg to 20Deg	104
A.1	Projection of spherical Gaussian Emissivity with Hubble Expansion Velocity Field .	111
A.2	Projection of Constant Emissivity with Hubble expansion velocity field	111
A.3	Ellipsoidal Gaussian Data Projection	112
A.4	Numerical Lorentz Factor Test	112
B.1	Syntax for UNIX Commands	115
B.2	UNIX File Structure	116
B.3	Opening rt file using Midnight Commander	120
B.4	Opening win_lin_Jon.c file using Midnight Commander	120
B.5	Inside win_lin_Jon.c	121
B.6	Saving file with Midnight Commander	121
B.7	Directories within Midnight Commander	122
B.8	Modifying File within Midnight Commander	122
B.9	Saving Modified File within Midnight Commander	123
B.10	Cart3D.Py Code	127
B.11	Directory Structure for Python Movie	128
B.12	Terminal Code for Running Python Movie	129
B.13	Python Jet Movie	130
B.14	Python File Reading	131
B.15	Running Toy.py	132
B.16	Reading File Header Python	133
B.17	Reading File Body Python	134

B.18 Matplotlib Contour Plot Code Part 1	135
B.19 Matplotlib Contour Plot Code Part 2	135
B.20 Matplotlib Contour Plot Code Part 3	136

Chapter 1

Introduction

1.1 Historical Considerations

1.1.1 Active Galactic Nuclei

Rapidly rotating, magnetized, supermassive black holes are thought to be the engine driving the most energetic and among the highest power phenomena in the observable universe: jets from Active Galactic Nuclei (AGN). AGN are compact regions ($r \lesssim 1\text{kpc}$) of galactic centers that dominate the radiation from the galaxy at some energy bands due to supernova remnant shocks, wind, stellar activity or black hole accretion.¹ Approximately 10% of AGN host jets, which are bipolar outflows of relativistic particles whose emission is enhanced at small viewing angle θ from the jet axis by powers of the special relativistic Doppler factor $\mathcal{D} = (\gamma(1 - \frac{v}{c} \cos \theta))^{-1}$. The first known observation distinguishing an AGN from its host galaxy was made of the Seyfert galaxy M77 (Messier Catalog source N.G.C. 1068) during the spectroscopic research of graduate student Edward Fath in 1908 at the University of California Lick Observatory. In 1918, Heber Curtis, again from the University of California Lick Observatory, recorded the first observation of a jet from an AGN, as he described the Messier catalog source N.G.C. 4486 ($\alpha = 12\ 25.8$, $\delta = +12\ 57$)—more commonly known as M87—as follows

Exceedingly bright; the sharp nucleus shows well in 5^m exposure. The brighter central portion is about 0f5 in diameter, and the total diameter is about 2'; nearly round. No spiral structure is discernable. A curious ray lies in a gap in the nebulosity in p.a., 20°, apparently connected with the nucleus by a thin line of matter. The ray is brightest at its inner end, which is 11" from the nucleus. 20a.u. [18] .

Cygnus A (3C 405) (see Figure 1.1), discovered by Grote Reber in 1939, was identified as the first double radio source during the interferometry experiments by Roger Jennison and Mrinal Kumar

¹In this work, we are only concerned with the last kind, and understand AGN to refer to those powered by black hole.

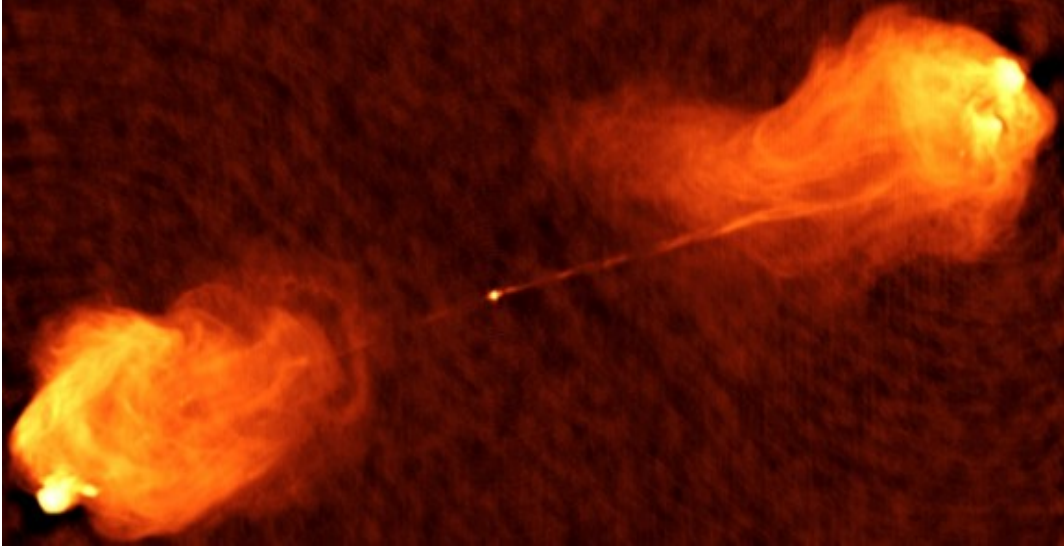


Figure 1.1: Double radio source Cygnus A as seen by the Very Large Array (VLA) at 5 GHz. The source is 230 Mpc away and the extent of the image is $0.0383^\circ \times 0.0217^\circ$ (154 kpc x 87 kpc). Though Cygnus A has the appearance of a pair of explosions, the source was correctly interpreted as the continuous injection of energy to the outer lobes by a central engine. Image courtesy of the National Radio Astronomy Observatory/Associated Universities, Inc. (NRAO/AUI).

(M. K.) Das Gupta in 1953. However, the origin of the source was misinterpreted as the collision of two galaxies. Our modern understanding of AGN jets as extended radio sources powered by the nucleus that accelerate particles along the jet axis originated with Martin Rees in 1971 [47].

Since then, observations of AGN jets have proliferated. The Roentgen Satellite (ROSAT) All-Sky Survey has correlated 843 X-ray sources with distinct radio sources seen by the Karl Jansky Very Large Array (VLA), including 146 quasars and 71 BL Lacs [14]. The *Fermi* Gamma-ray Space Telescope's 2015 3rd Catalog (3FGL)[3] has a corresponding catalog from Caltech's Owens Valley Radio Observatory (OVRO) 40-mm telescope radio survey[49] of 1200 AGN blazars (BL Lacertae objects and optically violent variable quasars)². Gamma ray observations of AGN can probe the highest energy cosmic ray phenomena known, potentially with implications for fundamental physics. For example, the spectrum of TeV gamma rays from distant BL-Lacs may indicate the existence of Beyond the Standard Model axion particles [5].

²Many of the sources in the *Fermi* catalog were previously included in the all-sky map collected by the Energetic Gamma Ray Experiment Telescope (*EGRET*)[57] from 1991-2000, though many more, such as J1350-1140 were not [56].

1.1.2 Gamma Ray Bursts

Gamma ray bursts can output greater power— albeit over a shorter time— than AGN jets. The first direct detection of GRBs occurred serendipitously in 1967 when the US launched the Vela satellites in the Cold War to detect Soviet nuclear weapons tests.

GRBs neatly fall into two categories: short burst GRBs typically lasting tens of ms and long burst GRBs typically lasting for hours. The progenitors of long burst GRBs are massive ($\geq 8M_{\odot}$) stars before they collapse into compact objects (white dwarfs, neutron stars or black holes) in supernovae. Short burst GRBs are believed to be produced by the merging of pairs of neutron stars.

1.1.3 Black Hole X-Ray Binaries

Black hole X-ray binaries are the third known source of relativistic jets. These sources are often categorized as low mass x-ray binaries (LMXB) or high-mass (HMXB). LMXBs are thought to form when a compact object is orbited by a star. HMXBs are formed when a member of an ordinary stellar binary undergoes a supernova event and becomes a compact object. The compact object then accretes the other star and the resulting accretion disk can power relativistic jets. Black hole X-ray binaries in the Milky Way such as GRS 1915+105 are also known as galactic superluminals (GSL). GSLs can be conceptualized as mini-AGN jets within our galaxy.

1.1.4 Theory

In 1977, magnetized accretion flows onto spinning black holes were theorized to provide relativistic jets power proportional to the square of the poloidal flux threading the horizon and the square of black hole spin through the Blandford-Znajek (BZ) mechanism [11]— an instance of theory lagging long after observation. The BZ mechanism is a natural explanation of most relativistic AGN jets because of the ubiquity of black hole accretion disks in the form of thick magnetized tori, which can interact with the black hole spin near the centers of massive galaxies to provide (a theoretical maximum) energy equal to $\sim 29\%$ of the rest mass energy of the black hole to power stable relativistic jets. Competing theories for jet formation have been advanced, but have not been as credible or widely applicable. For example, Roger Penrose showed that particles bound in negative (relativistic) energy orbits in the ergoregion (bounded by the outer Kerr horizon and the ergosphere circumscribing it) can extract rotational energy from the black hole. But because the production or transport of such a particle population within the ergosphere remains mysterious, there are no widely accepted models of relativistic jet formation via Penrose process.

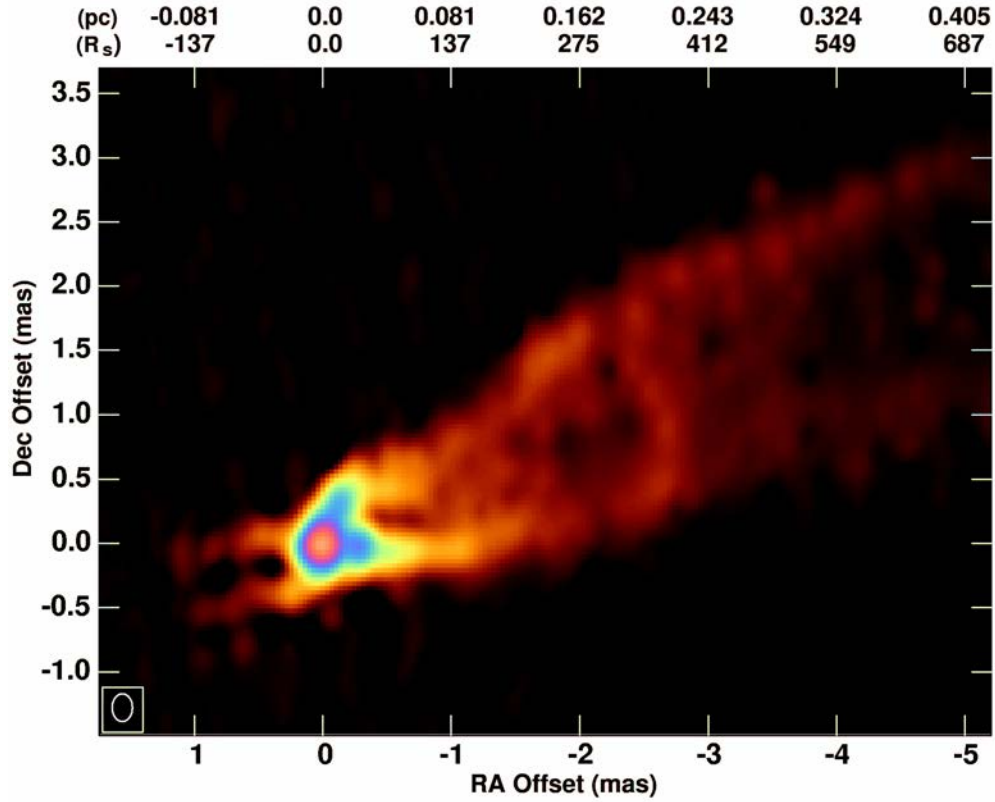


Figure 1.2: M87 VLA observation at 43GHz with $0.21\text{mas} \times 0.43\text{mas}$ beam. A prominent jet and a counterjet propagate away from the core. The extent of the image is $4.5\text{mas} \times 6\text{mas}$. Note that for M87, 1 mas of angular width corresponds to about 300 gravitational radii ($M = r_S/2$). Limb brightening is apparent. Courtesy of R. Craig Walker (NRAO).

1.2 Current Observations

Modern AGN jet astronomy and astrophysics are still saddled with open questions surrounding jet emission from bands throughout the electromagnetic spectrum in light of recent observations. Very long baseline interferometry (VLBI) involving radio telescopes such as the Atacama Large Millimeter/sub-millimeter Array (ALMA) and others separated by intercontinental distances promises to reveal microarcsecond angular resolution features of sub-mm (greater than 300GHz) emission of AGN [31]. In the remarkable M87 radio observation in Figure 1.2, there is enough spatial resolution to unambiguously see emission from both jet and counterjet. However, there is little consensus regarding even what region along the entire length of AGN jets is the emitted power most highly concentrated [10][36]. High resolution VLBI suggests that the central engine of M87 is found at radii $14r_S < r < 23r_S$ as M87 becomes optically thin for $\nu \geq 230\text{GHz}$ [25]. Radio sources have

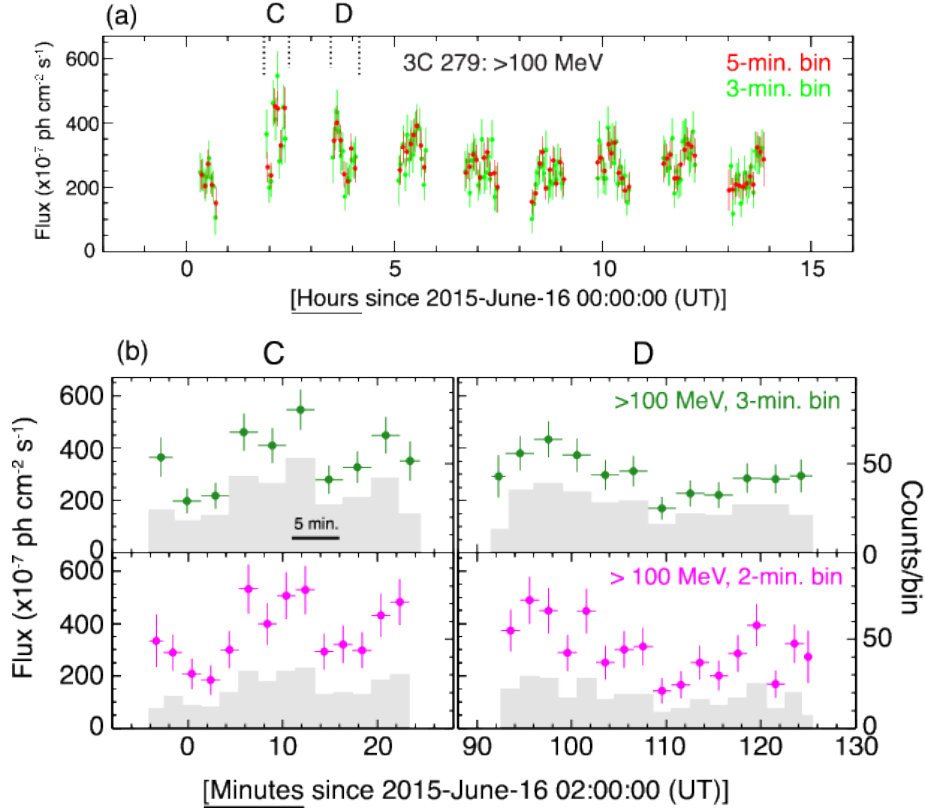


Figure 1.3: Intense 2015 >100 MeV flaring event of 3C 279 seen by *Fermi*-LAT (top panel). Orbits B-J are presented (orbital period 95.4min). In Orbits C and D (bottom panels), the flux is observed to vary by a factor of ~ 2 on 5-min timescales for data collected in 3-min and 2-min bins. The Event Horizon Telescope will likely see 3C 279— a 20 Jy radio source [58]. (Confer [55]).

compact cores that can be more and more closely resolved at higher frequencies.

For gamma ray sources, imaging is not a practical concern of observers. Gamma ray sources are detected either directly from their cosmic rays or from Cherenkov radiation emitted by cosmic rays temporarily exceeding the local speed of light. There are three major operational ground-based Cherenkov telescope arrays [28]: the High Energy Stereoscopic System (H.E.S.S.) sensitive to $30 \text{ GeV} < \nu < 100 \text{ TeV}$, the Major Atmospheric Gamma Ray Cherenkov (MAGIC) array sensitive to $\mathcal{O}(10 \text{ GeV}) < \nu < \mathcal{O}(10 \text{ TeV})$ and the Very Energetic Radio Imaging Telescope Array System (VERITAS) sensitive to $50 \text{ GeV} < \nu < 50 \text{ TeV}$. There are key questions surrounding gamma ray sources about other aspects than morphology. For example, the quasar 3C 279 in the constellation Virgo has exhibited significant variability on 5-*minute* timescales.

Also, the lag durations between peaks in radio emission following peaks in gamma emission have heretofore been difficult to ascertain due to poor sample statistics. For example, the *Fermi* Catalog

3FGL conclusively identifies at 15 GHz only 1563 AGN [3], which are compared at radio frequencies by the Owens Valley Radio Observatory (OVRO). Moreover, widely disparate hypotheses for jet plasma composition (e.g., leptonic [13] or hadronic [12]) may be in concordance with observed AGN spectra. Unlike absolute pair content, the electron-to-proton number ratio cannot be determined by the Comptonization of jet features on soft CMB photons or the amount of X-ray excess. As these energetic, variability and spectral considerations of AGN jets continue to be addressed by ever more advanced detectors with greater signal-to-noise, a parallel new front of state-of-the-art astrophysical simulations has rapidly emerged with the potential to answer these questions- and others that may in principle be inaccessible to observational astronomy as we see in the following.

Unlike observational astronomy, simulations of astrophysical systems are not diffraction limited, nor is their vantage point restricted by the position of the astrophysical object of interest relative to the Earth. The potentially greater spatial/angular resolution may resolve the question of what physical location dominates jet power emission. The duration for which radio peaks follow gamma ray peaks may be deduced from statistical analysis of simulated light curves. Whether astrophysical jets are primarily leptonic or hadronic may be resolved by comparisons between observations and simulations in which the primary source of gamma emission is modeled as inverse Compton scattering from jet electrons and positrons versus pion decay gamma rays from secondary products of jet hadron collisions. Furthermore, rotating the vantage point for viewing AGN jet simulations is an efficient way to generate a large sample of AGN with different viewing angles from the jet axis, facilitating obtaining significant estimates of observed properties of a population of AGN, e.g., azimuthally-averaged intensity.

1.3 Looking Forward

1.3.1 Cherenkov Array Telescope

The Cherenkov Array Telescope (CTA) will consist of over 100 telescopes distributed around the globe that together will achieve full sky coverage [2] and may be operational by 2020. Prime candidates for the location of CTA North and CTA South are the Canary Islands, Spain [17] and Chilean Andes [6], respectively. CTA's unprecedented image reconstruction capability is anticipated to reveal about 1,000 previously undetected gamma ray sources at energies between 100 GeV and 10 TeV. The CTA will see TeV emission from M87.

1.3.2 Event Horizon Telescope

The Event Horizon (EHT) is a collection of intercontinental baselines that will produce μ as angular resolution sub-mm radio very long baseline interferometer (VLBI) images. These baselines enable the EHT to measure closure phases and visibility amplitudes that can be Fourier transformed

to produce configuration space intensity maps. The EHT has measured closure phases of approximately 0° [4] for M87, with increasing precision expected in the near future. Current EHT baselines such as Arizona’s Heinrich Hertz Sub-Millimeter Telescope (SMT) and OVRO’s Combined Array for Research in Millimeter-wave Astronomy (CARMA) are already producing observational results. The size of the M87 emission regions of γ -flares (or enhancement) at above 100 GeV is constrained by causality consideration to be $r < 60\mathcal{D}$ light days $\sim 60r_S$ and by the SMT-CARMA resolution limit for its radio counterpart to be $r > 20r_S$ [4] (assuming the same particle population produced both components).

1.3.3 Observing Jet Simulations

The study of JAB systems has been transformed by MHD simulations. While semi-analytic models [15] [23] give highly stylized jets, simulations self-consistently capture detailed morphology of asymmetrical flows on scales spanning several decades. To match observations, the simulation flow variables must be converted to radiation, and there are two main approaches to accomplishing this. Particle-in-cell (PIC) codes are built with microphysical radiation processes in each cell [44], whereas a phenomenological approach such as that adopted here using a rather basic simulation infers the particle acceleration to add based on observations. In this work, I use general relativistic magnetohydrodynamic (GRMHD) simulations from [38] and [39] (hereafter MB09 and MTB12) with different emissivity prescriptions to carry out the process of “observing” simulations of jet/(accretion disk)/black hole (JAB) systems from ray tracing between image plane and source to convolving the resulting images with point spread functions. I will also illustrate the evolution of simulations of JAB systems’ dynamical and kinematic variables, e.g., magnetic field and bulk velocity, respectively, from various observer angles relative to the black hole spin axis. These quantities will be azimuthally-averaged and presented as a function of cylindrical radius from the jet axis. To answer the aforementioned open questions in radio astronomy, I will produce fixed observer time intensity maps (for observer time spans of thousands of gravitational-radius-light-crossing times $T_g = r_g/c = GM/c^3$) with various accretion flow/plasma-physics motivated prescriptions for the emissivity function of physical quantities (e.g., velocity shear) from the simulation output. “Observing” simulations also provide convenient means to examine potentially superluminal bulk flows and the polarization of jet segments. With the advantages of the absence of a diffraction limit, panoramic views of the same object and the ability to freely track features, this project promises to match the versatility of upcoming telescopes for AGN research such as the EHT and the CTA. Previous attempts at using GRMHD simulations to produce synthetic observation have typically differed by not focusing on the jets, e.g., Ricarte and Dexter’s work modeling EHT images of Sgr A* [48] or not using the constant observer time (finite light speed) effect [40]. Generally, simulations “observed” in extant works have yet to achieve the resolution of the fully general relativistic

MTB12 simulation used here. Movies of JAB simulations produced in this work will serve a captivating and engaging educational tools for furthering the community’s understanding of AGN jets (see <http://richardanantua.com/sample-page/jetaccretion-diskblack-hole-movies/>). Ultimately, I hope the methodology of mapping emissivity prescriptions to intensity and polarization maps in simulations will anticipate observations by future generation instruments and researchers.

1.3.4 This Thesis

The parts of this thesis following the above Introduction are organized as follows. Chapter 2 provides theoretical background on the important astrophysical processes expected to dominate emission from jets– synchrotron radiation and inverse Compton scattering– recasting them in a language germane to this work. Chapter 3 describes the general relativistic magnetohydrodynamic simulation used in this treatment of astrophysical plasmas as fluids, the flow state variables returned by the simulation and the mapping between simulation and physical units. In Chapter 4, a stationary, axisymmetric model based on the simulation is introduced to provide a more intuitive understanding. In Chapter 5, emission prescriptions– the most novel contribution of this work– are specified to reverse engineer observations. Chapter 6 develops the framework for polarized radiative transfer used for intensity and polarization map-making, including Mathematica tips. In Chapters 7 and 8, the methods developed in this work are applied to produce intensity maps of the unbeamed BL-Lac M87 and the high-power quasar 3C 279. Chapter 9 provides a basic statistical analysis of the “observing” jet simulation framework applied to individual sources and surveys. Future directions are proposed in Chapter 10.

Conceptually, it is useful to organize this work according to the flow chart shown in Figure 1.4.

Analysis Pipeline for Observing Jet Simulations

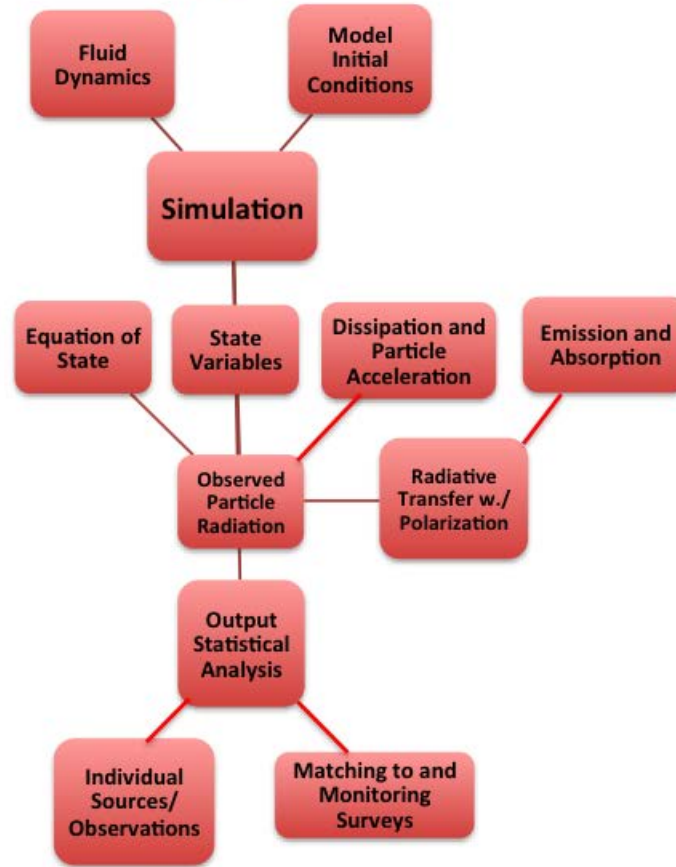


Figure 1.4: Logical flowchart for “Observing Jet Simulations.” Starting from the top down, we have fluid dynamics of plasma accreting onto a supermassive black hole and jet/disk/black hole model initial conditions. These are inputs to our simulation, which outputs state variables fluid rest mass density, gas energy density, 4-velocity and 4-magnetic field. In order to produce image maps, we must add an equation of state, dissipation and particle acceleration, and emission and absorption, and then perform radiative transfer. From the “observed” particle radiation, we will perform output statistical analysis. The output statistical analysis will be compared to individual sources and surveys. This flowchart is a basic outline that may omit model-specific inputs such as soft photon field for inverse Compton models.

Chapter 2

Radiative Processes

There are four fundamental radiative processes in astrophysics: blackbody, bremsstrahlung, Compton and synchrotron. Blackbody radiation is a thermal process, whereas the others need not be. Bremsstrahlung predominates in regions of sufficiently high target gas density, such as the intracluster medium seen in X-rays or H II regions at radio wavelengths. The processes that are responsible for the tremendous power output of relativistic jets and their surrounding magnetized accretion flows are inverse Compton radiation and synchrotron radiation. The following preliminary treatment of the theory of these two processes will provide necessary background to motivate emission prescriptions used in this work. One would be remiss not to mention atomic transition processes that result in absorption or emission line features. Molecular lines enable astronomers to detect molecular clouds comprised of H₂, CO or CS, and the 21 cm hydrogen line is used to detect diffuse clouds, HI clouds and intercloud medium [33]. Thermal and kinetic line broadening give information about the motion and temperature of astrophysical sources.

2.1 Synchrotron Radiation and Gas Dynamics

Galaxies are surrounded by a network of tangled magnetic fields that store energy tapped into by particles that gyrate about them, radiating synchrotron radiation as the particles accelerate. The Larmor frequency ν_e for an electron gyrating in a helical path of pitch angle α and circumference $2\pi R = v_{\perp} t = v_{\perp} / \nu_e = v \sin \alpha / \nu_e$ around a magnetic field line under centripetal force $\gamma m_e v_{\perp}^2 / R = \frac{e}{c} v_{\perp} B$ is $\nu_e = eB / 2\pi \gamma m_e c$ transforms as $\nu_{\text{Obs}} \sim \gamma^3 \nu_e$ in the lab frame. This statement can be derived using the following arguments: The synchrotron particle, accelerating normal to its velocity, emits radiation into a cone of opening angle $2/\gamma$ (see Figure 2.1) observed only when the line of sight lies within this cone, i.e., for $\Delta t = \frac{s}{v} = \frac{(R/\sin \alpha)(2/\gamma)}{2\pi \nu_e R/\sin \alpha} = \frac{2}{\gamma \omega_e}$, where we have used the formula for the arc length along a helix $s = ((\frac{dx}{d\theta})^2 + (\frac{dy}{d\theta})^2)^{1/2} \theta = R\sqrt{1 + \cot^2 \alpha} = R/\sin \alpha$. To find the observed frequency, note that to reach an observer distance D from the initial and final parts of the

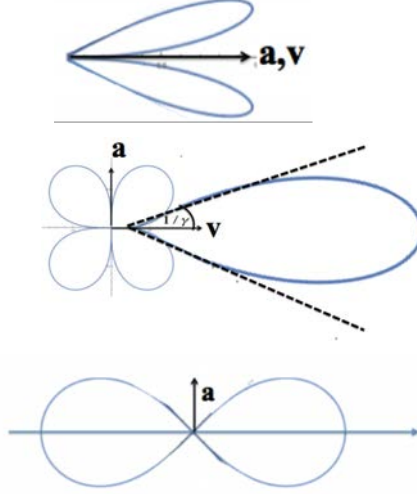


Figure 2.1: Profile of synchrotron emission from a single electron moving in the direction of acceleration (top), perpendicular to acceleration (middle) and instantaneously at rest (bottom). (Adapted from [50]).

pulse takes $t_{1,\text{Obs}} = \frac{D}{c} + t_{1,\text{emit}}$ and $t_{2,\text{Obs}} = \frac{D-\Delta s}{c} + t_{2,\text{emit}}$, respectively, so $\Delta t_{\text{Obs}} = \Delta t - \frac{\Delta s}{c} = \frac{2}{\gamma\omega_e} - \frac{2R}{\gamma c \sin \alpha} = \frac{2}{\gamma\omega_e} - \frac{2v \sin \alpha}{\gamma c \omega_e \sin \alpha} = \frac{2}{\gamma\omega_e} \left(1 - \frac{v}{c}\right) \approx \frac{2}{\gamma\omega_e} \left(\frac{1}{2\gamma^2}\right) = \frac{m_e c}{\gamma^2 e B}$ and $\nu_{\text{Obs}} \approx \frac{\gamma^2 e B}{m_e c} \sim \gamma^3 \nu_e$. Thus, the Doppler beaming that narrows observed pulse duration by a factor of γ and the light from more distant early portions of the trajectory of the approaching source catching up with emission from later and closer portions that shortens the observed beam by a factor γ^2 result in an observed synchrotron frequency quadratic in γ and a factor of γ^3 greater than the Larmor frequency.

The Larmor formula for synchrotron radiation power from a single electron is

$$p_e = 2\gamma^2 \sigma_T c \frac{B_{\perp}^2}{8\pi} \quad (2.1)$$

[50]. We have for a power law population of electrons

$$N_{\gamma} \sim K\gamma^{-p} \sim K\gamma^{-(2\alpha+1)} \quad (2.2)$$

and for pressure

$$P \sim \int \gamma d\gamma N_{\gamma}. \quad (2.3)$$

To find the pressure dependence of K , we must specify the particle distribution. For our AGN

application, we take $\alpha = (p - 1)/2 \sim 0.5$, (power law index $p = 2$), which gives

$$P_e \sim \int_{\gamma_{\min}}^{\gamma_{\max}} d\gamma K \gamma^{-1} \sim K \ln(\gamma_{\max}/\gamma_{\min}) \quad (2.4)$$

Otherwise, one finds

$$P_e \sim \frac{K}{2-p} \left(\gamma_{\max}^{2-p} - \gamma_{\min}^{2-p} \right). \quad (2.5)$$

2.1.1 Synchrotron Self-Absorption

For a thermal population of source particles, Kirchhoff's law gives $j_\nu = \chi_\nu B_\nu(T)$, where χ_ν is the absorption coefficient. In the Rayleigh Jeans (low frequency) limit,

$$(S_\nu)_{\text{thermal}} = B_\nu(T) = \frac{2h\nu^3/c^2}{e^{\frac{h\nu}{k_B T}} - 1} \approx \frac{2k_B T \nu^2}{c^2}, \quad (\chi_\nu)_{\text{thermal}} \approx \frac{c^2}{2k_B T \nu^2} j_\nu \quad (2.6)$$

For the non-thermal case of synchrotron radiation, to express the solution I_ν of the radiative transfer equation with emission and absorption in terms of simulation input variables t_{Obs} and ν_{Obs} and simulation output variables b^μ and ρ , assume that the frequency dependence of I_ν is given by a blackbody spectrum at the brightness temperature

$$I_\nu = B_\nu(T_b) \approx \frac{2k_B T_b \nu^2}{c^2} \quad (2.7)$$

in the Rayleigh-Jeans limit. We can eliminate T_b in favor of $\nu_{\text{Obs}} = \mathcal{D}\nu$ and B by noting that the brightness temperature in a relativistic plasma ($c_p/c_V = 4/3$) is related to the mean energy per particle via $\gamma m_e c^2 = \frac{1}{\frac{4}{3}-1} k_B T_e = 3k_B T_e = 3k_B T$, where we consider radio frequencies low enough so that the synchrotron electron temperature T_e equals the brightness temperature T_b , i.e., $T_e = T_b \equiv T$. Also note that the particle Lorentz factor is related to the observed frequency of synchrotron as $\gamma \sim (\frac{\nu_{\text{Obs}}}{eB/m_e c})^{1/2}$. Thus,

$$T \approx \frac{m_e^{3/2} c^{5/2}}{3k_B e^{1/2}} B^{-1/2} \nu_{\text{Obs}}^{1/2} \quad (2.8)$$

and

$$I_\nu \approx \frac{2m_e^{3/2} c^{1/2}}{3e^{1/2}} \mathcal{D}^2 B^{-1/2} \nu_{\text{Obs}}^{5/2}. \quad (2.9)$$

The expression for the synchrotron-self-absorbed source function in the case of a power law electron spectral distribution $N_e \sim \gamma^{-p}$ is given in Chapter 6 of Rybicki and Lightman as

$$(S_\nu)_{\text{power law}} = \frac{1}{\chi_\nu} \frac{P_\nu}{4\pi}, \quad (2.10)$$

where

$$(P_\nu)_{\text{power law}} = \frac{\sqrt{3}q^3 C B \sin \alpha}{2\pi m c^2 (p+1)} \Gamma\left(\frac{p}{4} + \frac{19}{12}\right) \Gamma\left(\frac{p}{4} - \frac{1}{12}\right) \left(\frac{mc2\pi\nu}{3qB \sin \alpha}\right)^{-\frac{p-1}{2}}, \quad (2.11)$$

$$(\chi_\nu)_{\text{power law}} = \frac{\sqrt{3}q^2}{8\pi m} \left(\frac{3q}{2\pi m^3 c^5}\right)^{\frac{p}{2}} C(B \sin \alpha)^{\frac{p+2}{2}} \Gamma\left(\frac{3p+2}{12}\right) \Gamma\left(\frac{3p+22}{12}\right) \nu^{-\frac{p}{2}-2} \quad (2.12)$$

so

$$(S_\nu)_{\text{power law}} = \sqrt{\frac{2qm}{3\pi c^3}} (mc^2)^p \sin^{\frac{1}{2}} \alpha \frac{\Gamma\left(\frac{p}{4} + \frac{19}{12}\right) \Gamma\left(\frac{p}{4} - \frac{1}{12}\right)}{\Gamma\left(\frac{3p+2}{12}\right) \Gamma\left(\frac{3p+22}{12}\right)} B^{-\frac{1}{2}} \nu^{\frac{5}{2}}, \quad (2.13)$$

and the source function is proportional to the intensity function, as expected.

2.1.2 Polarization of Synchrotron Radiation

Polarization, which depends on the orientation of magnetic fields in astrophysical plasma, gives us a window into the detailed structure of these fields. In this work, we focus on linear polarization due to the difficulty of observing circular polarization. For instance, for synchrotron radiation in a uniform medium, the degree of circular polarization is $\sim 3/\gamma$, which works out to 1% for typical compact radio sources [33].

We are interested in the transport of polarized synchrotron radiation in the simulation (unprimed) frame in which the electromagnetic and flow variables are most naturally expressed. However, the emission and absorption are most easily calculated in a (primed) fluid rest frame defined by the MHD solution moving with velocity \vec{v} and in which $\vec{E}' = \vec{0}$. To facilitate these transformations, we first express the comoving ray direction \hat{n}' and magnetic field \vec{B}' in terms of simulation frame variables as follows. From Jackson's Electrodynamics [29],

$$\vec{B}' = \gamma(\vec{B} - \vec{\beta} \times \vec{E}) - \frac{\gamma^2}{\gamma+1} \vec{\beta}(\vec{\beta} \cdot \vec{B}) \quad (2.14)$$

In the Galaxy Frame, $\vec{E} = -\vec{\beta} \times \vec{B}$, so

$$\begin{aligned} \vec{B}' &= \gamma(\vec{B} + \vec{\beta} \times (\vec{\beta} \times \vec{B})) - \frac{\gamma^2}{\gamma+1} \vec{\beta}(\vec{\beta} \cdot \vec{B}) = \gamma(\vec{B} + \vec{\beta}(\vec{\beta} \cdot \vec{B}) - \vec{B}(\vec{\beta} \cdot \vec{\beta})) - \frac{\gamma^2}{\gamma+1} \vec{\beta}(\vec{\beta} \cdot \vec{B}) \\ &= \gamma(1 - \beta^2)\vec{B} + \gamma\vec{\beta}(\vec{\beta} \cdot \vec{B}) - \frac{\gamma^2}{\gamma+1} \vec{\beta}(\vec{\beta} \cdot \vec{B}) \\ &= \frac{1}{\gamma}\vec{B} + \left[\gamma - \frac{\gamma^2}{\gamma+1}\right] \vec{\beta}(\vec{\beta} \cdot \vec{B}) = \frac{\vec{B}}{\gamma} + \frac{\gamma(\vec{B} \cdot \vec{v})\vec{v}}{\gamma+1} \end{aligned}$$

The aberration of the angle between an emitted light ray and the direction of relative motion between

the emitter and galaxy frame¹ is given by

$$\begin{aligned}\sin\theta' &= \frac{\sin\theta}{\gamma(1-\beta\cos\theta)} = \mathcal{D}\sin\theta \\ \cos\theta' &= \frac{\cos\theta-\beta}{\gamma(1-\beta\cos\theta)} = \gamma\mathcal{D}(\cos\theta - \beta)\end{aligned}\quad (2.15)$$

where primes apply to the frame of the moving emitter. Since special relativity only alters lengths along the direction of relative motion, the transformed observer direction \hat{n}' must be coplanar with \hat{n} and \vec{v} , i.e., $\hat{n}' = a\hat{n} + b\vec{v}$. Then $|\hat{n}' \times \vec{v}| = v\sin\theta' = \mathcal{D}v\sin\theta = \mathcal{D}|\hat{n} \times \vec{v}|$ and so $\hat{n}' \times \vec{v} = \mathcal{D}\hat{n} \times \vec{v} \implies a = \mathcal{D}$. Likewise, dotting \vec{v} into \hat{n}' from the right and using the cosine identity, we get $\hat{n}' \cdot \vec{v} = \gamma\mathcal{D}(\hat{n} \cdot \vec{v} - v^2) = \mathcal{D}\hat{n} \cdot \vec{v} + bv^2$, we get

$$\begin{aligned}-v^2b &= \mathcal{D}\hat{n} \cdot \vec{v} - \gamma\mathcal{D}(\hat{n} \cdot \vec{v} - v^2) = \mathcal{D} - \frac{1}{\gamma} - \gamma\mathcal{D}\left(1 - \frac{1}{\gamma\mathcal{D}} - v^2\right) = \mathcal{D} - \frac{1}{\gamma} - \frac{\mathcal{D}}{\gamma} + 1 \\ \implies b &= -\frac{\gamma^2(\mathcal{D} - \frac{1}{\gamma} - \frac{\mathcal{D}}{\gamma} + 1)}{\gamma^2 - 1} = -\frac{(\mathcal{D}+1)\gamma}{1+\gamma}\end{aligned}\quad (2.16)$$

where we have used $\hat{n} \cdot \vec{v} = 1 - \frac{1}{\gamma\mathcal{D}}$, $v^2 = (\gamma^2 - 1)/\gamma^2$. These following identities are worth repeating, as they will be useful in formulating synchrotron radiation prescriptions

$$\begin{aligned}\vec{B}' &= \frac{\vec{B}}{\gamma} + \frac{\gamma(\vec{B} \cdot \vec{v})\vec{v}}{\gamma + 1} \\ \hat{n}' &= \mathcal{D}\hat{n} - \frac{\gamma\mathcal{D} + 1}{\gamma + 1}\vec{v},\end{aligned}\quad (2.17)$$

where $\mathcal{D} = \nu/\nu' = [\gamma(1 - \hat{n} \cdot \vec{v})]^{-1}$ is the Doppler factor.

The polarized synchrotron emissivity depends upon the component of the magnetic field resolved perpendicular to \hat{n}' in the comoving frame, $B'_\perp \equiv |\vec{B}' - (\vec{B}' \cdot \hat{n}')\hat{n}'|$. It is convenient to express this in terms of the effective field B_e evaluated in terms of simulation frame variables by

$$B_e = \mathcal{D}^{-1}B'_\perp = [B_\perp^2 + E_\perp^2 - 2\vec{E}_\perp \times \vec{B}_\perp]^{1/2},$$

where $\vec{B}_\perp, \vec{E}_\perp$ are resolved perpendicular to \hat{n} . Note that eB_e/m_e is the magnitude of the perpendicular acceleration experienced by an ultrarelativistic electron moving towards the observer. It is also helpful to note that $B'_\parallel \equiv \vec{B}' \cdot \hat{n}' = \mathcal{D}B_\parallel/\gamma - \vec{B} \cdot \vec{v}$, where $B_\parallel \equiv \vec{B} \cdot \hat{n}$.

In the theory of optically thick, polarized radiative transfer, a useful comoving quantity from which comoving emission and absorption functions are generated is the power per unit frequency from each polarization

$$p'_{\nu',1,2}(x) = \frac{\sqrt{3}\mu_0 e^3 c B'_\perp}{4\pi m_e} \left[\frac{x}{2} \left(\pm K_{2/3}(x) + \int_x^\infty K_{5/3}(x') dx' \right) \right], \quad \text{where } x = \frac{\nu'}{\nu'_c} \quad (2.18)$$

¹The galaxy frame will sometimes be denoted "Gal" frame for brevity.

K_q is a modified Bessel function of imaginary argument and 1 and 2 refer to two independent polarization directions. Then the comoving emissivity components for a power law electron² distribution are

$$\begin{aligned} j'_{\nu'\Omega',1,2} &= K'_{\Omega'} \left(\frac{\nu'_c}{\gamma'^2} \right)^{\frac{p-1}{2}} \int_0^\infty dx 2x^{\frac{p-3}{2}} p'_{\nu',1,2}(x) \\ &= \frac{\mu_0 e^3 c B'_\perp K'_\Omega}{8\sqrt{3}\pi m_e} \left(\frac{3eB'_\perp}{2\pi\nu' m_e} \right)^{\frac{p-1}{2}} \frac{\Gamma(\frac{3p-1}{12})\Gamma(\frac{3p+7}{12})}{p+1} \left\{ \frac{3p+5}{2}, 1 \right\} \\ &= \frac{1}{4\sqrt{3}} \tilde{P}_e \left(\frac{r_e \nu'}{c} \right) \left(\frac{3eB'_\perp}{2\pi\nu' m_e} \right)^{\frac{3}{2}} \frac{\Gamma(\frac{3p-1}{12})\Gamma(\frac{3p+7}{12})}{p+1} \left\{ \frac{3p+5}{2}, 1 \right\}, \end{aligned} \quad (2.19)$$

where the last step introduces the (proper) partial pressure due to leptons contributing to emission in the band $[\nu, 2\nu]$

$$\tilde{P}_e = \frac{4\pi}{3} K'_{\Omega'} m_e c^2 \gamma'^{2-p} = \frac{4\pi}{3} K'_{\Omega'} m_e c^2 \left(\frac{3eB'_\perp}{2\pi\nu' m_e} \right)^{\frac{p-2}{2}} \quad (2.20)$$

Since this quantity is defined in the galaxy frame, there is no reason to use primed notation. As for the absorption coefficient in the power law case,

$$\begin{aligned} \chi'_{\nu',1,2} &= -\frac{1}{m_e \nu'^2} \int d\gamma' \gamma'^2 \frac{d}{d\gamma'} \left(\frac{N'_{\gamma',\Omega'}}{\gamma'^2} \right) p'_{\nu',1,2}(\gamma') \\ &= \frac{\sqrt{3}(p+2)\mu_0 e^3 c B'_\perp K'_\Omega}{16\pi m_e^2 \nu'^2} \left(\frac{3eB'_\perp}{4\pi\nu' m_e} \right)^{\frac{p}{2}} \left(\pm K_{2/3}(x) + \int_x^\infty dx' K_{5/3}(x') \right) \\ &= \frac{\mu_0 e^3 c B'_\perp K'_\Omega}{8\pi \sqrt{3} m_e^2 \nu'^2} \left(\frac{3eB'_\perp}{2\pi\nu' m_e} \right)^{p/2} \Gamma\left(\frac{3p+2}{12}\right) \Gamma\left(\frac{3p+10}{12}\right) \left\{ \frac{3p+8}{2}, 1 \right\} \\ &= \frac{1}{4\sqrt{3}} \left(\frac{\tilde{P}_e}{m_3 \nu'^2} \right) \left(\frac{r_e \nu'}{c} \right) \left(\frac{3eB'_\perp}{2\pi\nu' m_e} \right)^2 \Gamma\left(\frac{3p+2}{12}\right) \Gamma\left(\frac{3p+10}{12}\right) \left\{ \frac{3p+8}{2}, 1 \right\} \end{aligned} \quad (2.21)$$

Now, to transform to the galaxy frame, recall the Lorentz invariance of j/ν^2 and $\chi\nu$ gives

$$\begin{aligned} j_{\nu\Omega,1,2}(\nu, \hat{n}, \vec{B}) &= \mathcal{D}^2 \frac{1}{4\sqrt{3}} \tilde{P}_e \left(\frac{r_e \nu}{c} \right) \left(\frac{3eB'_\perp}{2\pi\nu' m_e} \right)^{\frac{3}{2}} \frac{\Gamma(\frac{3p-1}{12})\Gamma(\frac{3p+7}{12})}{p+1} \left\{ \frac{3p+5}{2}, 1 \right\} \\ \chi_{\nu,1,2}(\nu, \hat{n}, \vec{B}) &= \mathcal{D}^{-1} \frac{1}{4\sqrt{3}} \left(\frac{\tilde{P}_e}{m_3 \nu'^2} \right) \left(\frac{r_e \nu}{c} \right) \left(\frac{3eB'_\perp}{2\pi\nu' m_e} \right)^2 \Gamma\left(\frac{3p+2}{12}\right) \Gamma\left(\frac{3p+10}{12}\right) \left\{ \frac{3p+8}{2}, 1 \right\} \end{aligned} \quad (2.22)$$

Noting

$$\begin{aligned} B'_\perp &= |\vec{B}' \times \hat{n}'| = [(\vec{B}' \times \hat{n}') \cdot (\vec{B}' \times \hat{n}')]^{1/2} = \mathcal{D}[\{\vec{B} \times (\hat{n} - \vec{v})\}^2 - \{(\vec{B} \times \hat{n}) \cdot \vec{v}\}^2]^{1/2} \\ &= \mathcal{D}|\vec{B} \times \hat{n} - \vec{E}_\perp| = \mathcal{D}[B_\perp^2 + E_\perp^2 - 2N_{||}]^{1/2} = \mathcal{D}B_e \end{aligned} \quad (2.23)$$

and $\nu = \mathcal{D}\nu'$, we have the simulation frame quantities

$$\begin{aligned} j_{\nu\Omega,1,2}(\nu, \hat{n}, \vec{B}) &= \mathcal{D}^4 \tilde{P}_e \frac{r_e \nu}{4\sqrt{3}c} \left(\frac{3eB_e}{2\pi\nu m_e} \right)^{\frac{3}{2}} \frac{\Gamma(\frac{3p-1}{12})\Gamma(\frac{3p+7}{12})}{p+1} \left\{ \frac{3p+5}{2}, 1 \right\} \\ \chi_{\nu,1,2}(\nu, \hat{n}, \vec{B}) &= \mathcal{D}^4 \tilde{P}_e \frac{r_e}{4\nu\sqrt{3}c} \left(\frac{3eB_e}{2\pi\nu m_e} \right)^2 \Gamma\left(\frac{3p+2}{12}\right) \Gamma\left(\frac{3p+10}{12}\right) \left\{ \frac{3p+8}{2}, 1 \right\} \end{aligned} \quad (2.24)$$

It is instructive to extract the p dependence from $j_{\nu\Omega,1,2}$ and $\chi_{\nu\Omega,1,2}$ as in the plots of Figure 2.2. It will also be useful to form the sum and difference of the Galaxy Frame emissivity components and

²In this section, electrons and positrons can be used interchangeably.

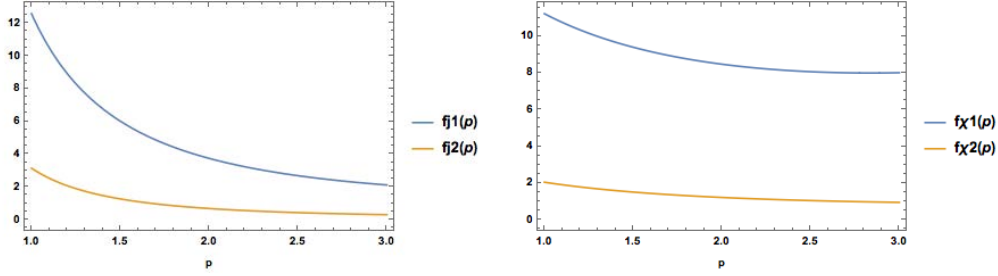


Figure 2.2: Dependence of (left) synchrotron emission function and (right) absorption function with lepton power law p .

average and half difference of the Galaxy Frame absorption function components

$$\begin{aligned}
 j_{\nu\Omega} &\equiv j_{\nu\Omega,1} + j_{\nu\Omega,2} = \mathcal{D}^4 \tilde{P}_e \frac{\sqrt{3}r_e\nu}{2c} \left(\frac{3eB_e}{2\pi\nu m_e} \right)^{\frac{3}{2}} \frac{\Gamma(\frac{3p-1}{12})\Gamma(\frac{3p+19}{12})}{p+1} \\
 \chi_{\nu} &\equiv \frac{\chi_{\nu 1} + \chi_{\nu 2}}{2} = \mathcal{D}^4 \tilde{P}_e \frac{\sqrt{3}r_e}{4m_e\nu c} \left(\frac{3eB_e}{2\pi\nu m_e} \right)^2 \Gamma\left(\frac{3p+2}{12}\right) \Gamma\left(\frac{3p+22}{12}\right) \\
 j_{\nu\Omega,1} - j_{\nu\Omega,2} &= \frac{3(p+1)}{3p+7} j_{\nu\Omega} \\
 \frac{\chi_1 - \chi_2}{2} &= \frac{3(p+2)}{3p+10} \chi
 \end{aligned} \tag{2.25}$$

where we have used $\Gamma(\frac{3p+19}{12})/\Gamma(\frac{3p+7}{12}) = \frac{3p+7}{12}$ and $\Gamma(\frac{3p+22}{12})/\Gamma(\frac{3p+10}{12}) = \frac{3p+10}{12}$.

Stokes parameters (I, Q, U, V) in the case of zero circular polarization ($V = 0$) obey the system of polarization transfer equations

$$\frac{d}{ds} \begin{pmatrix} I \\ Q \\ U \end{pmatrix} = - \begin{pmatrix} \chi_I & \chi_Q & \chi_U \\ \chi_Q & \chi_I & 0 \\ \chi_U & 0 & \chi_I \end{pmatrix} \begin{pmatrix} I \\ Q \\ U \end{pmatrix} + \begin{pmatrix} j_1 + j_2 \\ (j_1 - j_2) \cos 2\psi \\ (j_1 - j_2) \sin 2\psi \end{pmatrix}. \tag{2.26}$$

where

$$\begin{aligned}
 \alpha_I &= \frac{\chi_1 + \chi_2}{2} \\
 \alpha_Q &= \frac{(\chi_1 + \chi_2) \cos 2\psi}{2} \\
 \alpha_U &= \frac{(\chi_1 + \chi_2) \sin 2\psi}{2}
 \end{aligned} \tag{2.27}$$

and $\psi = \tan^{-1}(BX^2 + BY^2 + EX^2 + EY^2 - 2(EX \cdot BY - EY \cdot BX))$ (see Figure 2.3 for definition of observer coordinates X and Y). Integrating from observer to source in the case of constant ψ , we set the boundary conditions of this inhomogeneous system of coupled differential equations to be $I(0) = Q(0) = U(0) = 0$ in Mathematica to get

$$\begin{aligned}
I(s) &= \frac{\chi_1 j_2 + \chi_2 j_1 - \chi_2 j_1 e^{-\chi_1 s} - \chi_1 j_2 e^{-\chi_2 s}}{\chi_1 \chi_2} \\
Q(s) &= \frac{(j_2 \chi_1 (1 - e^{-\chi_2 s}) + j_1 \chi_2 (e^{-\chi_1 s} - 1)) \cos 2\psi}{\chi_1 \chi_2} \\
U(s) &= \frac{(j_2 \chi_1 (1 - e^{-\chi_2 s}) + j_1 \chi_2 (e^{-\chi_1 s} - 1)) \sin 2\psi}{\chi_1 \chi_2}
\end{aligned} \tag{2.28}$$

The first of these solutions in (2.28) reduces to the formal solution of the radiative transfer equation in Chapter 4 when $\chi_1 = \chi_2 \equiv \chi$ and $2j_1 = 2j_2 \equiv j$. The time-dependent calculation requires more care, but will be approximately solved by the method of quadrature (integration) in Chapter 6 the important cases of optically thin, polarized emission ($\chi_I = \chi_Q = \chi_U = 0$) and optically thick, unpolarized intensity ($Q = U = 0$).

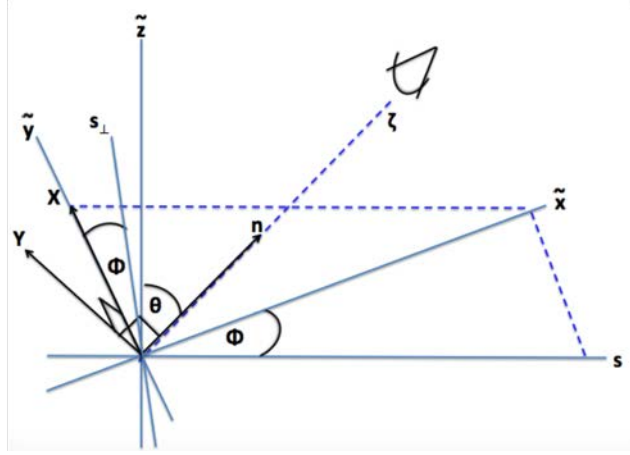


Figure 2.3: Polarization axes X and Y on the sky superposed onto simulation Cartesian coordinates $\{\tilde{x}, \tilde{y}, \tilde{z}\}$ and simulation cylindrical polar coordinates $\{s, \phi, \tilde{z}\}$. The displacement from the observer plane is parameterized by ζ and the inclination angle is θ .

In order to treat the time-dependent case where an analytic solution is intractable, it is convenient to define a new coordinate system. The following relations relate the convenient coordinate system in Figure 2.3 to Obs and Gal frame coordinates:

$$z_0 = \frac{\text{diam}}{2} - \zeta \tag{2.29}$$

$$\begin{pmatrix} x_{\text{Gal}} \\ y_{\text{Gal}} \\ z_{\text{Gal}} \end{pmatrix} = \begin{pmatrix} s \\ s_{\perp} \\ \tilde{z} \end{pmatrix} = \begin{pmatrix} \frac{\tilde{x}}{\cos \phi} \\ \frac{\tilde{y}}{\cos \phi} \\ \tilde{z} \end{pmatrix} \tag{2.30}$$

$$t_{\text{Obs}} = t_{\text{Gal}} - \frac{\zeta}{c} = t_{\text{Gal}} - \frac{|\vec{r}_{||}|}{c} \tag{2.31}$$

where $\vec{r}_{||} = \vec{r} \cdot \hat{n}$ is the component of the displacement vector parallel to the observer direction. We

also have

$$\hat{X} = \text{Rot}_{\hat{z}}(\phi)\hat{s}_{\perp} = \text{Rot}_{\hat{z}}(\phi)\hat{y}_{\text{Gal}} = \hat{y} = -\sin\phi\hat{x}_{\text{Gal}} + \cos\phi\hat{y}_{\text{Gal}} \quad (2.32)$$

where

$$\text{Rot}_{\hat{z}}(\phi) = \begin{pmatrix} \cos\phi & -\sin\phi & 0 \\ \sin\phi & \cos\phi & 0 \\ 0 & 0 & 1 \end{pmatrix} \quad (2.33)$$

and

$$\begin{aligned} \hat{Y} = \hat{n} \times \hat{X} &= \sin\theta \sin^2\phi \hat{z}_{\text{Gal}} - \cos\theta \sin\phi \hat{y}_{\text{Gal}} + \sin\theta \cos^2\phi \hat{z}_{\text{Gal}} - \cos\theta \cos\phi \hat{x}_{\text{Gal}} \\ &= -\cos\theta \cos\phi \hat{x}_{\text{Gal}} - \cos\theta \sin\phi \hat{y}_{\text{Gal}} + \sin\theta \hat{z}_{\text{Gal}} \end{aligned} \quad (2.34)$$

where one can check by applying

$$\text{Rot}_{\hat{z}}(\phi)\text{Rot}_{\hat{y}}\left(\theta - \frac{\pi}{2}\right) = \begin{pmatrix} \cos\phi & -\sin\phi & 0 \\ \sin\phi & \cos\phi & 0 \\ 0 & 0 & 1 \end{pmatrix} \begin{pmatrix} \sin\theta & 0 & -\cos\theta \\ 0 & 1 & 0 \\ \cos\theta & 0 & \sin\theta \end{pmatrix} \quad (2.35)$$

on \hat{z}_{Gal} . Using this formalism, one can express

$$\begin{aligned} BX &= \sin\phi_{\text{Obs}}B_x + \cos\phi_{\text{Obs}}B_y, \quad BY = -\cos\theta_{\text{Obs}}\cos\phi_{\text{Obs}}B_x - \cos\theta_{\text{Obs}}\sin\phi_{\text{Obs}}B_y + \sin\theta_{\text{Obs}}B_z \\ EX &= \frac{\sin\phi_{\text{Obs}}E_x + \cos\phi_{\text{Obs}}E_y}{c}, \quad EY = \frac{-\cos\theta_{\text{Obs}}\cos\phi_{\text{Obs}}E_x - \cos\theta_{\text{Obs}}\sin\phi_{\text{Obs}}E_y + \sin\theta_{\text{Obs}}E_z}{c} \end{aligned} \quad (2.36)$$

so the effective magnetic field is

$$B_e = \sqrt{(BX + EY)^2 + (BY - EX)^2} \quad (2.38)$$

2.1.3 Polarized Radiative Transfer Equations with Opacity

The general case of polarized radiative transfer with opacity is a coupled inhomogeneous system of differential equations 2.26. The solution in this case cannot be obtained by the method of quadrature.

2.2 Equipartition of Energy

The equipartition magnetic field strength B can be obtained by minimizing the total energy with respect to B . Following [24], we write the RHS of

$$U_{\text{Tot}} = U_e + U_p + U_B \quad (2.39)$$

in terms of B . The simplest is the magnetic energy in volume V

$$U_B = \frac{B^2}{8\pi} fV \quad (2.40)$$

where f is the filling fraction. Note

$$\frac{dE}{dt} = -\frac{2e^4}{3m_e^4 c^7} (B \sin \theta)^2 E^2 \quad (2.41)$$

Writing $U_p = (1 + K)U_e$, we must now write the electron energy in volume V in terms of B . We do this via the magnetic-field-dependent $L_{\text{Syn}} = V \int_{E_1}^{E_2} \left(-\frac{dE}{dt}\right) N(E) dE$ noting the peak synchrotron frequency is related to electron energy by $\nu_C = \frac{3e}{4\pi m_e^3 c^5} (B \sin \theta) \gamma E_e^2$:

$$\frac{U_e}{L_{\text{Syn}}} = \frac{V \int_{E_1}^{E_2} (N_0 E^{-p}) E dE}{N_0 V \frac{2e^4}{3m_e^4 c^7} (B \sin \theta)^2 \int_{E_1}^{E_2} E^{-p+2} dE} = \frac{-p+3}{-p+2} \frac{(c_1 B \sin \theta)^{1/2}}{c_2 (B \sin \theta)^2} \frac{\nu_2^{-\frac{p+2}{2}} - \nu_1^{-\frac{p+2}{2}}}{\nu_2^{-\frac{p+3}{2}} - \nu_1^{-\frac{p+3}{2}}} \quad (2.42)$$

where $c_1 \equiv \frac{3e}{4\pi m_e^3 c^5}$ and $c_2 \equiv \frac{2e^4}{3m_e^4 c^7}$. Then

$$u_{\text{Tot}} = (1 + K)c_3 L_{\text{Syn}} B^{-3/2} + \frac{fV}{8\pi} B^2 \quad (2.43)$$

where $c_3 = \frac{-p+3}{-p+2} \frac{c_1^{1/2}}{c_2} \frac{\nu_2^{-\frac{p+2}{2}} - \nu_1^{-\frac{p+2}{2}}}{\nu_2^{-\frac{p+3}{2}} - \nu_1^{-\frac{p+3}{2}}}$. The condition for minimizing the sum of energy from relativistic particles (electrons and protons) and magnetic energy

$$\frac{d(U_e + U_{pr} + U_B)}{dB} = 0 \quad (2.44)$$

yields $B_{\text{min}} = (6\pi(1 + K)c_3 \frac{L_{\text{Syn}}}{fV})^{2/7}$, and

$$\frac{U_e(B_{\text{min}})}{U_B(B_{\text{min}})} = \frac{4}{3(1 + K)} \quad (2.45)$$

Then at equipartition of electron particle and magnetic energy, $U_e \sim U_B$. Note that using this as a prescription to infer observed radiation requires modeling of several quantities, such as the cutoff values of the magnetic field, and the fraction of energy in protons. The formalism employing partial

pressures circumvents these difficulties.

2.3 Inverse Compton Radiation

The inverse Compton process is an important mechanism to produce gamma rays in the galactic disk, where electrons and positrons upscatter soft photons from the interstellar radiation field (ISRF). Electrons and positrons can be used interchangeably when considering inverse Compton radiation.

2.3.1 Single-Electron Case

For an electron interacting with an isotropic incident photon field at a single frequency ν_0 , the intensity is

$$I(\nu_0, \nu) = \frac{3\sigma_{Tc}}{16\gamma^4} \frac{N(\nu_0)}{\nu_0^2} \nu \left[2\nu \ln \frac{\nu}{4\nu_0\gamma^2} + \nu + 4\gamma^2\nu_0 - \frac{\nu^2}{2\gamma^2\nu_0} \right] \quad (2.46)$$

where we have written the intensity in terms of the number rather than energy of scattered photons [33].

2.3.2 Multi-Electron Population Case

Following [50], consider an isotropic monochromatic field of photons of incident energy E_0 as measured in lab frame S scattering from a beam of monoenergetic electrons of energy $\gamma m_e c^2$, also in the lab frame. Impose the condition $\gamma E_0 \ll m_e c^2$, which not only guarantees the nonrelativistic limit $h\nu_0 \ll m_e c^2$, but also Thompson scattering in the electron's rest frame S' . Assume

$$\frac{d\sigma'}{d\Omega'} = \frac{1}{4\pi} \sigma_T = \frac{2}{3} r_e^2 \quad (2.47)$$

where r_e is the classical electron radius $2.82 \cdot 10^{-13}$ cm (note, the true cross-section includes the Rayleigh form factor). The isotropic incident photon spectrum in the lab frame is

$$\mathcal{I} = \nu_0 \delta(E - E_0) \quad (2.48)$$

[50], where ν_0 is the number of photons per unit area per unit time per steradian. The frames S and S' are related by a Lorentz transformation, and I/ν^3 is a Lorentz invariant quantity, where $I = hE\mathcal{I}$ (I has units of energy per unit time per unit frequency per unit area per solid angle). By Lorentz invariance, $(I_\nu)' / (\nu')^3 = (I_\nu) / (\nu)^3$, so $(I_\nu)' = (\nu'/\nu)^3 I_\nu = (E'/E)^3 I$ and

$$\mathcal{I}' = \frac{I'}{hE'} = \frac{(E'/E)^3}{hE'} I = \frac{(E'/E)^3}{hE'} hE\mathcal{I} = (E'/E)^2 \mathcal{I} = (E'/E)^2 \nu_0 \delta(E - E_0). \quad (2.49)$$

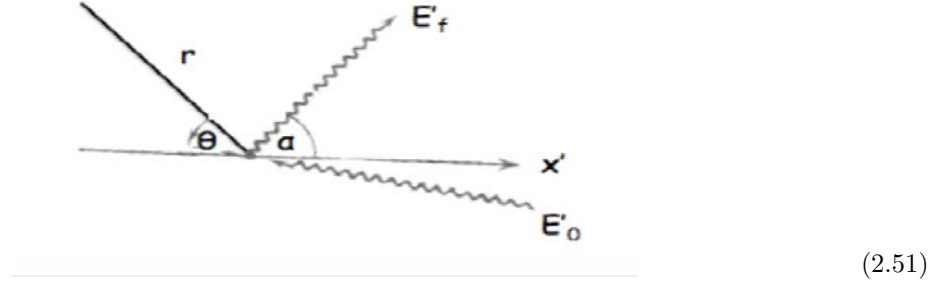


Figure 2.4: Inverse Compton scattering of a photon in electron rest frame. The photon energy changes from E'_0 to E'_f during the collision. In the coordinate system shown, r is measured from reference line at polar angle θ .

Allowing n to be the number of electrons per unit volume in the beam, we have a photon emission spectrum (analogous to Rybicki and Lightman's Eqs. 1.84 and 1.85) in S' of

$$j'((E_\nu)') = n' \sigma_T \int_{-1}^1 \mathcal{I}'((E_\nu)', \mu') d\mu' \quad (2.50)$$

where μ is the cosine of the angle between the x' -axis and the photon direction in the electron rest frame (refer to Figure 2.4) Using polar coordinates and setting the r direction antiparallel with the x' -axis ($\theta = 0$) and defining the angle between the emitted photon wavevector and the x' -axis as α' , we have $\mu' = \cos \alpha' = -\cos \theta$ and $d\Omega = d\mu' d\phi$, where ϕ is the azimuthal angle. Assuming photons scatter elastically $E' = (E_f)'$ and using the Doppler formula

$$E = \gamma E' \left(1 + \frac{v}{c} \mu' \right) \quad (2.52)$$

, the incident and scattered photon intensity has the same angular distribution in the electron rest frame:

$$\begin{aligned} \mathcal{I}'(E', \mu') &= \mathcal{I}'((E_f)', \mu') = \nu_0 ((E_f)'/E_0)^2 \delta \left(\gamma (E_f)' \left(1 + \frac{v}{c} \mu' \right) - E_0 \right) \\ &= \frac{\nu_0}{\gamma \beta (E_f)'} \left(\frac{(E_f)'}{E_0} \right)^2 \delta \left(\mu' - \frac{E_0 - \gamma (E_f)'}{\gamma \beta (E_f)'} \right) \end{aligned} \quad (2.53)$$

Then

$$j'((E_f)') = n' \sigma_T \int_{-1}^1 \frac{\nu_0}{\gamma \beta (E_f)'} \left(\frac{(E_f)'}{E_0} \right)^2 \delta \left(\mu' - \frac{E_0 - \gamma (E_f)'}{\gamma \beta (E_f)'} \right) d\mu' \quad (2.54)$$

$$= \begin{cases} \frac{n' \sigma_T \nu_0 (E_f)'}{2\gamma\beta E_0^2}, & \frac{E_0}{\gamma(1+\beta)} < (E_f)' < \frac{E_0}{\gamma(1-\beta)} \\ 0, & \text{otherwise} \end{cases} \quad (2.55)$$

where the argument of the δ function was set to 0 for $\mu' = -1$ and $\mu' = 1$ to get the boundary of the support of $(j(E_f)')$. To write this result in the lab frame (assuming $\gamma \gg 1$), use the Lorentz invariance of j/ν^2 , where $j = hEj$:

$$\frac{j'}{(\nu')^2} = \frac{j}{\nu^2} \implies \frac{hE'j'}{(\nu')^2} = \frac{hEj}{\nu^2} \implies j = \frac{E'}{E} \frac{\nu^2}{(\nu')^2} j' = \frac{E'}{E} \frac{E^2}{(E')^2} j' = \frac{E}{E'} j' \quad (2.56)$$

$$j((E_f), \mu_f) = \frac{E}{E'} j'((E_f)') \quad (2.57)$$

$$\implies j((E_f), \mu_f) = \begin{cases} \frac{n \sigma_T \nu_0 E_f}{2\gamma^2 \beta E_0^2}, & \frac{E_0}{\gamma^2(1-\beta\mu_f)(1+\beta)} < E_f < \frac{E_0}{\gamma^2(1-\beta\mu_f)(1-\beta)} \\ 0 & \end{cases} \quad (2.58)$$

where we have used $n' = n/\gamma$ to relate the beam densities in the two frames and the Doppler formula $(E_f)'/E_f = \gamma(1 - \beta\mu_f)$.

2.3.3 Klein-Nishina Regime

For a theoretical treatment of inverse Compton radiation including polarization and absorption, it is helpful to consider 3 frames: the Galaxy Frame, the Center of Momentum (CoM) Frame and the Electron Rest Frame (ERF), which will be denoted by 0, 1 and 2 primes, respectively. In the spirit of high-energy particle physics, we change the notation from above and set $m_e = c = \hbar = 1$. Furthermore, we work in the Klein-Nishina limit:

$$\begin{aligned} \gamma &\gg 1 \\ \tilde{\nu}' &\equiv \frac{\gamma'}{\gamma} \sim \mathcal{O}(1) \end{aligned} \quad (2.59)$$

Moreover, define $\tilde{\nu}'_0 = \gamma' \nu'_0 \sim 1\text{MeV}$. In this limit, photons tend to collide head on with the lepton in the Galaxy Frame. Photons approach the lepton in the ERF, and recoil in the same direction as the electron in the CoM as in Figure 2.5.

In the e^- rest frame,

$$\nu' = \frac{\nu'_0}{1 + (1 - \hat{n} \cdot \hat{n}'_0)^2 \nu'_0} \quad (2.60)$$

the unpolarized Klein-Nishina differential cross section is

$$\frac{d\sigma}{d\Omega'} = \frac{r_e^2}{2} \left(\frac{\nu'}{\nu_0} \right)^2 \left(\frac{(\nu'_0 - \nu')^2}{\nu' \nu'_0} + 1 + (\hat{n}'_0 \cdot \hat{n}')^2 \right) \quad (2.61)$$

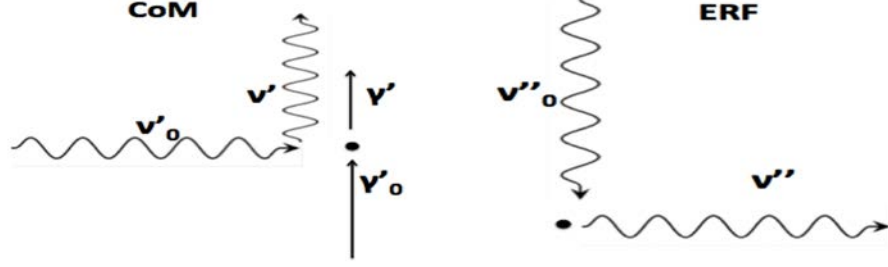


Figure 2.5: Inverse Compton scattering in Klein-Nishina limit in ERF (left) and CoM (right).

and the polarized Klein-Nishina formula reads

$$\frac{d\sigma}{d\Omega'} = \frac{r_e^2}{4} \left(\frac{\nu'}{\nu_0} \right)^2 \left(\frac{(\nu'_0 - \nu')^2}{\nu' \nu'_0} + 4(\hat{\epsilon}'_0 \cdot \hat{\epsilon}')^2 \right) \quad (2.62)$$

A useful Lorentz invariant is the differential probability

$$d\mathcal{P} = \mathcal{N}_0 \nu_0^2 d\nu'_0 d\Omega'_0 \frac{d\sigma}{d\Omega'_0} \delta(\nu'' - \nu'_s) d\nu'' d\Omega''_0 dt'' \quad (2.63)$$

where \mathcal{N}_0 is the Lorentz invariant soft photon occupation number. In the CoM frame,

$$d\mathcal{P} = \mathcal{N}_0 \nu_0'^2 d\nu'_0 d\Omega'_0 (1 - \hat{n}'_0 \cdot \hat{u}') \frac{d\sigma}{d\Omega''} \delta(\nu' - \nu'_s) \quad (2.64)$$

where

$$\nu'_s = \frac{\mathcal{D}' \nu'_0}{\mathcal{D}'_0 + \nu'_0 (1 - \hat{n}'_0 \hat{n}'')} \quad (2.65)$$

In the unpolarized axisymmetric case,

$$\hat{n}''_0 = -\hat{u} = -\hat{n}'$$

$$|d\Omega''| \rightarrow \frac{2\pi d\mathcal{D}'}{\gamma}$$

$$|d\Omega'_0| \rightarrow \frac{2\pi d\mathcal{D}'_0}{\gamma' \mathcal{D}'_0{}^2}$$

so the power per unit frequency becomes

$$\begin{aligned} p'_{\nu'} &= \frac{2\pi\nu'}{\gamma'} \int d\nu'_0 d\Omega'_0 \frac{I'_{\nu'_0 \Omega'_0}}{\nu'_0} \frac{1}{\gamma' \mathcal{D}'} \frac{\nu'_0 \mathcal{D}'^2}{\nu' \mathcal{D}'_0} \frac{d\sigma}{d\Omega''} \\ &= \int d\nu'_0 \int_{\frac{1}{2\gamma'}}^{\frac{2(\gamma' - \nu')\nu'_0}{\nu'}} \frac{d\mathcal{D}'_0}{\gamma' \mathcal{D}'_0{}^2} \frac{I'_{\nu'_0 \Omega'_0}}{\nu'_0{}^2} \left(\frac{\nu'^2}{\gamma'(\gamma' - \nu')} + 1 + \left(\frac{\mathcal{D}'_0 \nu'}{(\gamma' - \nu')\nu'_0} - 1 \right)^2 \right) \end{aligned} \quad (2.66)$$

for $\gamma' > \frac{1}{2} \left[\nu' + \sqrt{\nu'^2 + \frac{\nu'}{\nu_0}} \right] \equiv \gamma_{\min}$. Writing the CoM Frame transformed incident photon energy $\tilde{\nu}'_0 \equiv \gamma' \nu'_0$, outgoing photon energy $\tilde{\nu}' \equiv \frac{\nu'}{\gamma'}$ and $\eta \equiv 1 - \mu'_0$,

$$p'_{\nu'} = 2\pi^2 r_e^2 \tilde{\nu}' \int d\tilde{\nu}'_0 \int_{\frac{\tilde{\nu}'}{2(1-\tilde{\nu}')}}^2 d\eta \frac{I'_{\nu'_0 \Omega'_0}}{\tilde{\nu}'_0{}^2} \left(\frac{\tilde{\nu}'^2}{1-\tilde{\nu}'} + 1 + \left(\frac{\tilde{\nu}'}{(1-\tilde{\nu}')\tilde{\nu}'_0 \eta} - 1 \right)^2 \right) \quad (2.67)$$

To transform intensity from the Galaxy Frame to the CoM frame, use

$$I'_{\nu' \Omega'}(\nu', \hat{n}') = \mathcal{D}^{-3} I_{\nu \Omega}(\nu, \hat{n}) \quad (2.68)$$

In the case of an isotropic soft photon distribution,

$$p'_{\nu'} = \frac{\pi^2 r_e^2 \nu'}{2\gamma'^2} \int d\nu'_0 \frac{u'_{\nu'_0}}{\nu'^2_0} \left(\frac{\mathcal{D}'_0 \nu'}{(\gamma' - \nu')\nu'_0} - 1 \right)^2 \quad (2.69)$$

Further restricting to monochromatic soft photons in the Thompson limit gives

$$p'_{\nu'} = 3\sigma_T \frac{u'_0}{\nu'_0} (x + x^2 - 2x^3 + 2x^2 \ln x) \quad (2.70)$$

where $x \equiv \frac{\tilde{\nu}}{4\tilde{\nu}'_0}$, $p' = \int d\nu' p'_{\nu'} = \frac{4}{3} \sigma_T \gamma'^2 u'$ (scattering rate = $\sigma_T \frac{u'}{\nu'_0}$). Momentarily restoring c to compare with the intensity $I'(\nu'_0, \nu') = 3\sigma_T c N(\nu_0) \left[\frac{\nu'}{4\gamma'^2 \nu'_0} + \frac{\nu'^2}{16\gamma'^4 \nu'^2_0} - \frac{\nu'^3}{32\gamma'^6 \nu'^3_0} + \frac{\nu'^2}{8\gamma'^4 \nu'^2_0} \ln \frac{\nu'}{4\nu'_0 \gamma'^2} \right]$ due to a single electron in the Thompson limit from Eq. 2.46, we recover $p'_{\nu'} = \frac{u'_0}{\nu'_0 N(\nu'_0)} I'(\nu'_0) = I'(\nu'_0)$ (where we have used $N(\nu_0) = \frac{u_0}{\nu_0}$).

To transform from CoM frame emission to Galaxy Frame emission, use

$$j_{\nu \Omega}(\nu, \hat{n}) = \mathcal{D}^2 j'_{\nu' \Omega'}(\nu', \hat{n}'). \quad (2.71)$$

as with synchrotron radiation.

2.3.4 Pair Production

Unlike synchrotron radiation, inverse Compton radiation is mainly modulated by the process of pair production, which serves as opacity in this case. The total cross section for pair production is given in the unpolarized case by [7]

$$\sigma_{\gamma\gamma \rightarrow e^+e^-} = \frac{3\sigma_T}{16} (1-v) \left((3-v^4) \ln \left[\frac{1+v}{1-v} - 2v(1-v^2) \right] \right), \quad (2.72)$$

where v is the electron or positron speed in the photon center-of-momentum frame and $1-\eta$ is the cosine of the scattering angle. Substituting $\xi = 1/(1-v^2) = \frac{\tilde{\nu}\nu_0\eta}{2}$, the absorption coefficient for pair

production can be written as

$$\begin{aligned} \chi_{\gamma\gamma \rightarrow e^+e^-} = \frac{3\pi\sigma_T}{\tilde{\nu}^2} \int_{\nu^{-1}}^{\infty} \frac{d\tilde{\nu}_0}{\tilde{\nu}_0^3} \int_1^{\tilde{\nu}\tilde{\nu}_0} \frac{d\xi}{\xi^2} \left[(2\xi(\xi+1)-1) \ln(\xi^{1/2} + (\xi-1)^{1/2}) - \xi^{1/2}(\xi-1)^{1/2} \right] \\ \times I_{\nu_0\Omega}(\nu_0, \frac{2\xi}{\tilde{\nu}\tilde{\nu}_0}). \end{aligned} \quad (2.73)$$

The non-axisymmetric case introduces an integral over azimuth. We do not concern ourselves with the extension to polarization here since the observations of polarized inverse Compton radiation are currently at a rudimentary level.

Chapter 3

3D General Relativistic Magnetohydrodynamic Simulations

That kiloparsecs long streams of relativistic cosmic rays can form stable jets in denser AGN environments subject to innumerable MHD instabilities would be difficult to believe if not borne out by simulations. Simulations reveal a key ingredient to jet stability is a magnetically arrested disk whose magnetic flux has saturated the black hole so that the system attains equilibrium between gravity and magnetic pressure [38] [39]. These investigations produced Poynting flux (electromagnetic) jets powered by rapidly rotating black holes threaded by vertical flux via the Blandford-Znajek mechanism. Though no longer state-of-the-art, the simulation used in this work captures many aspects of the kinematics and dynamics of a Poynting flux jet launched from a magnetically arrested disk remarkably well. For example, numerical density floors serve a role analogous to particle injection by pair production in the near jet region close to the black hole. In the outer jet region, we will see the phenomenon of entrainment reflected in the simulation by a decelerating jet. A qualitative cutoff between the force-free and MHD regimes of the simulation will be given at the end of this chapter. First, it is helpful to acquire a basic sense of the simulation parameters quantitatively.

3.1 Idumps Investigations

Simulation data, or time series of physical quantities evolved under GRMHD equations in a region, are conveniently stored as a columns of floats in binary (or larger text) files with char header that we refer to as "Idumps" files here. The Idump sizes used in this work are described in Table 1, and the format of files of lattice quantities are given in Table 2.

Table 1: Datablock size specifications

idump	Paper	Spacetime Lattice Pixels	Spacetime Extent
MB09D Idump1	MB09&MTB12	32x32x128x83	435Mx435M x933Mx1660M
MB09D Idump2	MB09&MTB12	256x256x256x1665 or 100x100x100x1665	80Mx80M x200Mx1664M
MB09D Idump3	MB09&MTB12	256x256x256x1665	80Mx80M x1400Mx1664M
MB09D Idump 4	MB09&MTB12	256x256x256x1665	320Mx320M x1400Mx1664M

Table 2: File formats for datablocks on remote server

idump	Type	Spacetime Lattice Pixels	File Size (Single Timestep)
MB09D Idump2	Text	256x256x256x1665	2.63GB
MB09D Idumps 2,3 & 4	Binary	256x256x256x1665	939.5MB
MB09D Idump 2	Text	100x100x100x1665	253MB
MB09D Idump 2	Binary	100x100x100x1665	56MB

The lower resolution Idump1 is conveniently stored in URLs created by Jonathan McKinney. The choice to IDumps 2,3 and 4, which are all stored on SLAC computing clusters, depends on whether the performance goal is dynamic range captured or resolution. The particular idump used to generate images in the following may not be stated if it can be inferred from the scale and features of the images.

The simulation MB09D has the following state variables: rest mass density ρ , the gas internal energy u_g , the velocity 4-vector $u^\mu = (\gamma c, \gamma \vec{v})$ and the fluid comoving magnetic field 4-vector b^μ . MB09D also has parameters: dimensionless spin $a/M = .92$, a poloidal field geometry such that $A_\phi \propto (\rho_0 - \rho_{\text{cut}})$, where, e.g., $\rho_{\text{cut}} \sim .25\rho_{\text{max}} = .25$, thermal to magnetic pressure ratio $\beta_{\text{min}} = (p_g/p_b)_{\text{min}} = 14$ (so $p_g \geq 14p_b$), maximum thermal to maximum magnetic pressure ratio $\beta_{\text{rat-of-max}} = p_{g,\text{max}}/p_{b,\text{max}} = 100$ (so $p_{g,\text{max}} = 100p_{b,\text{max}}$), average thermal to magnetic pressure ratio $\beta_{\text{rat-of-max}} = p_{g,\text{av}}/p_{b,\text{av}} = 530$ (so $p_{g,\text{av}} = 530p_{b,\text{av}}$), disk geometric half-angular thickness $\theta_{\text{rmax}}^d = .18$, where

$$\theta^d = (\langle (\theta - \theta_0)^2 \rangle_\rho)^{1/2} = \left(\frac{\int dA_{\theta\phi} \rho (\theta - \theta_0)^2}{\int dA_{\theta\phi} \rho} \right)^{1/2},$$

thermal half-angular thickness $\theta_{\text{rmax}}^t = .24$, where

$$\theta^t = \tan^{-1} \frac{\langle c_s \rangle_w}{\langle v_{\text{rot}} \rangle_w},$$

initial ($t = 0$) $S_{\text{d,MRI}} = 2r\theta^d/\lambda_{\theta\text{MRI}}$ and $\lambda_{\text{dMRI}} = 2\pi|v_{\text{d,A}}|/|\Omega_{\text{rot}}| = 3.4$ (inside) and 16 (outside) and final time $T_f = 5662r_g/c$. The magnetorotational instability in a differentially rotating (higher angular speed but lower angular momentum at smaller radius) disk results from perturbations $\delta B \sim e^{ikz}$ causing waves that push disk elements inward (outward) that then are decelerated (accelerated) by magnetic tension. This instability can be suppressed by polar magnetic field in [39], allowing stable jets to form. For numerical stability, the density floors $\rho \geq 0.02b^2$ and $u_g \geq 10^{-3}b^2$ are used [39].

3.2 General Relativistic Magnetohydrodynamic Equations

Accretion flows in magnetized plasma are well described by fluid dynamical equations for ρ , u_g , the velocity 4-vector u^μ and b^μ . In what follows in this chapter, we set $c=1$. Fluid elements may approach relativistic ($v \approx 1$) speeds upon being accelerated by numerous sources, including gravitational fields near the centers of galaxies, plasma currents and magnetic reconnection. Thus one must take care to keep track of special relativistic effects when dealing with astrophysical magnetohydrodynamic (MHD) flows. For example, by relating comoving magnetic field to Galaxy Frame magnetic field via

$$b^\mu = (B^\mu + (\vec{u} \cdot \vec{B})u^\mu)/u^t \quad (3.1)$$

, we see that \vec{u} enters the formula for magnetic energy density $u_b = (b^\mu b_\mu)/2$ in terms of the field measured in the Galaxy Frame, viz.

$$\begin{aligned} b^\mu b_\mu &= \frac{B^\mu B_\mu + 2(\vec{u} \cdot \vec{B})B_\mu u^\mu + u^\mu u_\mu (\vec{u} \cdot \vec{B})^2}{(u^t)^2} \\ &= \frac{B^2 + 2B_\mu u^\mu (\vec{u} \cdot \vec{B}) + u^2 (\vec{u} \cdot \vec{B})^2}{(u^t)^2} \\ &= \frac{B^2 - 2B^t u^t (\vec{u} \cdot \vec{B}) + 2(\vec{B} \cdot \vec{u})(\vec{u} \cdot \vec{B}) - (u^t)^2 (\vec{u} \cdot \vec{B})^2 + v^2 (u^t)^2 (\vec{u} \cdot \vec{B})^2}{(u^t)^2} \end{aligned}$$

Assuming the field follows the flow, $B^t = 0$, so

$$\begin{aligned} b^\mu b_\mu &= \frac{B^2 + 2(\vec{B} \cdot \vec{u})^2 - (u^t)^2 (\vec{u} \cdot \vec{B})^2 + v^2 (u^t)^2 (\vec{u} \cdot \vec{B})^2}{(u^t)^2} \\ &= \frac{B^2 + 2(\vec{B} \cdot \vec{u})^2 - \frac{1}{1-v^2} \left((\vec{u} \cdot \vec{B})^2 [1 - v^2] \right)}{\frac{1}{1-v^2}} \\ &= (1 - v^2) [B^2 + (\vec{u} \cdot \vec{B})^2] \end{aligned}$$

As the MHD flows relevant for this work occur around the strong gravitational curvature of black holes, we must also invoke general relativity– which gives us even more indices to worry about!

The magnetohydrodynamic equations for an astrophysical plasma

$$\begin{aligned} (\rho u^\mu)_{;\mu} &= 0 \\ (T^\mu_\nu)_{;\mu} &= 0 \\ (R^\mu_\nu)_{;\mu} &= 0 \end{aligned} \tag{3.2}$$

where

$$T^\mu_\nu = (\rho + u_g + p_g + b^2) u^\mu u_\nu + (p_g + (1/2)b^2) \delta^\mu_\nu - b^\mu b_\nu$$

[51] can be conceptualized as conservation equations for mass, energy and momentum, respectively, and the rest mass energy density ρ does not include energy, curvature, etc. In general relativistic form as above, it is possible to analyze effects such as gravitational redshift and inertial frame-dragging by the ergosphere inside the static limit for which objects must move at the speed of light to overcome frame dragging.

The simulation used to solve the GRMHD equations in this thesis is taken from [38] and is based upon the high-accuracy relativistic modeling (*HARM*) code of [21]. It is further analyzed in [39] where it is called MB09D. It features a modestly spinning hole, a thick disk (with height comparable to radius) and a dipolar polar initial magnetic field.

3.2.1 Simulation Kinematic and Dynamic Variables

To get a "picture"– so to speak– of the evolution of the kinematic (motion) and dynamic (force and energy) variables in the simulation MTB12, first consider the slices of Idump 3 at Galaxy Frame times $t_{\text{Gal}} = 1500M$ and $2000M$ through the equatorial plane (Figures 3.1 and 3.2) and through a longitudinal plane (Figures 3.5 and 3.6), at $T_{\text{Gal}} = 2000M$ and $2500M$. At all times, the accretion disk is prominent (especially in ρ and u_g), and the jet has relatively low densities and field values. The infall of disk magnetic field is arrested at around $5M$. The transverse velocity components v_x and v_y are approximately related by an azimuthal phase shift of $\pi/2$, as are the transverse magnetic field components B_x, B_y . The longitudinal component of velocity v_z decreases (in absolute value) sharply

from $T_{\text{Gal}} = 1500M$ to $2000M$ as disk magnetorotational and interchange instabilities diminish to give rise to stable jets. The flow is quasi-stationary, though there is a steady decrease in rest mass density ρ at small cylindrical radius as mass is entrained from disk into the jet. At $z = 50M$, the jet has accelerated away from the disk as its core becomes filled with vertical magnetic field as seen in the plots of v_z and B_z in Figure 3.3. In Figure 3.4 of transverse ρ profiles at a small height—say $25M$ —over the equatorial plane, the disk density is seen to pulse and quiver from $T_{\text{Gal}} = 2000M$ to $T_{\text{Gal}} = 2500M$ as the area near the black hole is evacuated by the expanding jet.

In the galaxy frame $x_{\text{Gal}}-y_{\text{Gal}}-z_{\text{Gal}}$ Cartesian system datablocks, the upper half $x_{\text{Gal}}-z_{\text{Gal}}$ planes at $T = 2000M$ and $2500M$ in Figures 3.5 and 3.6, respectively, reveal an advancing relativistic flow surrounded by toroidal magnetic field propagating in the opposite sense of the toroidal component of the flow. In the bottom half of the simulation, the z -component of the curl or \vec{B} changes sign, as seen in Figure 3.16, and the toroidal magnetic field rotates with the flow. Moreover, the jet accelerates away from the disk due to magnetic pressure $\sim B_\phi^2$ (picture B_ϕ as a coiled spring).

The 2D-sideviews of ρ , v_z , B_x , B_y , and B_z as well as the 1D-transverse profiles of ρ , v_z , and B_z of Figure 3.8 suggest the jet collimation at $z = 100M$ is more consistent with magnetic tension (provided there is current outside the jet return current due to B_ϕ "hoop" stress than ram pressure from the surrounding medium. The transverse profile of the magnetic field component B_z shows that the flux is mostly confined to a narrow core within the jet and contains small side lobes. That the jet flux is mostly anchored at the horizon is characteristic of Blandford-Znajek jets. Electromagnetic tension is small in the central core with uniform magnetic field. This core expands outward as the jet advances due to electromagnetic stress.

The transverse profiles of v_z at increasing altitudes in Figure 3.7 are characterized by two types of inflection points: on the side, where the jet is being pinched, and on the cylindrical core (spine), where a cavity forms from mass loading.

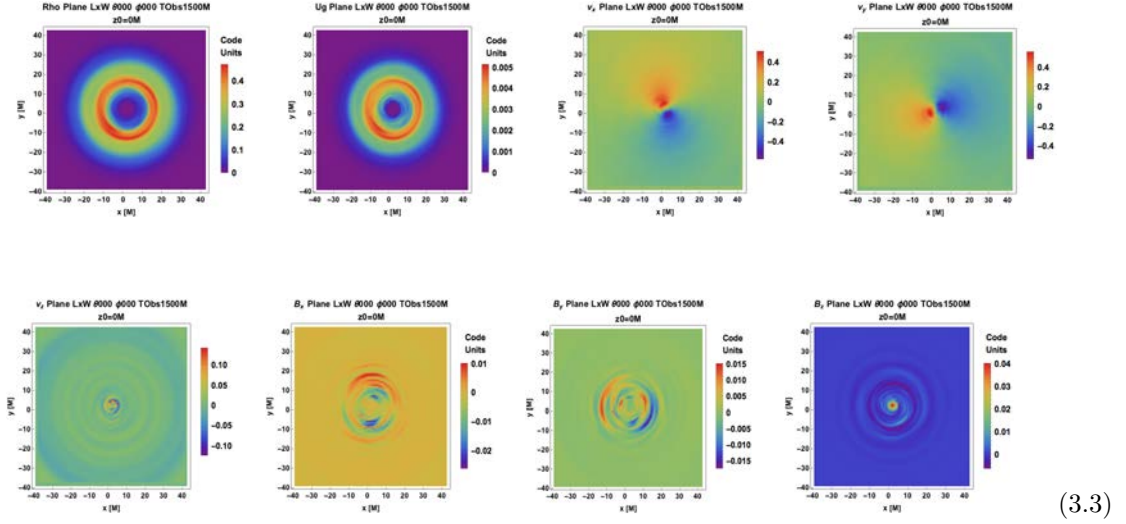


Figure 3.1: Density plots of (from top left to bottom right) ρ , u_g , v_x , v_y , v_z , B_x , B_y and B_z at simulation time $T = 1500M$ at height $z_0 = 0M$ and polar and azimuthal angles $(\theta, \phi) = (0^\circ, 0^\circ)$. The velocity components are in units of c . The rest mass density and gas energy density are concentrated on the disk torus. The transverse magnetic fields are ordered and toroidal, though B_z and the velocity components are not at this altitude.

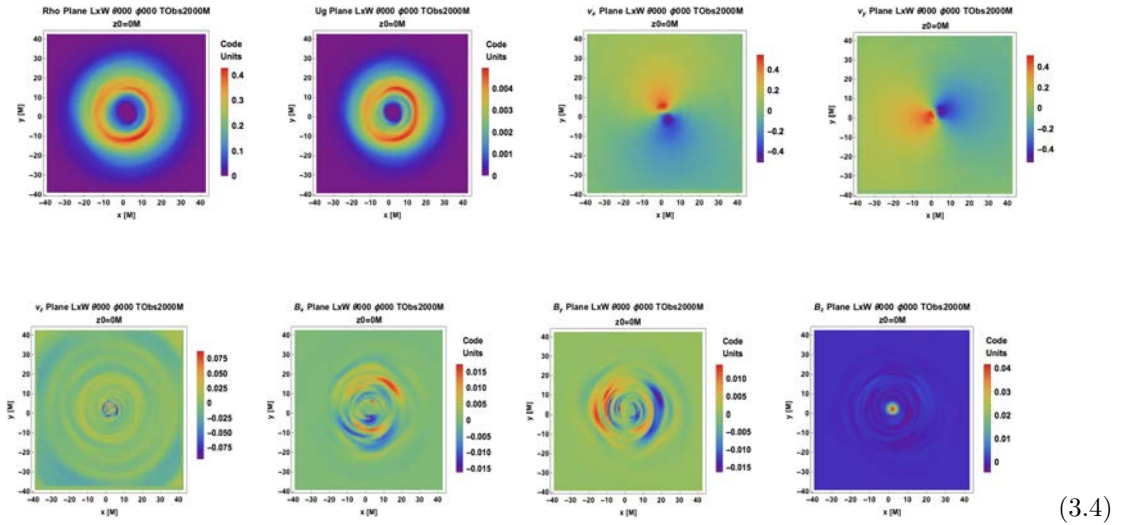


Figure 3.2: Density plots of (from top left to bottom right) ρ , u_g , v_x , v_y , v_z , B_x , B_y and B_z at simulation time $T = 2000M$ at height $z_0 = 0M$ and polar and azimuthal angles $(\theta, \phi) = (0^\circ, 0^\circ)$. The velocity components are in units of c .

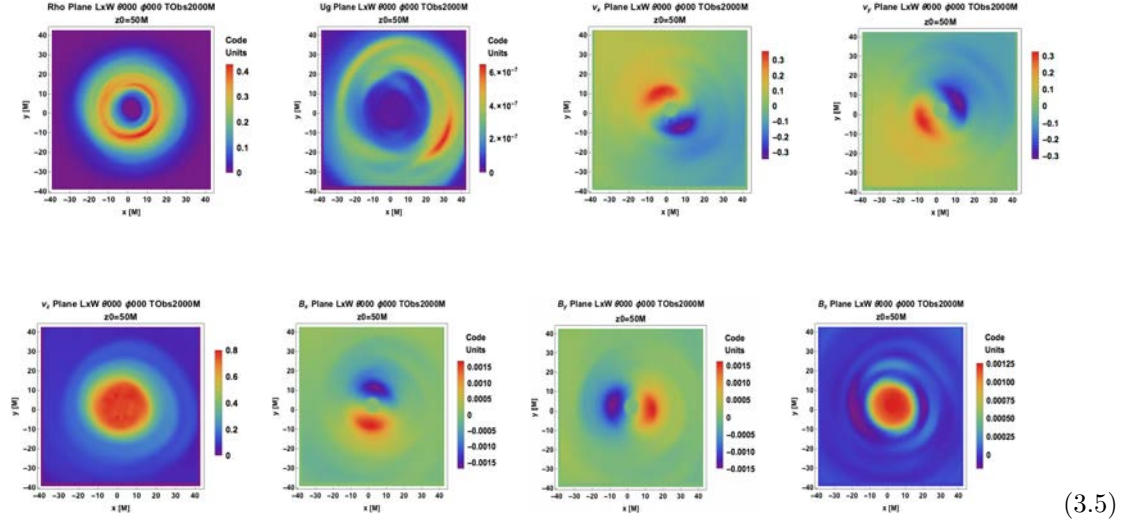


Figure 3.3: Density plots of (from top left to bottom right) ρ , u_g , v_x , v_y , v_z , B_x , B_y and B_z at simulation time $T = 2000M$ at height $z_0 = 50M$ and polar and azimuthal angles $(\theta, \phi) = (0^\circ, 0^\circ)$. The velocity components are in units of c . The locus of highest gas energy density has migrated to larger cylindrical radius on the disk torus. The transverse magnetic and velocity fields are ordered and toroidal, while B_z and v_z are positive.

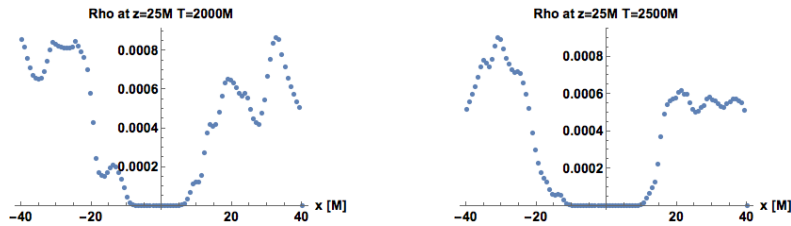


Figure 3.4: Transverse profiles for ρ at $t_{\text{Gal}} = 2000M$ (left panel) and $t_{\text{Gal}} = 2500M$ (right panel). At this small altitude, the central few M have almost no density, but density rises sharply outside.

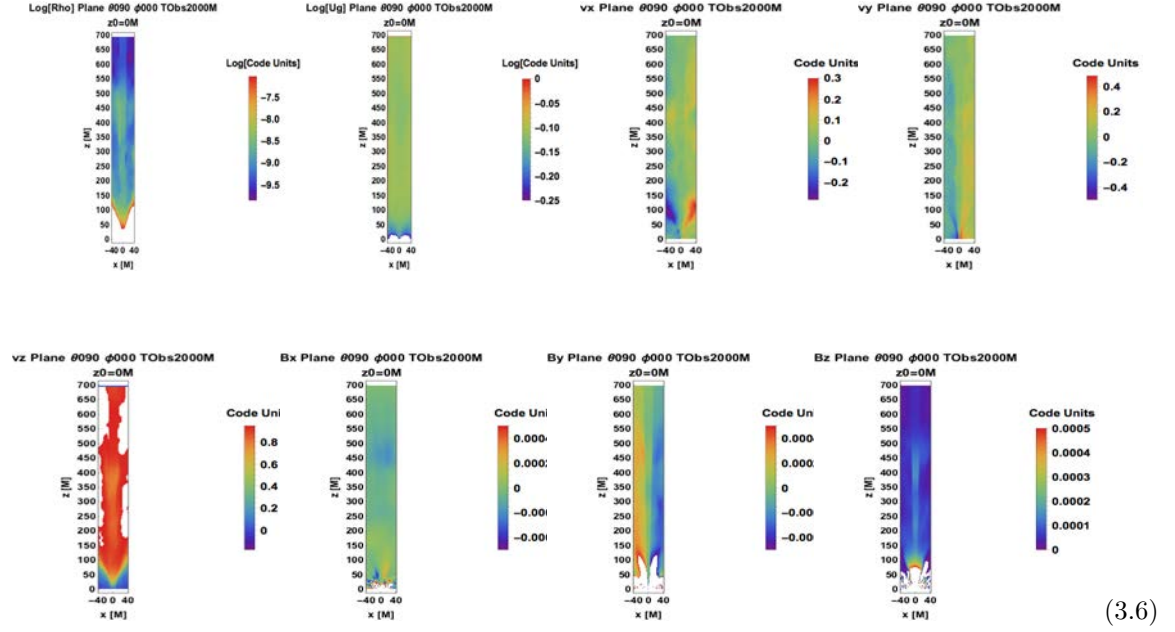


Figure 3.5: Density plots of (from top left to bottom right) ρ , u_g , v_x , v_y , v_z , B_x , B_y and B_z at simulation time $T = 2000M$ on the $y = 0M$ plane and polar and azimuthal angles $(\theta, \phi) = (90^\circ, 0^\circ)$. The rest mass density and gas energy density are very large at low altitude near the disk. On this plane the radial component of \vec{v} and the toroidal component of \vec{B} show the greatest variation among the transverse fields, and v_z and B_z are positive.

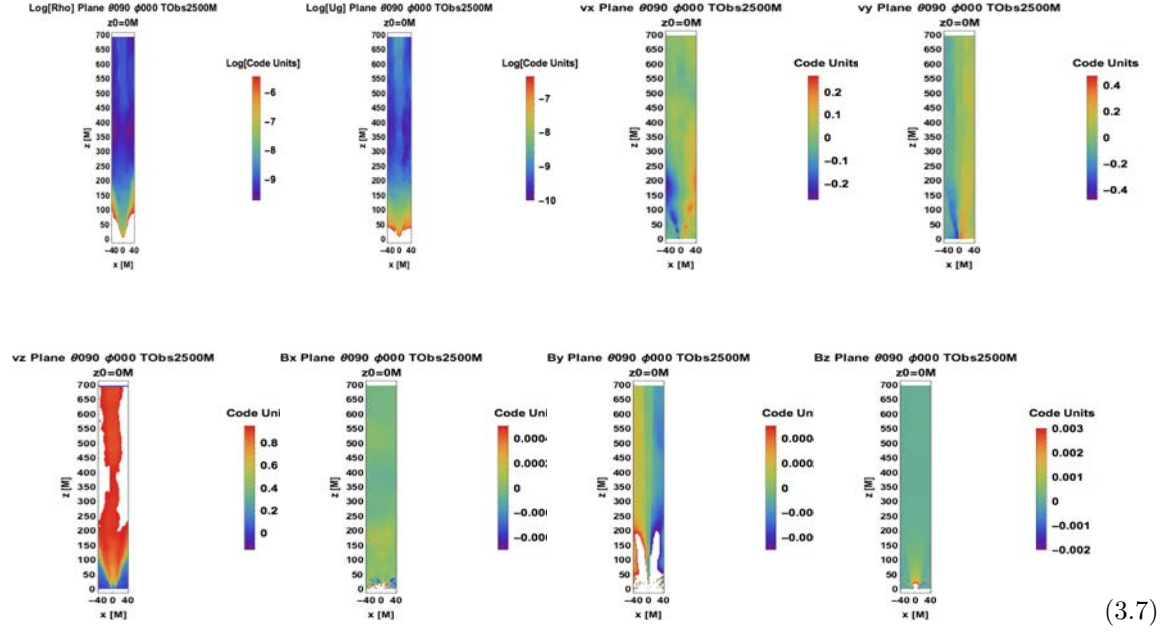


Figure 3.6: Density plots of (from top left to bottom right) ρ , u_g , v_x , v_y , v_z , B_x , B_y and B_z at simulation time $T = 2500M$ on the $y = 0M$ plane and polar and azimuthal angles $(\theta, \phi) = (90^\circ, 0^\circ)$.

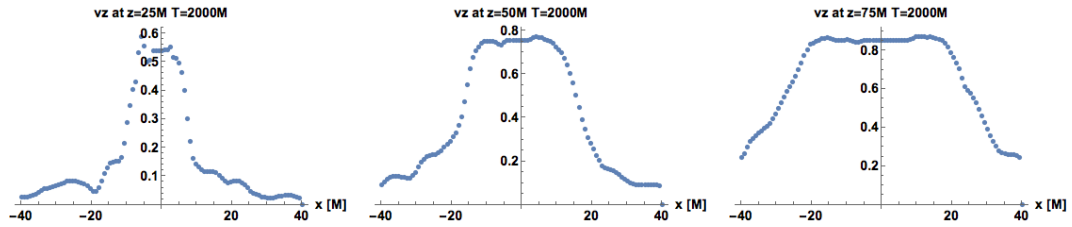


Figure 3.7: Transverse profiles for v_z at $t_{\text{Gal}} = 2000M$ at $z = 25M$ (left panel), $z = 50M$ (middle panel) and $z = 75M$ (right panel). The boundary layers (highly sloped portions) of the plots are associated with large velocity shear.

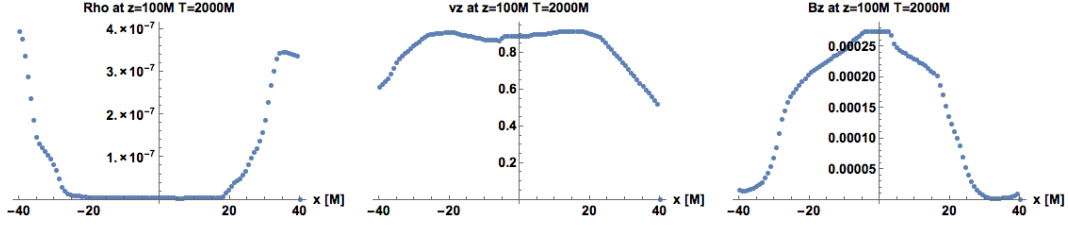


Figure 3.8: Transverse profiles for ρ (left panel), v_z (middle panel) and B_z (right panel) at $t_{\text{Gal}} = 2000M$.

To visually obtain an understanding of the relativistic jet emanating from the poles of the black hole in MTB12, one can study plots of kinematic and dynamic variables including the longitudinal (jet) axis. The jet expansion is most clear in the Lorentz factor profiles of Figure 3.9 generated from IDump 1. The Doppler factor from the high resolution IDump 2 on a longitudinal plane highlights the approaching and suppresses the receding portions of the accretion flow in 3.11. The large scale velocity field can be seen from the low resolution simulation at various times in Figure 3.10. Smaller scale variability in the velocity and magnetic fields can be analyzed from the 3D-vector plots from IDump 3 in 3.12 in which the magnetic field is displayed and in Figure 3.13, in which the velocity field and the component of velocity field perpendicular to the magnetic field is displayed in a $60M \times 60M \times 60M$ box. Though the latter two 3D plots have compatible directions, the agreement is not exact due to artificial numerical density floors affecting MHD variables ρ and u_g in Equation 3.2.

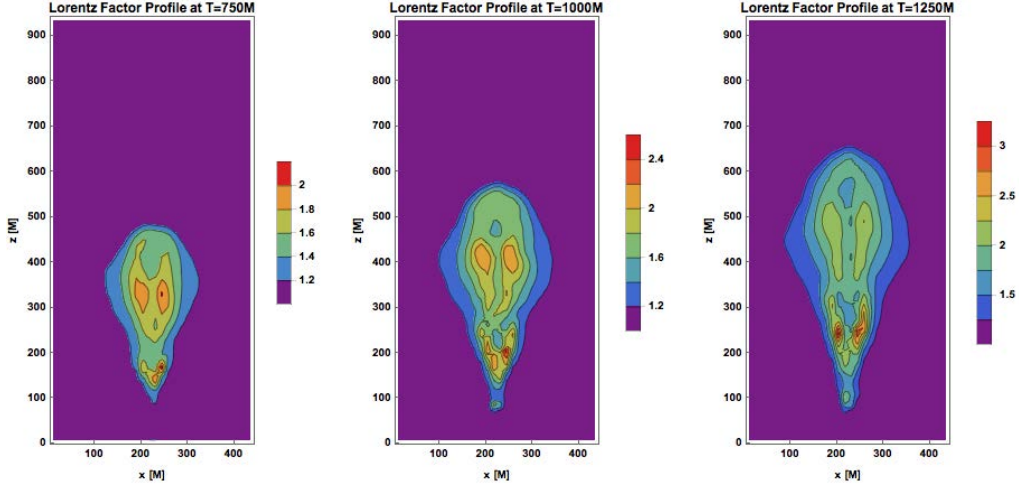


Figure 3.9: Lorentz factor profiles for xz -plane at $t_{\text{Gal}} = 750M$ (left panel), $t_{\text{Gal}} = 1000M$ (middle panel) and $t_{\text{Gal}} = 1250M$ (right panel) planes for $t_{\text{Gal}} = 1300M$. The jet can be considered a transient at these times.

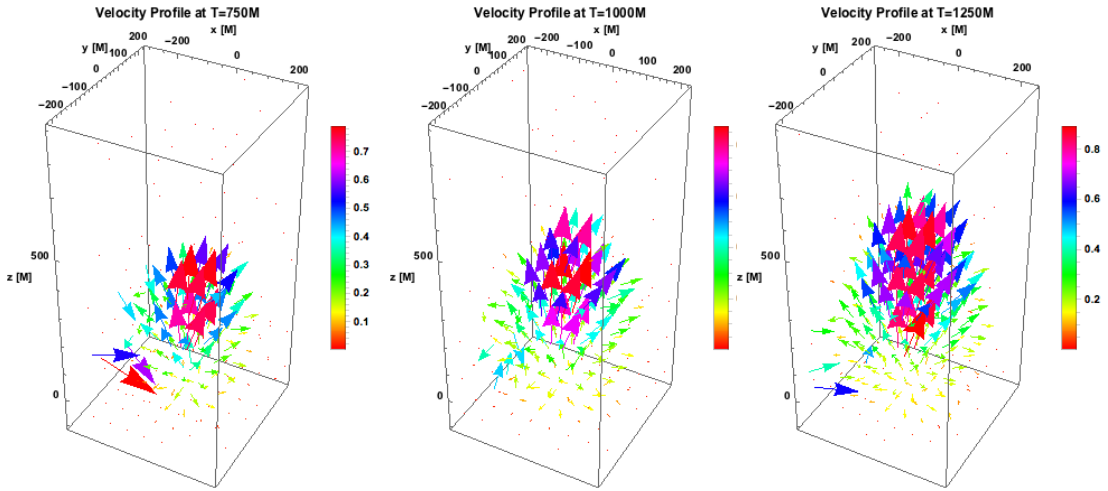


Figure 3.10: Velocity 3D vector field at $t_{\text{Gal}} = 750M$ (left panel), $t_{\text{Gal}} = 1000M$ (middle panel) and $t_{\text{Gal}} = 1250M$ (right panel). At large radius, jet velocity in the run idumps1 has greater poloidal component than toroidal component. Near the equator, the flow velocity has significant toroidal component.

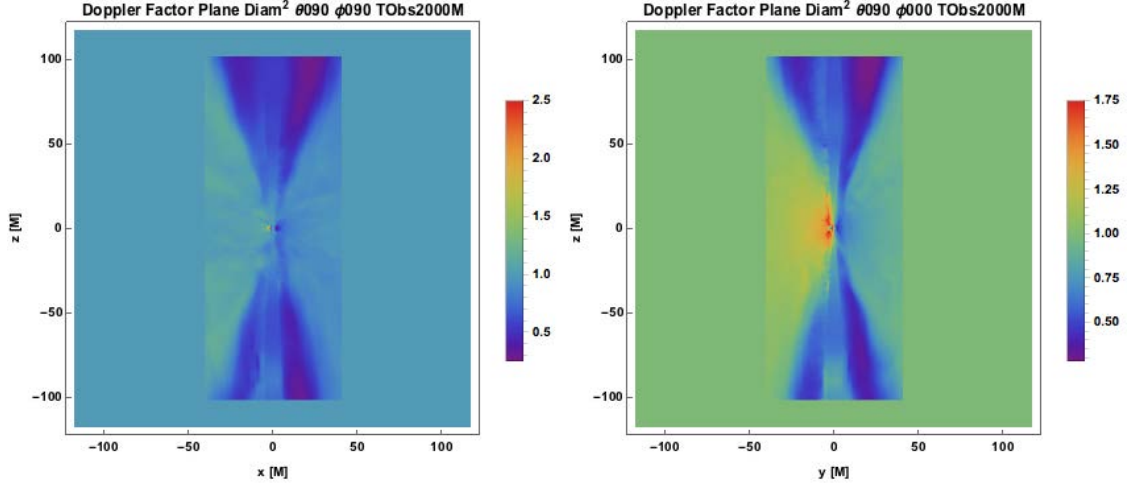


Figure 3.11: Doppler factor profiles for xz-plane at $t_{\text{Gal}} = 750M$ (left panel), $t_{\text{Gal}} = 1000M$ (middle panel) and $t_{\text{Gal}} = 1250M$ (right panel).

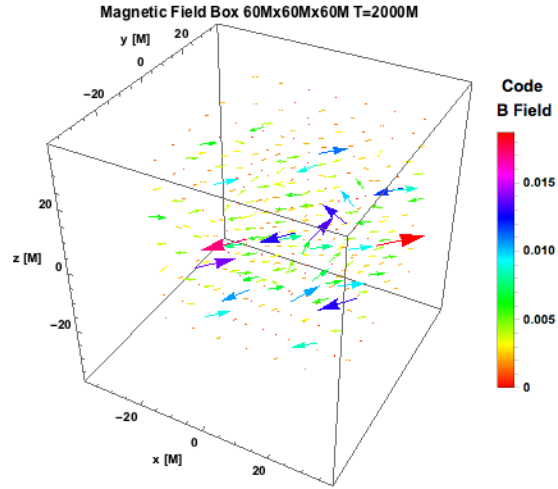


Figure 3.12: Magnetic field 60Mx60Mx60M in a small box at the center of the high resolution 80Mx80Mx200M simulation region. The poloidal component dominates at the disk, and the toroidal component is relatively large away from the disk. The latter component has negative angular velocity about the z_{Gal} -axis

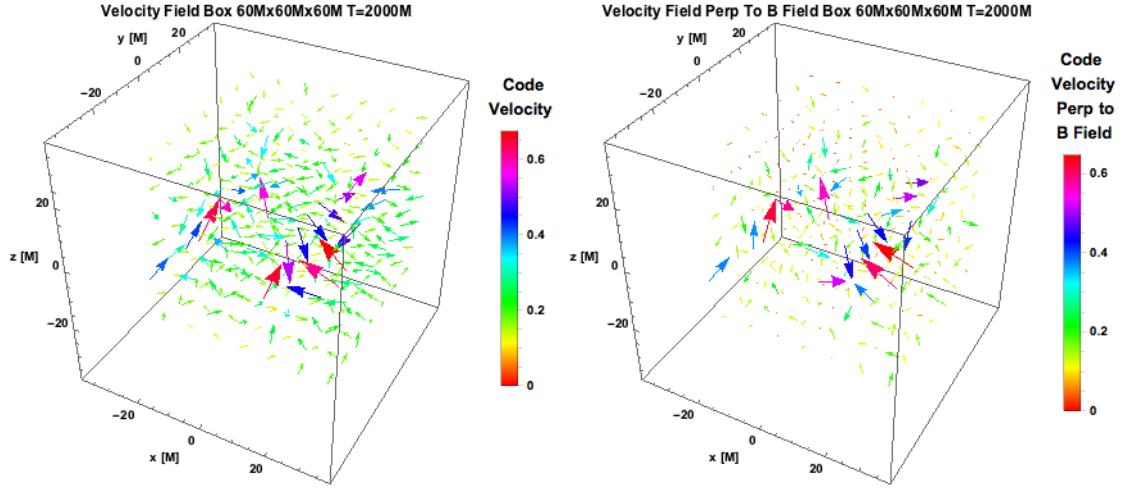


Figure 3.13: Velocity field (left panel) and velocity field component perpendicular to magnetic field (right panel) for a $60M \times 60M \times 60M$ box at the center of the high resolution $80M \times 80M \times 200M$ simulation region for $t_{\text{Gal}} = 2000M$.

To see the dynamical importance of the magnetic field, examine the IDump 3 density plots of B_x , B_y and B_z extending $\pm 100M$ from the equatorial plane in Figure 3.14, and the square and z-component of the derived current density

$$\vec{j}' = \frac{1}{\mu_0} \vec{\nabla} \times \vec{B}' + \epsilon_0 \frac{\partial \vec{E}'}{\partial t} \quad (3.8)$$

in Figures 3.15 and 3.16, respectively (where the current density is approximated as $\vec{j}' \sim \vec{\nabla} \times \vec{B}$).

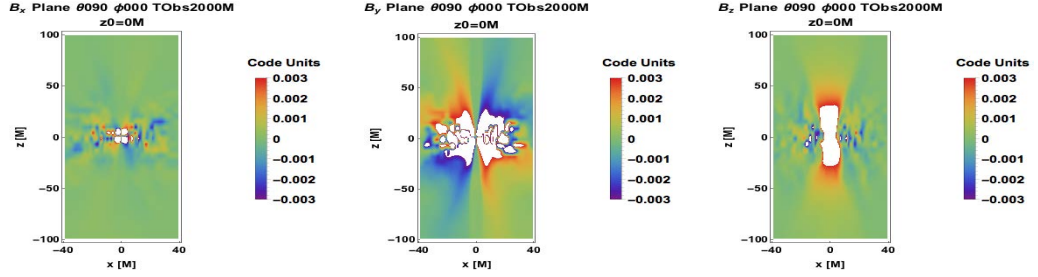
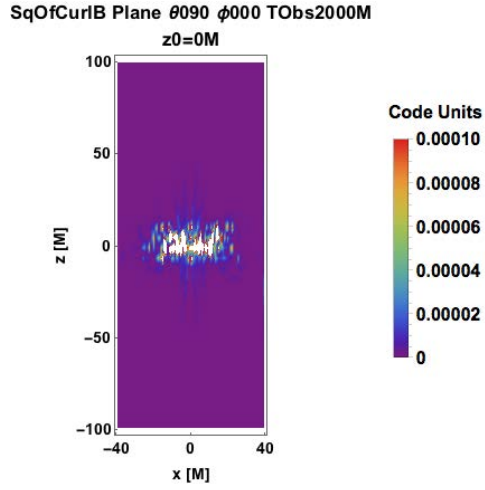


Figure 3.14: Longitudinal (xz -plane) density plots of lab frame magnetic field component (from left to right) B_x , B_y , B_z at simulation time $T = 2000M$. The panels show reversal of the transverse fields across the jet axis.



(3.9)

Figure 3.15: Density plot of the square of the curl of the lab frame magnetic field at simulation time $T = 2000M$. The curl of \vec{B} is proportional to the current density.

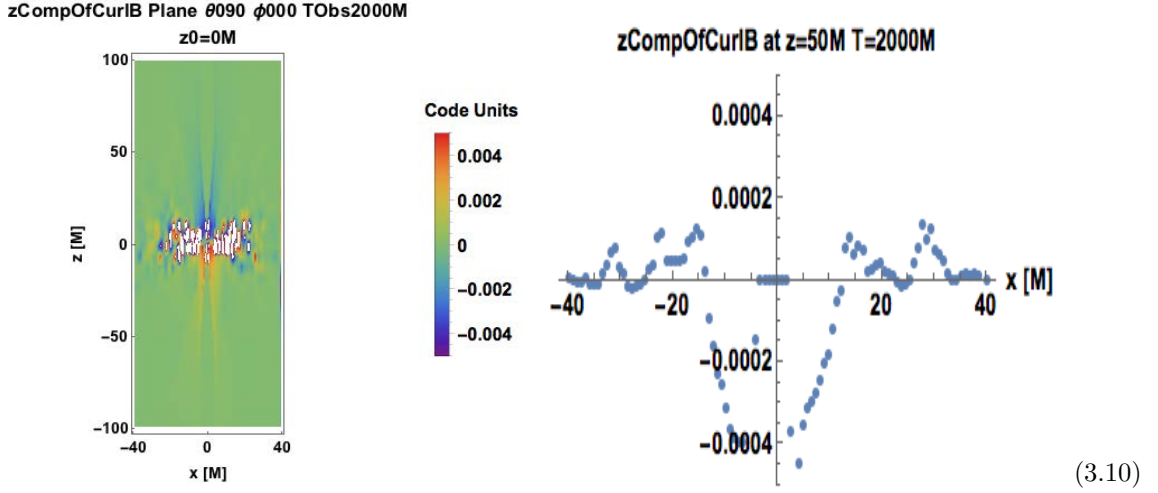


Figure 3.16: Density plot of lab frame magnetic field curl z -component at simulation time $T = 2000M$ (left panel) and a plot of the transverse variation at $z = 50M$ (right panel). This shows the z -component of the current can be large near the center of the jet (outside of a narrow core a few M wide at this altitude).

3.3 Code Coordinates to Physical Units

Quantities calculated from the simulation have scales set by the black hole gravitational radius and some quantity related to energy, e.g., luminosity, while their physical counterparts are expressed by astronomers in cgs units. Thus, we require a scheme for relating black hole quantities calculated from the simulation to quantities observers have measured.

3.3.1 Relating Quantities to the Black Hole for Particle Jet

Here we outline how one can convert units for a jet dominated by particle kinetic energy. The easiest unit conversions are obtained by expressing mass, length, time and frequency in terms of the mass scale M and fundamental constants, cf. Table 3. Units based on other quantities may require more work, cf. 4.

For example, the mass accretion rate can be determined from the code via

$$\dot{M}_{\text{code}} = \int d\Omega \left(\frac{r}{r_g} \right)^2 \rho_{\text{code}} \frac{v_r}{c}$$

Table 3: cgs Unit Conversions Based on $M \equiv M_{\text{M87}} = 6.6 \cdot 10^9 M_\odot$ and Fundamental Constants

Input	Cgs Value
Mass (M)	$1.31 \cdot 10^{43} \text{g}$
Length ($\frac{GM}{c^2}$)	$9.73 \cdot 10^{14} \text{cm}$
Time ($\frac{GM}{c^3}$)	$3.25 \cdot 10^4 \text{s} = 9.0 \text{hr}$
Frequency ($\frac{c^3}{GM}$)	$3.08 \cdot 10^{-5} \text{s}^{-1} = 3.08 \cdot 10^{-14} \text{GHz}$

Table 4: Unit Conversions for Simulation Outputs

Output	$\frac{\text{cgs unit}}{\text{code unit}}$
ρ	$3.797 \cdot 10^{86} \frac{\text{g}^2 \text{s}}{\text{cm}^3} \dot{M}_{\text{code}}^{-1} \dot{M}_{M_\odot/\text{yr}} \dot{M}_{\text{cgs}}^{-2}$
u_g	$8.988 \cdot 10^{20} \frac{\text{cm}^2}{\text{s}^2} \frac{[\rho_{\text{cgs}}]}{[\rho_{\text{code}}]}$
p	$\frac{[u_g \text{ cgs}]}{[u_g \text{ code}]}$

and then related to the observed mass accretion rate by

$$\dot{M}_{\text{phys}} = \dot{M}_{\text{code}} r_g^2 c \left(\frac{\rho_{\text{cgs}}}{\rho_{\text{code}}} \right)$$

(note $r_g^2 c \rho_{\text{cgs}}$ has units of $\frac{\text{g}}{\text{s}}$) to give us the conversion between code and observed rest mass density units, as in Table 4. Furthermore, u_g and p_e have units of $c^2 \rho$.

The luminosity has units of $c^2 \dot{M}$, and can be computed from the simulation by

$$L_e = \int dA F c = \int dA 4\gamma p u c = \int dA 4 \frac{(c^2 + u^2)^{1/2}}{c} p_e u c \quad (3.11)$$

where F is flux and we have normalized $u_\mu u^\mu = \gamma^2 c^2 - u^2 = c^2$. To relate code and physical values of luminosity, we determine the normalization for the power law sources of electrons. Assuming a power law electron distribution $N_\gamma = K \gamma^{-p}$ in the jet, we can determine the normalization K of the electron population size through the pressure $P_e = \frac{1}{3} \int_{\gamma_{\min}}^{\gamma_{\max}} d\gamma N_\gamma \gamma m_e c^2 \implies$

$$K = \frac{3P_e}{m_e c^2 \int_{\gamma_{\min}}^{\gamma_{\max}} d\gamma \gamma^{1-p}} \quad (3.12)$$

where there is a code value for P_e .

We can scale code units for frequency and magnetic field to cgs units by equating other black hole quantities of astronomical systems to those in the simulation.

Table 5: Convenient Conversions for Simulation Inputs

Input	cgs Value
$\nu_{\text{Obs}}(\text{GHz})$	10^9s^{-1}
$\frac{dM_{\text{M87}}}{dt}(M_{\odot}/\text{yr})$	$6.302 * 10^{22} \frac{\text{g}}{\text{s}} = 10^{-3} M_{\odot}/\text{yr}$
$r_{G,\text{M87}}$	$1.99 * 10^{15} \text{cm}$
c	$2.998 * 10^{10} \frac{\text{cm}}{\text{s}}$
GM_{M87}	$8.74 * 10^{35} \text{cm}^3 \text{s}^{-2}$

3.3.2 Relating Quantities to the Black Hole for Electromagnetic Jet

The electromagnetically dominated jet simulation used in this work is more naturally expressed in terms of two implicit scales: the gravitational radius M and the jet magnetic flux Φ threading the hole and the accretion gap. (The dimensionless spin, $a/M = 0.92$, is set by the simulation.) For example, in our application to M87, our unit of magnetic flux is $\sim 10^{26} \text{ Wb} \equiv 10^{34} \text{ G cm}^2 = 10^{34} \text{ Mx}$ so that $\Phi = 10^{26} \Phi_{26} \text{ Wb}$ and $\Phi_{26} \approx 0.5$. All other quantities, including observables, will be expressed in terms of these two scaled quantities. Using a self-similar, stationary axisymmetric model, these ideas will be made concrete in Ch. 4.

Table 6: Convenient Conversions for EM Jet Simulation Inputs

Input	Relation to Black Hole	cgs Value	mks value
Mass	M_{BH}	$1.3 \cdot 10^{43} \text{ g}$	$1.3 \cdot 10^{40} \text{ kg}$
Length	$\frac{GM_{BH}}{c^2}$	$r_{15} \cdot 10^{15} \text{ cm}, r_{15} \sim 1$	$r_{13} \cdot 10^{13} \text{ m}, r_{13} \sim 1$
Time	$\frac{GM_{BH}}{c^3}$	$r_{15} \cdot 3.3 \cdot 10^4 \text{ s}$	$r_{13} \cdot 3.3 \cdot 10^4 \text{ s}$
Magnetic Flux	Φ_B	$\Phi_{34} \cdot 10^{34} \text{ Mx}, \Phi_{34} \sim 1$	$\Phi_{26} \cdot 10^{26} \text{ Wb}, \Phi_{26} \sim 1$
Magnetic Field	$\frac{\Phi_B}{(\text{Length Unit})^2}$	$\Phi_{34}/r_{15}^2 \cdot 10^4$	$\Phi_{26}/r_{13}^2 \text{ T}$
Pressure	$\frac{\Phi_B}{(\text{Length Unit})^4}$	$(\Phi_{34}/r_{15}^2)^2 \cdot 10 \text{Ba}$	$(\Phi_{26}/r_{13}^2)^2 \text{Pa}$

3.4 Inner vs. Outer Jet Simulations

The "Observing Jet Simulations" routines can be adapted to study all parts of AGN. Using the parameter

$$\sigma = \frac{\text{Electromagnetic Flux Density}}{\text{Particle Flux Density}} \quad (3.13)$$

, we can classify regions with $\sigma \gg 1$ as electromagnetically dominated and regions with $\sigma \ll 1$ as dominated by particle kinetic energy. High σ simulations, which include disk and near jet regions, have numerically reliable \vec{E} , \vec{B} and $\vec{E} \times \vec{B}$; low σ simulations include outer jet regions, and have reliable relativistic gas energy density u_g .

Chapter 4

Self-Similar Stationary Axisymmetric Model

To facilitate back-of-the-envelope predictions of jet behavior that do not require extensive analysis of the simulation, it is useful to find analytic forms for important jet variables. To this end, let us start with a model that is stationary ($\frac{\partial}{\partial t} = 0$) and axisymmetric ($\frac{\partial}{\partial \phi} = 0$). In practice, these regimes can be applied to the simulation when they are tied to criteria such as the final time at which transients occur or the range of azimuthal angles over which the appearance of an intensity map appears constant. Proceeding in code units, we also assume we are in the force free regime

$$\rho \vec{E} + \vec{j} \times \vec{B} = \vec{0} \quad (4.1)$$

and that the jet is parabolic, with self-similarity variable $\xi = \frac{s^2}{z}$. Now, we can express– in cylindrical coordinates– the magnetic flux $\Phi = \Phi(\xi(s, z))$, current $I = I(\xi(s, z))$ and fieldline angular velocity $\vec{\Omega}_B(\xi(s, z))$, and relate jet variables to these

$$\begin{pmatrix} B_s \\ B_\phi \\ B_z \end{pmatrix} = \begin{pmatrix} -\frac{1}{2\pi s} \frac{\partial \Phi}{\partial z} \\ \frac{I}{2\pi s} \\ \frac{1}{2\pi s} \frac{\partial \Phi}{\partial s} \end{pmatrix} = \begin{pmatrix} \frac{s\Phi'}{2\pi z^2} \\ \frac{I}{2\pi s} \\ \frac{\Phi'}{2\pi z} \end{pmatrix} \quad (4.2)$$

$$\begin{pmatrix} j_s \\ j_\phi \\ j_z \end{pmatrix} = \vec{\nabla} \times \vec{B} = \begin{pmatrix} -\frac{sI'}{2\pi z^2} \\ -\frac{s(2z\Phi' + (s^2 + 4z^2)\Phi'')}{2\pi z^4} \\ \frac{I'}{\pi z} \end{pmatrix} \quad (4.3)$$

$$\rho = \vec{\nabla} \cdot \vec{E} = -\frac{1}{2\pi z^2} (\xi(4z + \xi)\Phi'\Omega'_B + \Omega_B(2(2z + \xi)\Phi' + \xi(4z + \xi)\Phi'')) \quad (4.4)$$

Enlisting Mathematica, we expand the s - and z -components of the Lorentz force

$$0 = \frac{-2\xi\Phi'^2 - \xi^2\Phi'\Phi''}{2\pi^2 s z^3} + \frac{2\xi^2\Omega_B^2\Phi'^2 - \xi^3\Omega_B\Phi'^2\Omega'_B - 4\xi\Phi'\Phi'' + \xi^3\Omega_B^2\Phi'\Phi''}{2\pi^2 s z^2} + \frac{-I'I + 4\xi\Omega_B^2\Phi'^2 + 4\xi^2\Omega_B\Phi'^2\Omega'_B + 4\xi^2\Omega_B^2\Phi'\Phi''}{2\pi^2 s z} + \mathcal{O}(z)^5 \quad (4.5)$$

$$0 = \frac{s^4\Phi'\Phi''}{4\pi^2 z^6} + \frac{\xi\Phi'^2}{2\pi^2 z^4} + \frac{-2\xi^2\Omega_B^2\Phi'^2 - \xi^3\Omega_B\Phi'^2\Omega'_B + 4\xi\Phi'\Phi'' - \xi^3\Omega_B^2\Phi'\Phi''}{4\pi^2 z^3} + \frac{I'I - 4\xi\Omega_B^2\Phi'^2 - 4\xi^2\Omega_B\Phi'^2\Omega'_B - 4\xi^2\Omega_B^2\Phi'\Phi''}{2\pi^2 s z} + \mathcal{O}(z)^5. \quad (4.6)$$

Taking the leading order terms in z/ξ , which here are the coefficients of the highest power of Z , we have the following equation for I

$$4\xi^2\omega_B^2\Phi'\Phi'' + 4\xi(\Omega_B^2 + \xi\Omega_B\Omega'_B)\Phi'^2 = I'I \quad (4.7)$$

whose solution gives us the first analytic form

$$I = -2\Omega_B\xi\Phi' \quad (4.8)$$

To convert this code current to SI units, use the impedance of free space $Z_0 = \mu_0 c = 377\Omega$ and write $I = -2\frac{\Omega_B\xi\Phi'}{Z_0}$. In addition to Ω , Φ and I , another quantity conserved on surfaces of constant ξ is

$$V = \int \frac{\Omega d\Phi}{2\pi} \quad (4.9)$$

4.1 Reference Case: $z=50M$

In addition to I, Φ, Ω_B , quantities \vec{B} , V , \vec{E} , Poynting flux $\vec{F}_{EM} = \frac{1}{\mu_0}\vec{E} \times \vec{B}$ and the dynamic quantities $L_{EM} = 2\pi \int ds F_{EM} s$ and $G_{EM} = \frac{F_{EM}}{\Omega_B}$ can be derived in the self-similar semi-analytic model. The self-similarity parameter is determined by a rough fit to the curvature of parabolic jets from the simulation, e.g., a jet width of $32M$ at $z_0 = 50M$ implies $\xi = 20$. Considering the simulation at $z = 50M$, use the fitting forms

$$\begin{aligned} \Phi &= \Phi_H \tanh(0.3\xi) \\ \Omega_B &= \frac{2c}{r_H} 0.5 \frac{1+\xi}{1+2\xi} \end{aligned} \quad (4.10)$$

where the scales $\Phi_H = 10^{26}\text{Wb}$ and $r_H = 2 \cdot 10^{13}\text{m}$ for M87. From this can be derived

$$I = -\frac{2\Omega_B\xi\Phi'}{Z_0} = -\frac{0.0477465s^2 \left(1 + \frac{s^2}{50}\right) \text{sech}[0.006s^2]^2}{1 + \frac{s^2}{25}} \cdot 10^{18} \text{A} \quad (4.11)$$

The results for altitude $z_0 = 50M$ are shown in Figures, 4.1, 4.2 and 4.3. In Figure 4.1, where $B_z = \frac{\xi}{\pi s^2} \frac{d\Phi}{d\xi}$, $B_\phi = \frac{I}{2\pi s}$ and $B_s = \frac{\xi}{2\pi s z}$, we see the flux is confined by the toroidal field and the

denser medium surrounding the jet. The field becomes increasingly toroidal ($B_z \sim s^{-2} \sim z^{-1}$, $B_\phi \sim s^{-1} \sim z^{-1/2}$) toroidal field goes to 0 outside the jet boundary, indicating a jet return current also confined to the jet. Regarding the electric field, one notes that its values are not unlike typical values for the klystron at SLAC. However, Figure 4.2 indicates that that V , found by integrating E_s , is otherworldly (the jet is much larger than SLAC). The fieldline angular speed at the jet boundary diminishes to about half the value at the axis. From Figure 4.3, the radiation flux of the jet peaks at intermediate cylindrical radius. Also, we see $L_{\text{EM}} \sim \frac{V^2}{Z_0}$ (the impedance of free space matches the impedance of the hole).

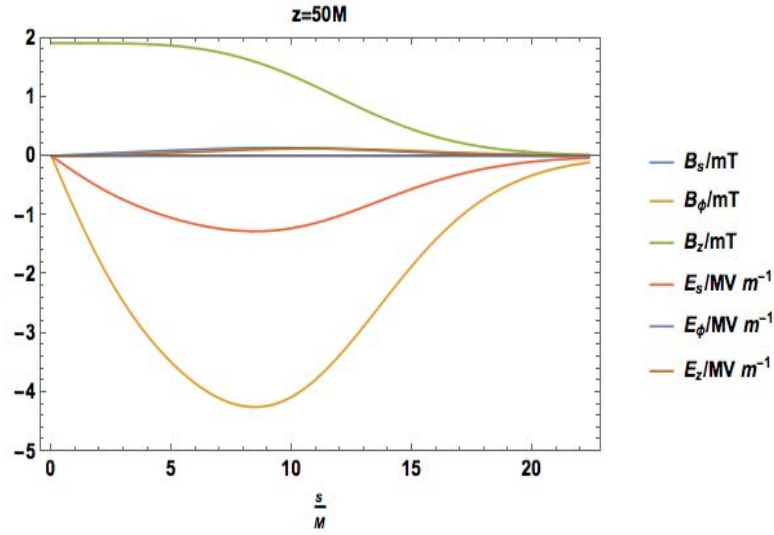


Figure 4.1: Electric and magnetic field components at $z_0 = 50M$ as a function of cylindrical radius.

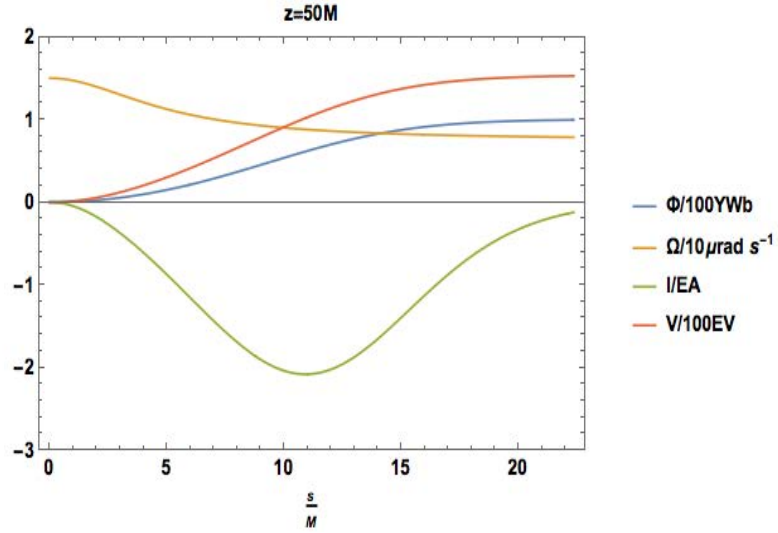


Figure 4.2: Magnetic flux, fieldline angular speed, current and voltage at $z_0 = 50M$ as a function of cylindrical radius.

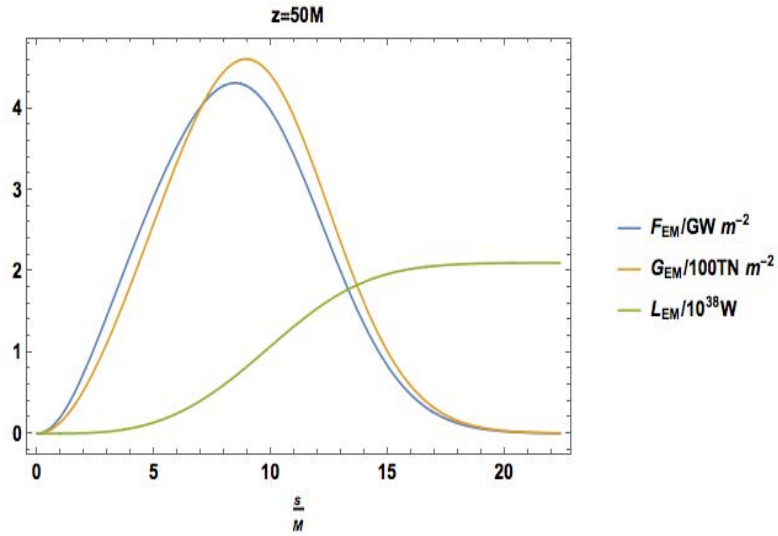


Figure 4.3: Poynting flux strength, Poynting flux strength per fieldline angular speed and electromagnetic luminosity at $z_0 = 50M$ as a function of cylindrical radius.

The upshot of our self-similar model is that it is readily scaled to other altitudes and can be used for testing the code and unit conversions.

4.2 Near the Hole: $z=10M$ - $100M$

The magnetic field structure in Figure 4.4 is compatible our finding in the simulation that the jet is becoming collimated so that the tangent to the flow becomes steeper with higher z . However, we also see that the jet is not focused, but expanding. The toroidal field is largest at intermediate radius.

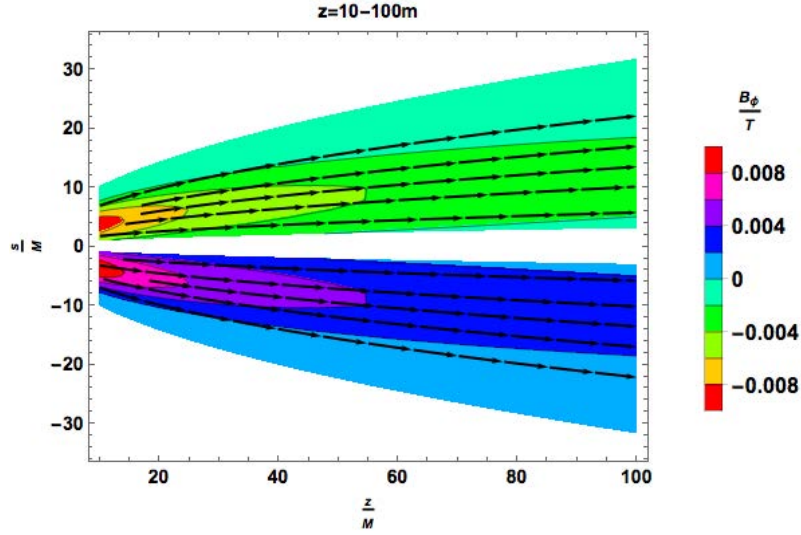


Figure 4.4: Jet magnetic field between $z = 10M$ and $z = 100M$.

4.3 Outer Jet: Beyond $100M$

On this scale, the model captures confinement by the toroidal field and external environment 4.5. On larger scales in 4.5, the vertical magnetic field is confined to a narrow core at small cylindrical radius.

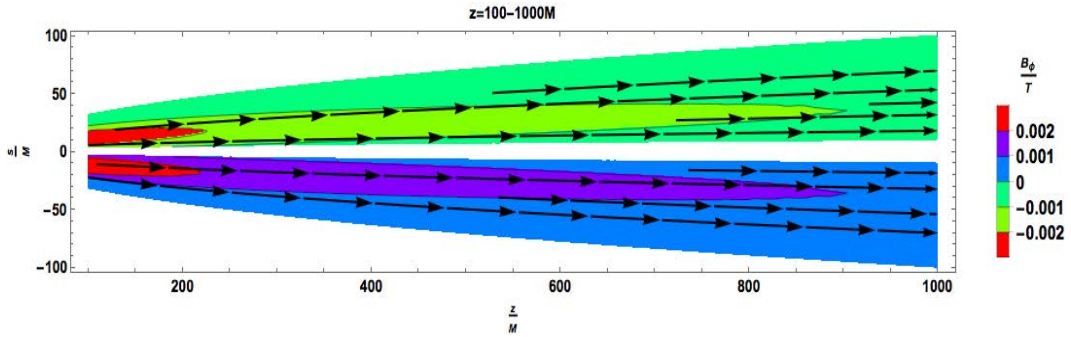
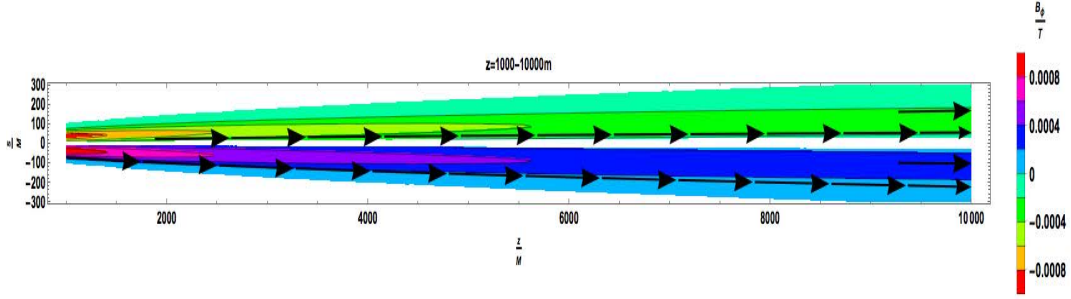


Figure 4.5: Jet magnetic field between $z = 100M$ and $z = 1000M$.

Figure 4.6: Jet magnetic field between $z = 1000M$ and $z = 10000M$.

4.3.1 Velocity Field: Bead on a Wire

The velocity field in the self-similar model was fit to the simulation. However, it is very close to the field that would be found for the case of vanishing Lorentz force on simulation particles. For high σ regions in the inner few hundred M from the black hole, the simulation is approximately force free, and we may assume that the velocity is that of a test particle released at $z_0(\xi)$ and being accelerated centrifugally along the field like a bead on a magnetic wire with parabolic constant ξ . Ignore pressure and non-ideal electromagnetic stress as well as inertial influence on the field geometry. If we non-relativistically transform into a frame rotating with angular velocity Ω where the electric field vanishes, the particle travels with velocity \vec{v}' along \vec{B} and $s\Omega \ll c$. The centrifugal potential in the simple, tractable case of subrelativistic, sub-Alfvénic motion is

$$\frac{1}{2}\Omega^2 s^2, \quad (4.12)$$

so $v'^2 = \Omega^2 s^2 - \text{Const.}$ and $\vec{v} = \kappa \vec{B} + \vec{\Omega} \times \vec{r} = \vec{v}' + \vec{\Omega} \times \vec{r}$. Hence

$$\vec{v} = \left[\Omega^2 (s^2 - s_{\text{ref}}^2) + v_{\text{ref}}'^2 \right]^{1/2} \hat{B} + s\Omega \hat{\phi} = (\hat{B} + \hat{\phi})s\Omega \quad (4.13)$$

for $z \gg z_{\text{ref}}$ where $\Omega = \Omega(\xi)$, $s_{\text{ref}} = (\xi z_{\text{ref}})^{1/2}$ and $v_{\text{ref}}' = v'(\xi, z_{\text{ref}})$.

4.4 Observing Self-Similar Model

Let us adopt M87 parameters $d = 5.1 \cdot 10^{23}$ m (so $1 M = 0.004$ mas), $a/M = 0.92$ so $\Omega_H = 10^{-5}$ and $\Phi_{H26} = 1$. Assuming the gas pressure is a constant fraction ($7 \cdot 10^{-7}$) of the magnetic pressure (refer to β model of Chapter 5), we have a synchrotron emission and absorption prescription that can be observed. Performing ray tracing on the model at $\theta_{\text{obs}} = 20^\circ$ gives the intensity and polarization of the inner mas in Figure 4.7 and inner 10 mas in Figure 4.8.

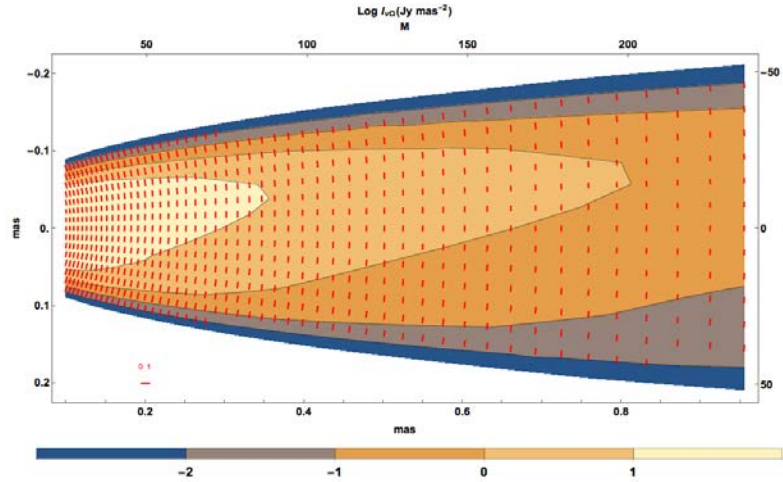


Figure 4.7: Intensity (colors) and E-field indicating polarization (red lines) between 0 mas and 1 mas at 43 GHz and viewing angle 20° . The map lacks bilateral symmetry, as the observed intensity depends on a relative angle between observer and magnetic field that is different on the two sides of the jet.

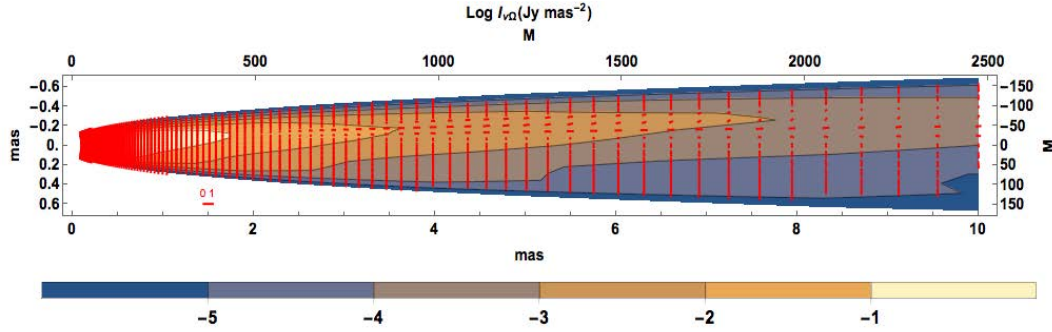


Figure 4.8: Intensity (colors) and E-field indicating polarization (red lines) between 0 mas and 10 mas. The core (inner mas) has the greatest polarization. Limb brightening of the distribution of E-field is only apparent in the outer few mas.

The polarization fraction

$$P = \frac{\sqrt{Q^2 + U^2}}{I} \quad (4.14)$$

can be decomposed according to the X - and Y -coordinate axes in Chapter 2 by

$$\langle P_X, P_Y \rangle = \left\langle \sqrt{\frac{Q^2 + U^2 + Q(Q^2 + U^2)}{2I^2}}, \sqrt{\frac{Q^2 + U^2 - Q(Q^2 + U^2)}{2I^2}} \text{sign}(U) \right\rangle \quad (4.15)$$

The asymmetry of intensity in this model is quite pronounced while the polarization is fairly homogeneous. One may also take a convolution

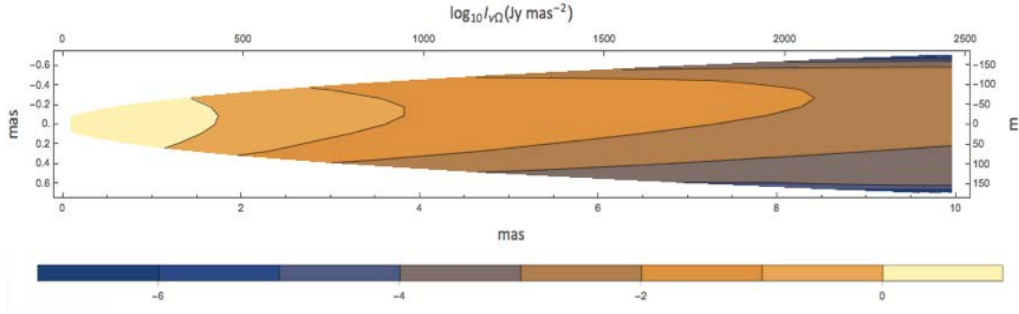


Figure 4.9: Intensity between 0 mas and 10 mas convolved with a Gaussian of width $(\sigma_X, \sigma_Y) = \frac{1}{\sqrt{8\pi \ln 2}}(0.43, 0.21)$ mas (in anticipation of EHT observations).

as in Figure 4.9 to emulate observing instrument properties. The convolution clearly smears out the intensity isocontours. We will see in Chapter 7 how the prescription used in this model compares to M87 observations.

Chapter 5

Emission, Particle Acceleration and Dissipation

In practice, when confronted with explaining observations of hard-to-resolve, distant jets in AGN teeming with wind and molecular clouds, we often face an embarrassment of riches. Nearly unconstrained jet compositions and emission regions leave us with a panoply of possible explanations. The degeneracy is not simply a function of theoretical ignorance or observational ineptitude, as the task of replicating jet observations across the electromagnetic spectrum is barely imaginable with a single emissivity prescription. The “observing jet simulations” routines allow one to analyze the same source in the low-, intermediate- and high-frequency regimes, and in specific simulation segments, allowing us to broadly categorize AGN jets in terms of a few simple limits.

The key insight is that we relate the emissivity and absorption coefficient to the partial pressure \tilde{P}_e of the due to the source particles emitting at the observed frequency. The prescription does not vary much for reasonable values of the power law index $1 < p < 3$, as the plots in Chapter 2 show the p-dependent parts change only by a number of order unity. Also key, the emission observed will be written in terms of the “effective” magnetic field B_e , which in turn depends not only on the strength of the magnetic field, but also on the angle the magnetic field makes with the viewing angle. The prescription incorporates variation with gamma through \tilde{P}_e .

5.1 Synchrotron Emissivity Prescriptions

From the exposition of the theory of synchrotron radiation in Chapter 2,

$$j_\nu \propto K B^{1+\alpha} \nu^{-\alpha} \propto P_g B^{1+\alpha} \nu^{-\alpha} \propto u_g B^{1+\alpha} \nu^{-\alpha} \quad (5.1)$$

is a good toy model to account for the radio emissivity of AGN jets because $(P_\nu)_{\text{power law}} \propto B^{1+\alpha} \nu^{-\alpha}$ and the pressure dependent function K . Jets with this prescription should appear dominated by emission from the interior (spine) for higher α based on the investigation of Chapter 3 showing the jet magnetic field concentrated there. We now specify models by relating the pressure-dependent part of this prescription to \tilde{P}_e , physically motivated by energy arguments dissipation mechanisms.

5.1.1 Beta Model

The simplest idea is that $\beta_e \equiv \tilde{P}_e/P'_B$ (where $P'_B = b'^2/2\mu_0$) is constant, generalizing the common assumption of equipartition. This assumption is shown to be reasonable inside the jet, as seen in Figure 5.1.

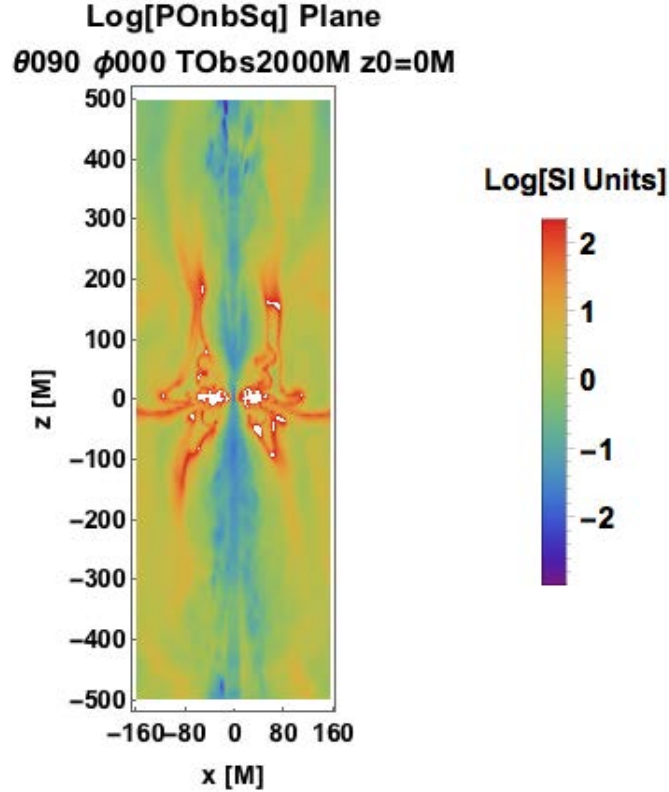


Figure 5.1: Simulation gas to magnetic pressure ratio longitudinal profile at $T = 2000M$.

5.1.2 Bias Model: Scaling Gas Pressure to Powers of Magnetic Field

Inner jet simulations are often met by the requirement to artificially set a floor to prevent the code density ρ and gas internal energy density u_g inside the jet funnel from approaching 0. This reduces our confidence in using these densities in particle emission prescriptions. A more

sound approach is to scale particle energy density u_g to magnetic energy density $b_\mu b^\mu$ using the assumption of equipartition of energy

$$u_g \sim b_\mu b^\mu \quad (5.2)$$

To account for varying degrees of gas pressure relative to magnetic pressure dominance, it is natural to make the scaling

$$u_g \sim (b_\mu b^\mu)^n \quad (5.3)$$

Before implementing the bias model in the simulation, it is difficult to ascertain which value of n will result in the greatest overall intensity. For low n , the gas pressure remains high far along the jet. For high n , emitting particles are better able to escape.

5.2 Synchrotron Particle Acceleration Prescriptions with Dissipation

The following formalism for specifying the spectral pressure can be cast as finding appropriate functions for the dissipation rate W' in

$$\tilde{P}_e = W' t' \quad (5.4)$$

The strategy for developing these models is to relate dissipation to quantities such as shear stress τ , shear strain S and current density j^α that affect the number of radiating particles. A simple estimate for velocity shear is the dominant component $|\frac{dv_z}{ds}|$ of the shear tensor. Objects lit up by velocity shear should appear brightest on the outer portion (sheath). Other prescriptions are expected to be lit up most where their particle acceleration is greatest, e.g. near the center (spine) for current density models.

5.2.1 Alpha Model

This model is inspired by the famous α -prescription [52] commonly invoked in the study of accretion disks where the shear stress is supposed to be αP where P is the pressure which we take here to be $(P'_M + P'_g) = \tau'/\alpha$. This is not naturally covariant and in the spirit of disk models, we simply multiply this stress by an estimate of the comoving rate of shear $S' = \gamma^2 |dv_z/ds|$ so that the comoving dissipation rate is $W' = \frac{1}{2} \tau' S'$. There are two sources of electron cooling, expansion, with a timescale $t'_{\text{exp}} = \gamma^{-1} |\nabla \cdot (\gamma \mathbf{v})|^{-1}$ and radiative cooling $t'_{\text{rad}} = (\mu_0 c / \sigma_T \mathcal{D}) (3em_e / 2\pi \nu B_e^3)^{1/2}$. We then estimate the electron partial pressure by $\tilde{P}_e = W' \min[t'_{\text{exp}}, t'_{\text{rad}}]$. Putting it all together

$$\tilde{P}_{e, \alpha \text{ model}} = \frac{1}{2} \alpha \left(\frac{b_\mu b^\mu}{2\mu_0} + \frac{u_g}{3} \right) \left(\gamma^2 \left| \frac{dv_z}{ds} \right| \right) \min \left\{ \frac{1}{\gamma |\gamma \vec{\nabla} \cdot \vec{v} + \vec{v} \cdot \vec{\nabla} \gamma|}, \frac{\mu_0 c}{\sigma_T} \sqrt{\frac{3em_e}{2\pi}} \mathcal{D}^{-1} B_e^{-2/3} \nu^{-1/2} \right\} \quad (5.5)$$

To implement the α model in the code, it is helpful to write

$$\begin{aligned} \frac{dv_z}{ds} &= \frac{\partial v_z}{\partial x} \frac{\partial x}{\partial s} + \frac{\partial v_z}{\partial y} \frac{\partial y}{\partial s} = \text{sign}(x) \frac{s}{\sqrt{s^2 - y^2}} \frac{\partial v_z}{\partial x} + \text{sign}(y) \frac{s}{\sqrt{s^2 - x^2}} \frac{\partial v_z}{\partial y} \\ &= \frac{x}{\sqrt{x^2}} \frac{s}{\sqrt{y^2}} \frac{\partial v_z}{\partial x} + \frac{y}{\sqrt{y^2}} \frac{s}{\sqrt{x^2}} \frac{\partial v_z}{\partial y} \end{aligned} \quad (5.6)$$

(or

$$\left(\frac{dv_z}{ds} \right)^2 = \left(\frac{dv_z}{dx} \right)^2 + \left(\frac{dv_z}{dy} \right)^2 \quad (5.7)$$

to avoid dividing by 0 at the axes) and

$$\vec{\nabla} \gamma = \begin{pmatrix} \frac{\partial}{\partial x} \\ \frac{\partial}{\partial y} \\ \frac{\partial}{\partial z} \end{pmatrix} \left(1 - \frac{v^2}{c^2} \right)^{-\frac{1}{2}} = \frac{1}{c^2} \gamma^3 v \begin{pmatrix} \frac{\partial v}{\partial x} \\ \frac{\partial v}{\partial y} \\ \frac{\partial v}{\partial z} \end{pmatrix} \quad (5.8)$$

$$\Rightarrow t'_{\text{exp}} = \frac{1}{\gamma |\gamma \vec{\nabla} \cdot \vec{v} + \vec{v} \cdot \vec{\nabla} \gamma|} = \frac{1}{\gamma |\gamma \left(\frac{\partial v}{\partial x} + \frac{\partial v}{\partial y} + \frac{\partial v}{\partial z} \right) + \frac{\gamma^3 v}{c^2} \left(v_x \frac{\partial v}{\partial x} + v_y \frac{\partial v}{\partial y} + v_z \frac{\partial v}{\partial z} \right)|} \quad (5.9)$$

so that spatial derivatives can easily be computed using

$$\frac{\partial v}{\partial x} \sim \frac{v \begin{pmatrix} x + x\text{Step} \\ y \\ z \end{pmatrix} - v \begin{pmatrix} x \\ y \\ z \end{pmatrix}}{x\text{Step}}, \quad \frac{\partial v}{\partial y} \sim \frac{v \begin{pmatrix} x \\ y + y\text{Step} \\ z \end{pmatrix} - v \begin{pmatrix} x \\ y \\ z \end{pmatrix}}{y\text{Step}}, \quad \frac{\partial v}{\partial z} \sim \frac{v \begin{pmatrix} x \\ y \\ z + z\text{Step} \end{pmatrix} - v \begin{pmatrix} x \\ y \\ z \end{pmatrix}}{z\text{Step}} \quad (5.10)$$

A density plot of this partial pressure is given in Figure 5.2.

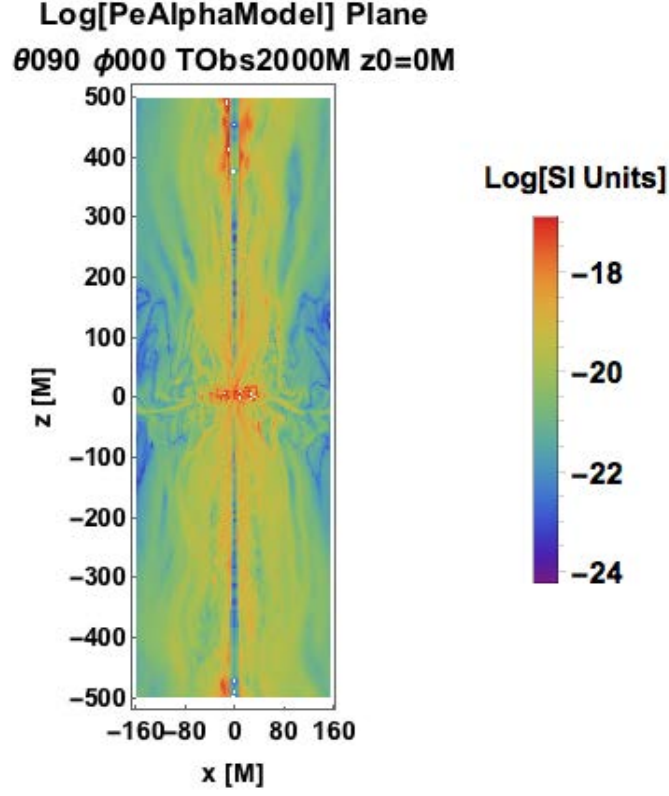


Figure 5.2: Spectral pressure longitudinal profile at $T = 2000M$ for alpha model with $\alpha = 0.5$.

5.2.2 Velocity Gradient Model

The velocity gradient model, which we shall term S^2 -model for reasons that will soon be apparent, is based explicitly on Newtonian viscosity. We introduce a characteristic length L and define a kinematic viscosity by $\nu' = cL/3$. The dynamic viscosity is

$$\mu' = c \frac{L}{3} \sqrt{\left(\rho c^2 + \frac{b_\mu b^\mu}{2\mu_0} \right) \left(\frac{u_g}{3} + \frac{b_\mu b^\mu}{2\mu_0} \right)} \quad (5.11)$$

The shear strain is $\tau' = \mu' S'$. The dissipation rate is then $W' = \frac{1}{2} S' \tau' = \frac{1}{2} \mu' S'^2$ and \tilde{P}_e is estimated as above. A density plot of this partial pressure is given in Figure 5.3.

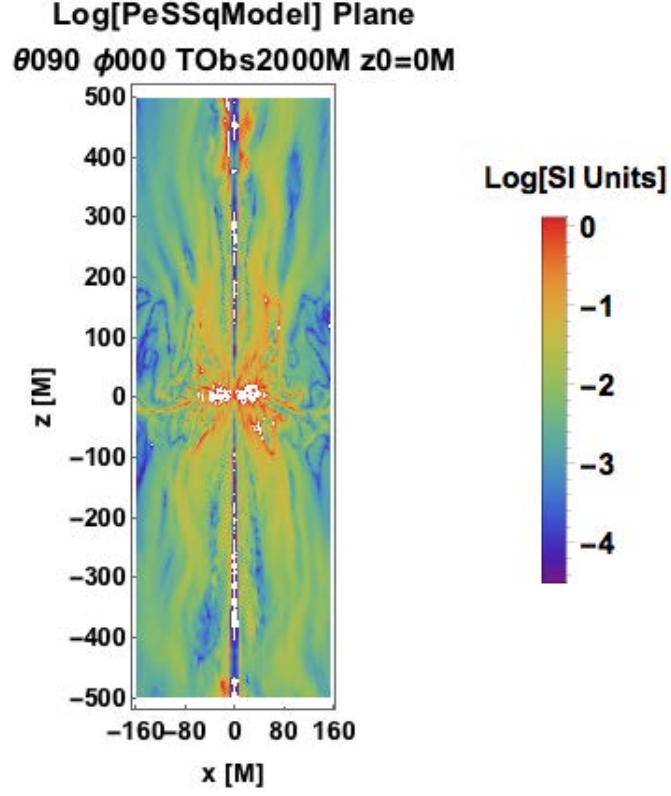


Figure 5.3: Spectral pressure longitudinal profile at $T = 2000M$ for velocity gradient model with $L = 1$.

5.2.3 Current Density Model

Finally, we work directly with the electromagnetic variables and replace the velocity gradient by the field gradient or equivalently the current density. In this case, which is best motivated by particle-in-cell (PIC) simulations of relativistic reconnection we propose $W' = \mu_0 c L |j_\alpha j^\alpha|$. The partial pressure from this j^2 -model is depicted in Figure 5.4.

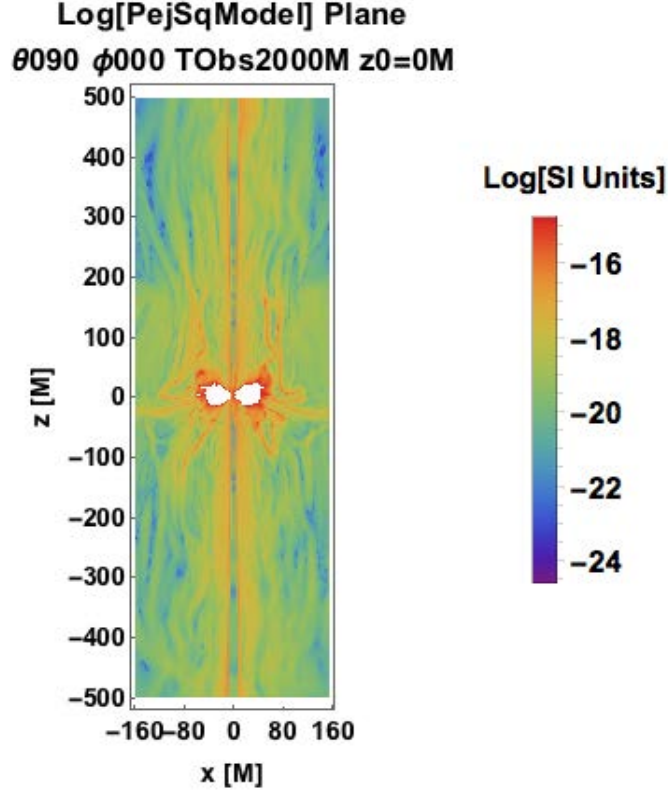


Figure 5.4: Spectral pressure longitudinal profile at $T = 2000M$ for current density model with $L = 1$.

5.2.4 Synchrotron Prescription in Convenient Observational Units

Anticipating application to M87, it is useful to write the comoving frame Lorentz factor of the particles "observed" to be emitting the radiation, $\tilde{\gamma}' = 20\nu'_{10}{}^{1/2}|\vec{B}'_{-3} \times \hat{n}'|^{-1/2}$, the lab frame magnetic field \vec{B}_{-3} measured in mT and ν'_{10} measured in units of 10 GHz. We assume that $K'_{\Omega'}$ and the pressure are isotropic but it is straightforward to generalize to the anisotropic case which may naturally arise in these jets. The total electron-positron pressure is $P_e = \int d\ln \gamma' \tilde{P}_e$. There may be additional pressure contributions from relativistic ions and non-relativistic plasma.

The emission, $j'_{\nu', \Omega'}(\nu', \hat{n}')$, and absorption, $\chi'(\nu', \hat{n}')$, coefficients are most naturally expressed in the comoving (primed) frame where there is no electric field. Standard synchrotron radiation theory (e.g. [33]) gives expressions for polarizations parallel, \parallel , and perpendicular, \perp , to the projected

comoving magnetic field \vec{B}' and $p = \{1, 1.5, 2, 2.5, 3\}$:

$$j'_{\nu'\Omega'} = j'_{\nu'\Omega',||} + j'_{\nu'\Omega',\perp} = K'_{\Omega'} |\vec{B}'_{-3} \times \hat{n}'|^{\frac{1+p}{2}} \nu'^{\frac{1-p}{2}}_{10} \times$$

$$2.4 \cdot 10^{-30} \frac{\text{W}}{\text{Hz m}^3 \text{sr}} \times \begin{cases} 50.4 + 202 = 252.4, & p = 1 \\ 6.15 + 29.2 = 35.35, & p = 1.5 \\ 1 + 5.5 = 6.5, & p = 2 \\ 0.191 + 1.19 = 1.381, & p = 2.5 \\ 0.041 + 0.285 = 0.326, & p = 3 \end{cases} \quad (5.12)$$

and

$$\chi'_{\nu'} = \frac{1}{2} \left(\chi'_{\nu'\Omega',||} + \chi'_{\nu'\Omega',\perp} \right) = K'_{\Omega'} |\vec{B}'_{-3} \times \hat{n}'|^{\frac{2+p}{2}} \nu'^{-\frac{4+p}{2}}_{10} \text{hspace1cm}$$

$$\times 2.58 \times 10^{-19} \text{m}^{-1} \times \begin{cases} 1.69 + 9.27 = 10.96, & p = 1 \\ 1.24 + 7.76 = 9.00, & p = 1.5 \\ 1.0 + 7.00 = 8.0, & p = 2 \\ 0.860 + 6.66 = 7.52, & p = 2.5 \\ 0.778 + 6.62 = 7.398, & p = 3 \end{cases} \quad (5.13)$$

In order to evaluate these expressions, we must transform the magnetic field \vec{B} and the ray direction \hat{n} from the simulation frame to the comoving frame (cf. Chapter 2). We must also transform the source function and absorption coefficient from the comoving to the simulation frame using

$$j_{\nu,\Omega}(\nu, \hat{n}) = \mathcal{D}^{\frac{3+p}{2}} j'_{\nu',\Omega'}(\nu, \hat{n}') \quad (5.14)$$

$$\chi(\nu, \hat{n}) = \mathcal{D}^{\frac{2+p}{2}} \chi'(\nu, \hat{n}') \quad (5.15)$$

We also need to transform the polarization. This is most easily done by noting that the electric vector in the \perp polarization mode is along the direction of $\vec{B}' \times \hat{n}'$. This electric vector direction is along $\mathcal{D}[\vec{B}/\gamma + (\vec{B} \cdot \hat{n})\vec{v}] \times \hat{n}$ in the simulation frame. We normalize to give this vector unit length and call it \hat{e}_{\perp} . The parallel polarization direction is $\hat{e}_{\parallel} = \hat{n} \times \hat{e}_{\perp}$.

We use these expressions in the equations of polarized radiative transfer.

5.3 Inverse Compton Prescriptions

Here we devise a simple model for jet gamma ray emission. The exposition of inverse Compton radiation in Chapter 2 suggests an emissivity proportional to the relativistic electron gas pressure

$P_g = (\gamma_{\text{E.o.S}} - 1)u_g$ (a proxy for the electron number density).

$$j_\nu \propto P_g. \quad (5.16)$$

The sites of inverse Compton emission depend on where we place the soft photons. For example, one may consider the local generation of soft photons. It is believed that low power BL Lacs produce soft photons from jet synchrotron radiation via the synchrotron self-Compton process. Powerful blazars reprocess accretion disk radiation. One soft photon source that is relatively easy to model is the broad line region (BLR). One may use a simple geometric model of a cylindrical wall comprised of soft UV photons from the BLR encompassing each jet (neglect pair-produced photons near each pole of the black hole, as upscattering of upstream photons by downstream electrons is negligible in the jet). Note there is less scattering from photons chasing e- than approaching e- from head on.

As before, we can relate simulated flow variables of interest to get important scaling relations. Using the lepton distribution function, $N_\gamma = K\gamma^{-2}$, we may deduce the spectrum of gamma rays

$$N_\gamma \sim \gamma^{-2} \implies I_\nu \sim \nu^{-\frac{1}{2}} \quad (5.17)$$

The spectrum of scattered gamma rays in this scenario is

$$j_{\nu,\Omega} = \frac{1}{4\pi} \int d\gamma N_\gamma 2\gamma^2 \sigma_{TC} \int d\nu' \frac{u_{\nu'}}{\nu'} \delta\left(\nu - \frac{4}{3}\gamma^2\nu'\right) \quad (5.18)$$

Note $\nu - \frac{4}{3}\gamma^2\nu' = 0 \implies \nu' = \frac{3}{4\gamma^2}\nu$ and

$$K = \frac{3P_e}{\ln \frac{\gamma_{\max}}{\gamma_{\min}}} \quad (5.19)$$

In the absence of a convincing observed functional form, we take the soft photon distribution to be constant

$$u_{\nu'} = C \quad (5.20)$$

Then

$$j_{\nu,\Omega} = \frac{1}{2\pi} \int_{\gamma_{\min}}^{\gamma_{\max}} d\gamma N_\gamma \gamma^2 \sigma_{TC} \frac{u_\nu}{\frac{3\nu}{4\gamma^2}} \frac{3}{4\gamma^2} = \frac{\sigma_{TC}}{2\pi} C \int_{\gamma_{\min}}^{\gamma_{\max}} d\gamma N_\gamma \gamma^2 \nu^{-1} \quad (5.21)$$

and, using Equation 5.19,

$$j_{\nu,\Omega} = \frac{\sigma_{TC}}{2\pi} C \int_{\gamma_{\min}}^{\gamma_{\max}} d\gamma K \nu^{-1} = \frac{\sigma_{TC}}{2\pi} C \int_{\gamma_{\min}}^{\gamma_{\max}} \frac{3P_e}{\frac{\gamma_{\min}}{\gamma_{\max}}} (\gamma_{\max} - \gamma_{\min}) \nu^{-1} \quad (5.22)$$

Chapter 6

Radiative Transfer and Imaging Pipeline

Unpolarized radiative transfer is an intuitive concept: Start with a beam of intensity, add some more intensity when passing through sources, remove some intensity at sinks, and then you are left with the final beam. Adding a polarimeter is only slightly more conceptually involved, as one must now account for a rotating polarization ellipse determining the relative contribution of each independent polarization. Translating these ideas into code resulting in image maps, however, requires care, as some approaches are far more computationally efficient than others.

6.1 Solving Radiative Transfer Equation

Without opacity or polarization, the problem of radiative transfer is trivial: $dI_\nu = j_\nu ds$. The solution of the unpolarized radiative transfer equation with opacity

$$\frac{dI_\nu}{ds} = j_\nu - \chi_\nu I \quad (6.1)$$

is

$$I_\nu = I_0 e^{-\tau_\nu} + \int_0^{\tau_\nu} S_\nu e^{-\tau'_\nu} d\tau'_\nu \quad (6.2)$$

where $S_\nu = j_\nu/\chi_\nu$ and $\tau_\nu = \int_{s_i}^{s_f} \chi_\nu ds$. A discretized version of this solution on the simulation lattice reads

$$I_{\nu,f} = I_{\nu,0} e^{\sum_{\vec{s}_n \in \text{l.o.s}} \chi_\nu(\vec{s}_n) s_n} + \sum_{\vec{s}_n \in \text{l.o.s}} j_\nu(\vec{s}_n) e^{-\sum_{\vec{s}_m \in \{s_0, \dots, s_n\}} \chi_\nu(\vec{s}_m) s_m} \|\vec{s}_{n+1} - \vec{s}_n\|. \quad (6.3)$$

An example of an evenly spaced sequence of line of sight (l.o.s.) points is

$$\{\vec{s}_n | n = 0, 1, \dots, N\} = \left\{ \text{Rot}_{\hat{z}}(\phi) \text{Rot}_{\hat{y}}(\theta) \begin{pmatrix} 0 \\ 0 \\ \frac{\text{diam}}{2} - n * \text{Step} \end{pmatrix} | n = 0, 1, \dots, N \right\} \quad (6.4)$$

where $\text{Step} = \frac{\text{diam}}{N}$. One may make the choice to stop the integration from observer plane to source when the optical depth reaches order unity if computational efficiency gained supersedes accuracy lost.

For optically thin, polarized radiative transfer,

$$\begin{aligned} \Delta Q_{\text{Obs}} &= \mathcal{D}(j'_1 - j'_2) \cos(2\psi) \Delta s_i \\ \Delta U_{\text{Obs}} &= \mathcal{D}(j'_1 - j'_2) \sin(2\psi) \Delta s_i \end{aligned} \quad (6.5)$$

where $j'_1 - j'_2 \propto j'_1 + j'_2$ for constant p , so the Stokes' parameters Q and U can be deduced from the total emissivity at each point in the ray tracing.

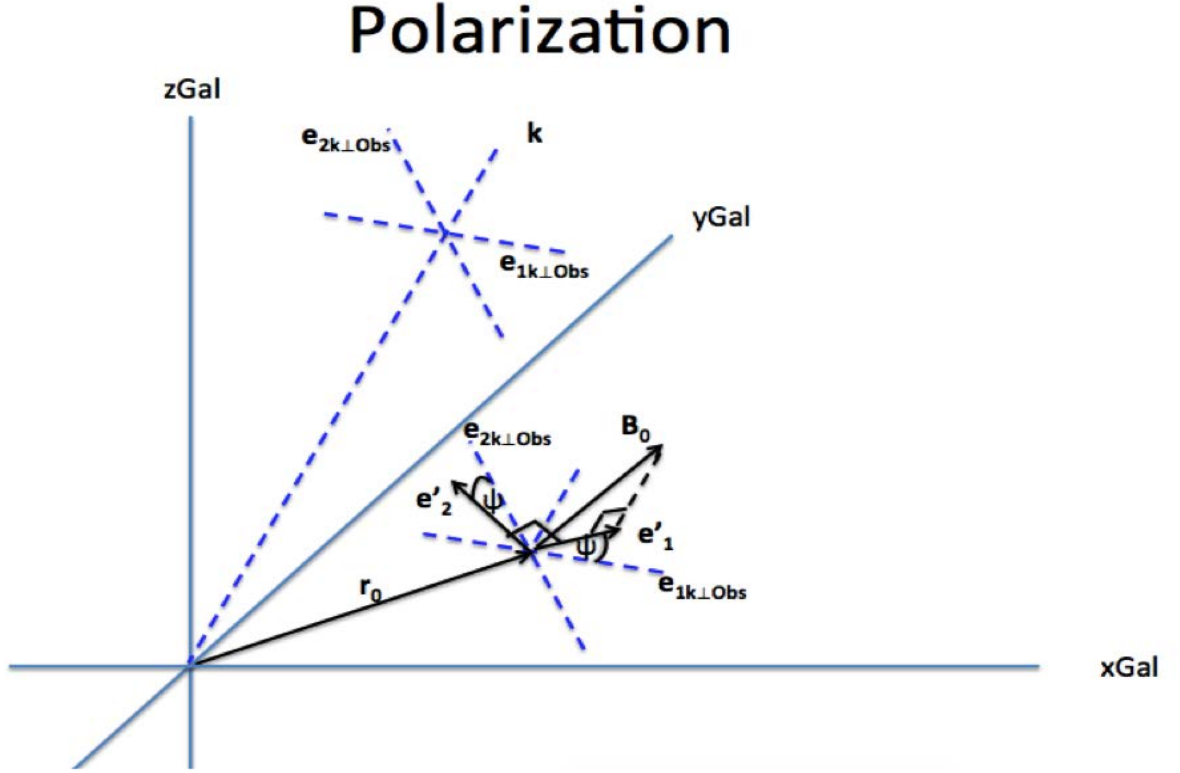


Figure 6.1: Unit vectors $\hat{e}_{1\hat{k}\perp\text{Obs}}$ and $\hat{e}_{2\hat{k}\perp\text{Obs}}$ span the plane perpendicular to the emitter frame observer direction \hat{k} (which transforms to galaxy observer direction \hat{n} upon boosting by emitter velocity \vec{v}). For an electron at source point \vec{r}_0 emitting synchrotron radiation in direction \hat{k} , polarization ellipse axis $\hat{e}_1 = \frac{\vec{B}_0 - (\hat{k} \cdot \vec{B}_0)\hat{k}}{|\vec{B}_0 - (\hat{k} \cdot \vec{B}_0)\hat{k}|}$ and $\hat{e}_2 = \hat{k} \times \hat{e}_1 = \hat{k} \times \hat{B}_0$ are oriented at angle ψ relative to a parallel transported observer basis of the emitter frame. The ellipticity angle is given by $\chi = \tan^{-1}(E_{2,\text{Wave}}/E_{1,\text{Wave}})$ is given by χ

6.2 Interpolation

The interpolation scheme used is first order (linear) in space and zeroth order in time. Using linear interpolation to make a continuum approximation of the value of a quantity at (x^*, y^*, z^*) within a Cartesian lattice amounts to using the weighted average of the quantity values on the 8 nearest lattice points $\{x_{\min}, x_{\max}\} \times \{y_{\min}, y_{\max}\} \times \{z_{\min}, z_{\max}\}$, where the weight of each point (x_i, y_i, z_i) is $w_i = \frac{|x^* - x_i||y^* - y_i||z^* - z_i|}{x_{\text{Step}} y_{\text{Step}} z_{\text{Step}}}$. The extrapolation used for quantities outside the simulation prism was to simply set such quantities to 0. Due to the discrete nature of the time series of datablocks, it is not possible to vary the Galaxy time continuously along the line of sight at constant observer time. Thus, zeroth order interpolation was performed to assign the same $t_{\text{Gal}} = t_{\text{Obs}} + \lfloor \frac{\hat{n} \cdot \vec{r}}{z_{\text{Step}}} \rfloor t_{\text{Step}}$ to line of sight points no less than $\lfloor \frac{\hat{n} \cdot \vec{r}}{z_{\text{Step}}} \rfloor$ and less than $(\lfloor \frac{\hat{n} \cdot \vec{r}}{z_{\text{Step}}} \rfloor + 1)$ z -direction lattice

steps from the observer, where $t_{\text{Step}} = \frac{z_{\text{Step}}}{c}$. See Figure 6.2.

6.3 Adding an Observer

GRMHD simulations are often analyzed with respect to a fixed Galaxy frame [40]. However, if we add an observer receiving emitted radiation, the relevant time coordinate for comparison with observation measures the point at which light is incident upon the observer image plane (see <http://richardanantua.com/sample-page/simulation-geometry/>). At each observer time, emitting elements further from the image plane correspond to earlier Galaxy times than emitting elements from closer to the observer due to the time required for light to travel. Thus, the observer orientation relative to the simulation region affects the image formed by the line of sight projection. The capacity to view the simulation from rotating vantage points at constant observer time enables us to observe how the observers perceive special relativistic effects such as Doppler beaming of jet emission.

6.4 Image-Making Procedure

While AGN are believed to be fueled by plasma flows near the equatorial plane, often AGN sources are observed as being dominated by jet emission, as in the case of M87. Thus, in our efforts to study jets from simulations, several methods are employed in order to isolate the jets from other segments of the simulation. In Figure 6.4, for instance, we geometrically isolate the jet and counterjet with a paraboloid cut (note cylindrically symmetric cuts are more natural representation of the jet even in a rectangular prismic simulation block). Another jet-isolation procedure involves forming gas or magnetic energy per unit mass isocontours, which tend to trace the jet boundary as in Figure 6.5. The pair of Figures 6.4 and 6.5 gives an opportunity to make the important distinction between Simulation (Gal) Frame and Observer Frame times. Time in the Gal Frame starts at the beginning of the simulation and advances at the rate measured by an observer at rest ($\vec{v} = \vec{0}$) with respect to the black hole. Slices of the simulation at $T_{\text{Gal}} \equiv T = 2000M$ are shown in Figure 6.5. For each Observer Frame time image map in Figure 6.4, on the other hand, the 3D simulation from all retarded Gal Frame times $T_{\text{Obs}} \equiv t_r$ satisfying $T_{\text{Obs}} + \frac{\text{diam}/2}{c} < t_r < T_{\text{Obs}} + \frac{\text{diam}/2}{c}$ contribute to the image projected onto the observer plane.

6.4.1 C and C++ Routines

The C++ line-of-sight integration routines import and project binary file simulations of a 3D Cartesian lattice with x-index running faster than y-index running faster than z-index onto 2D observer arrays with ny changing faster than nx and exports the results into 1D-lists in the form of .txt

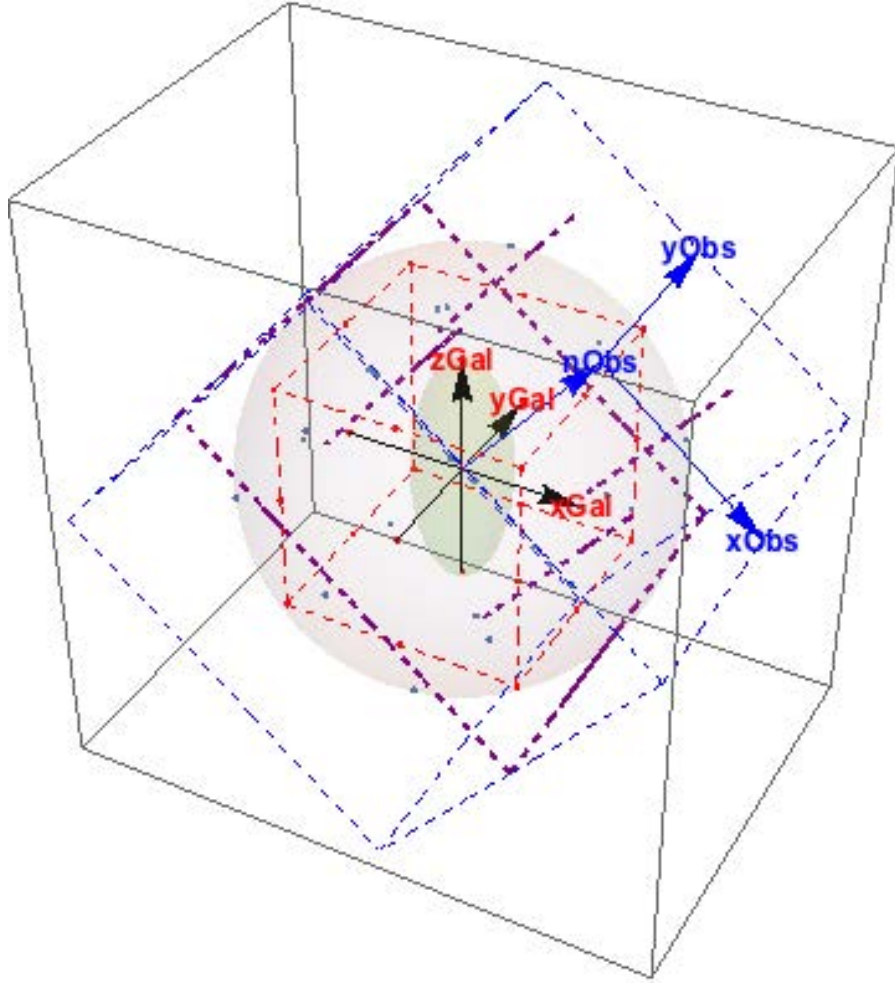


Figure 6.2: Observer coordinate lattice rotated about the Galaxy Frame Cartesian lattice. The $x_{\text{Obs}}\text{-}y_{\text{Obs}}$ plane origin is on the galaxy plane's circumscribing sphere in the n_{Obs} direction relative to the origin of the Galaxy Frame. All quantities on observer coordinate system lattice points (blue) are computed from first order linear interpolation of these quantities on nearest neighbor cells of the Galaxy Frame lattice (red), or extrapolated to zero if they are outside the simulation region bounded by the datacube. Integration can be performed slice-by-slice along lines of sight (purple) when the integrand is known throughout the simulation region.

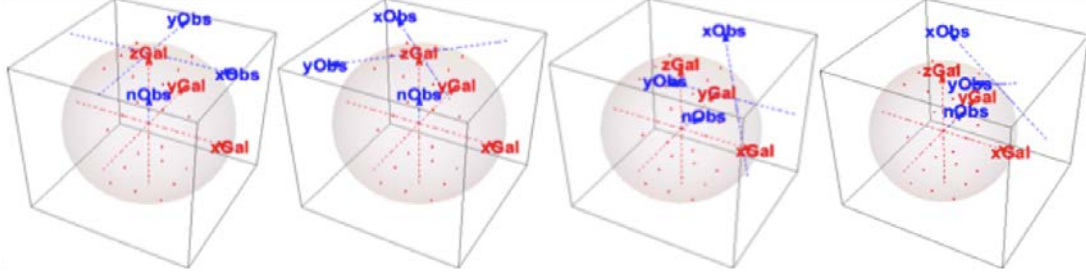


Figure 6.3: Rotating observer coordinates about fixed Galaxy frame Cartesian lattice. The x_{Obs} - y_{Obs} observer plane is initially parallel transported from the x_{Gal} - y_{Gal} -plane so the origin of the observer plane is tangent to the north pole of the galaxy plane's circumscribing sphere (Panel 1). The x_{Obs} - y_{Obs} -plane is first rotated about the z_{Gal} -axis to rotate 2D-projections from the 3D-simulation onto this plane (Panel 2). The x_{Obs} - y_{Obs} -plane is rotated in the polar direction relative to the simulation lattice (Panel 3). For the last rotation, the x_{Obs} - y_{Obs} -plane is rotated in the azimuthal direction.

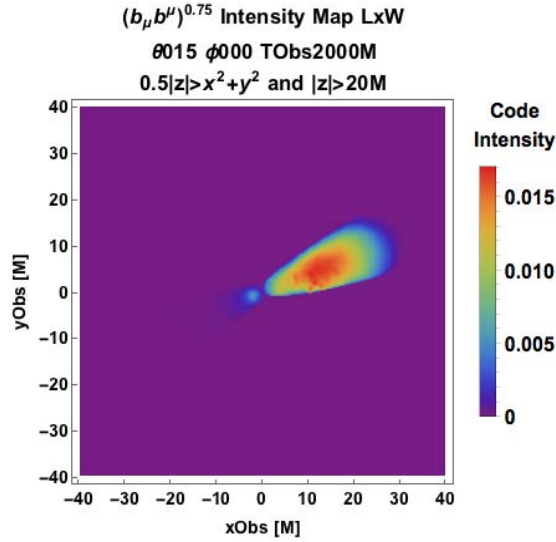
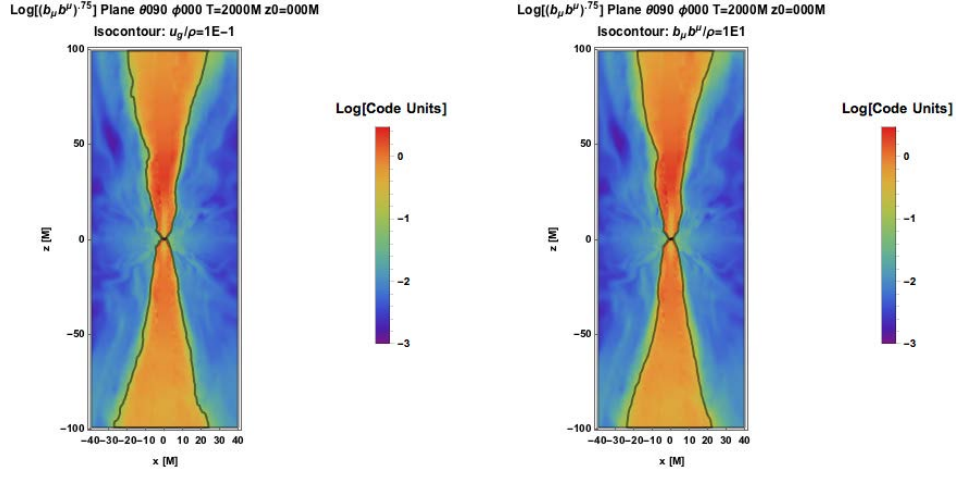


Figure 6.4: Simulated intensity map from generated from emissivity function $j \sim (b_\mu b^\mu)^{0.75}$ with geometrical jet isolation $|z| > x^2 + y^2 > 20$ viewed at 15° from the jet axis.



(6.6)

Figure 6.5: Log plots of $(b_\mu b^\mu)^{0.75}$ with isocontours $\frac{u_g}{\rho c^2} = 0.1$ (Panel 1) and $\frac{b_\mu b^\mu}{\rho c^2} = 10$ (Panel 2).

files. The main file is `ObservingJetSimulations.cpp`, which calls helper files such as `ObservingJetSimulationsInterpolationAndIntegration.h`, `ObservingJetSimulationsPolarization.h` and `ObservingJetSimulationsOpticalDepth.h`. A summary of the capabilities of the C++ image-making routines is as follows:

- File reading for simulation binary data files
`fieldline*.cart.bin.boxzh100.box256x256x256.out20.modelrunlocaldipole3dfdudicial`
 (using `ObservingJetSimulations.cpp`)
- Mapping observer times `tObs` to simulation spacetime regions contributing emission to an observer plane at constant observer time, removing the middle `2*HPillboxOn2/HSim` of the vertical simulation range to suppress disk emission
 (using `ObservingJetSimulations.cpp` and `ObservingJetSimulationsInterpolationAndIntegration.h`)
- Linear interpolation of physical quantities
 (using function
`float Interpolate3DCont(float x,float y,float z,float xMin,float yMin,float zMin,float xMax,float yMax,float zMax,float xStep,float yStep,float zStep, int NXs, int NYs, int NZs,float DataList[], int NumQuants , int QuantIndex)`
 from `ObservingJetSimulationsInterpolationAndIntegration.h`)

- Computing emission (from a list of emissivities j) from a plane normal to any observer direction $(\vec{n}(\theta, \phi))$
(using the function `ObservingJetSimulationsInterpolationAndIntegration.h: ObserverPlaneLoSIntegrand`)
- (Optional) computing polarization (from a list of emissivities j) from a plane normal to any observer direction $(\vec{n}(\theta, \phi))$
(using the function(s) `ObservingJetSimulationsPolarization.h: ObserverPlanePolLoSIntegrand`
`ObservingJetSimulationsOpticalDepth.h: ObserverPlaneLoSOpticalDepth`)
- Integrating emission from planes normal to the observer direction
(using `ObservingJetSimulations.cpp`)

The image-making routine is implemented by a command line argument via feeding parameters into Terminal. The parameters `tObs, θ, ϕ , HPillboxOn2/HSim, j, fieldline*.cart.bin.boxzh100.box256x256x256.out20.modelrunlocaldipole3dfiducial` are input as follows:

```
// At runtime, enter 1.) TObs; 2.) ThetaObs (degrees); 3.) fPhi = PhiObs (degrees); 4.)
ThickOn2 =.5*HPill/H (Half-thickness of pillbox to cut disk from); 5.) Emissivity prescription
from list [ L0)D, L1)d2.5bSq, L2)D2.5(1/3)Ug*bSq3, L3)D2.5bSq*Rho.75, L4) bSq ]; 6.) Filename
wildcard
// ./a.out 2010 30 0 .1 4 fieldline*.cart.bin.boxzh100.box256x256x256.out20.modelrunlocaldipole3dfiducial
```

6.4.2 Mathematica Routines

Mathematica 10.0.1.0 is a flexible yet powerful tool for rendering images from files of several formats including `.txt`. To post-process text file data, we import the list and populate arrays that will ultimately be displayed as density plots. We populate the observer arrays Mathematica in the `ny` faster than `nx` sequence they appear in imported data lists. In pseudocode,

```
For[nx=1,nx≤NXs,nx++,
  For[ny=1,ny≤NYs,ny++,
    ObsArray[[nx]][[ny]]=TextList[[ny+NXs*(nx-1)]]
  ]
]
```

Note that Mathematica 2D array plot values are distributed in a manner corresponding to the position of array components in matrix form (see Figure 6.6). In order to convert 2D arrays displayed this way (`nx` increasing downward and `ny` increasing to the right) into a standard Cartesian 2D plane with origin on the lower left and `x` increasing rightward and `y` increasing upward, one could use

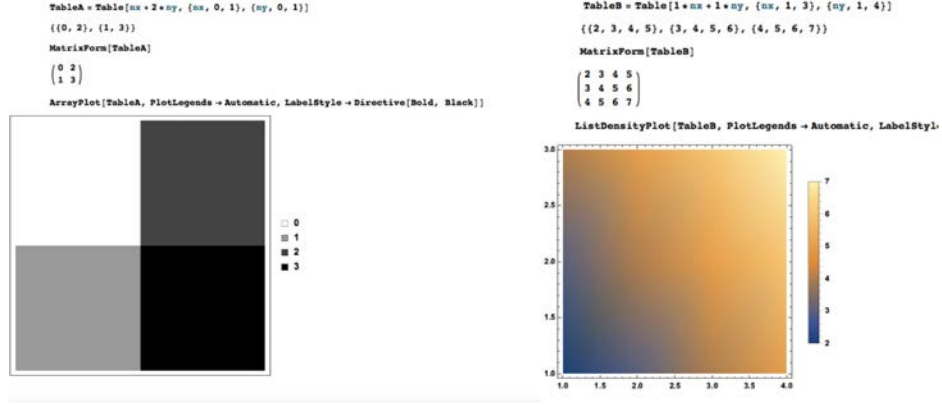


Figure 6.6: Mathematica ArrayPlot (left panel) and ListDensityPlot (right panel).

transformations $ny \rightarrow NYs - (ny - 1)$ followed by transposition $nx \leftrightarrow ny$. Note also that Mathematica's ListDensityPlot need not agree with the matrix form of its content (see Figure 6.6).

6.5 Connecting with Observation

Using rather long movies that from several different azimuths, we attempt to replicate the features. For mm wavelengths, superluminal features may occur at $< 2000M$. To accurately gauge the distance from the quasar, We must account for cosmological considerations such as the expansion speed of the universe and the fact that the duration measured on Earth is longer by a factor $(1+c)$ than that of a local observer. We wish to compare the observational $(c\Delta t/L_{\text{jet,proj}})$ to similar simulation time scales $(c\Delta t/L_{\text{jet,proj}})$ where $L_{\text{jet,proj}}$ is the length up to which features extend from the black hole for the observations and the origin for the simulations.

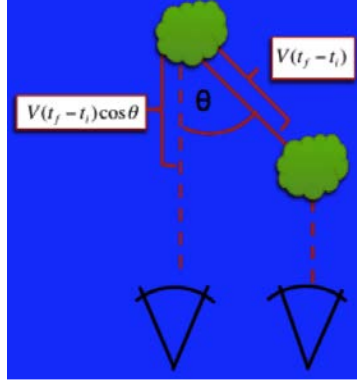
6.5.1 Superluminal Motion

We have seen that because of the finite speed of light, each observed time at the observer plane corresponds to a 3D de-projected region at various retarded times. AAnother geometrical light travel time effect is that the apparent transverse speed $v_{t,\text{app}}$ of a feature projected on the observer plane may be superluminal:

$$v_{t,\text{app}} = \frac{v(t_f - t_i) \sin \theta}{v(t_f - t_i) - \tau}, \text{ where } \tau = \frac{v(t_f - t_i) \cos \theta}{c} \quad (6.7)$$

$$\implies v_{t,\text{app}} = \frac{v \sin \theta}{1 - \frac{v \cos \theta}{c}}$$

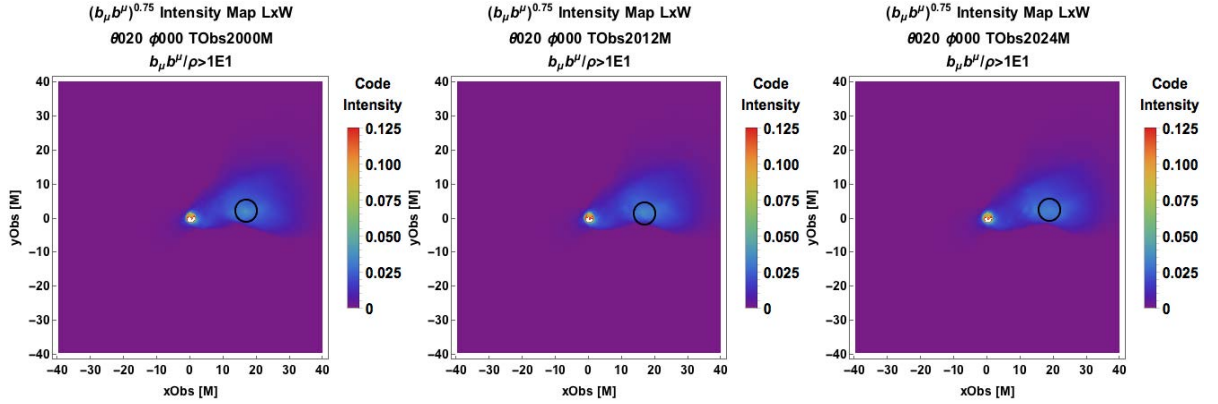
due to the path length difference depicted in Figure 6.8.



(6.8)

Figure 6.7: Geometry for apparently superluminal projections.

Moving features may not be distinct enough to be tracked by eye as in the generic simulation. A simple approach to address this, is to center a circle of small radius around the measured intensity maximum and track for several frames, as in Figure 6.8.



(6.9)

Figure 6.8: Frame-by-frame tracking of a moving knot of high intensity. The circle has radius $3.125M$ and is centered on the maximum intensity pixel of the simulated image. The maximum observed speed here is $v \sim 0.5c$.

We now extend the flexibility of our "Observing Jet Simulations" pipeline to observe different astrophysical object using the same simulation oriented at varying angled and with various emission prescriptions.

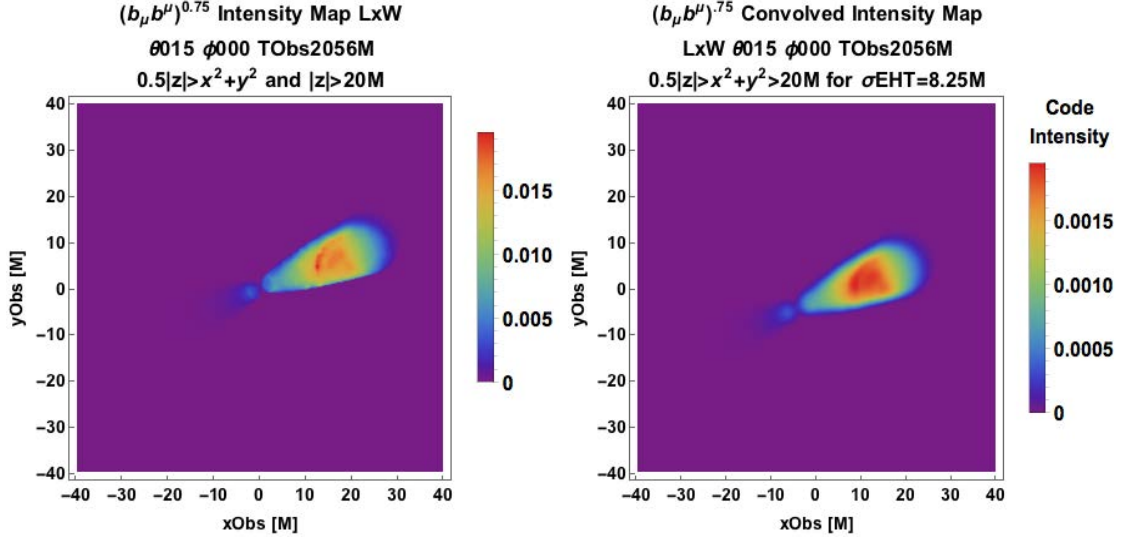


Figure 6.9: Simulated intensity map at TObs=2056M generated from emissivity function $j \sim (b_\mu b^\mu)^{0.75}$ with $|z| > 20$. The left panel is not convolved and the right panel is convolved with a Gaussian point spread function of width $8.25M$.

6.6 Instrumentation and Convolution

An important aspect of instrumentation is the cadence, or frame rate, of an observation. For example, VLA observations of M87 at 43GHz have been taken at a cadence of one per 21 days ($\sim 56M$). The simulation Idumps $\mathfrak{I}1$ have timestep $2M$, so the approach of making a simulated jet movie to emulate tracking observational features is feasible as the simulation temporal resolution is finer than the observational cadence.

The computational resolution set by the simulation lattice step sizes is often not the limiting factor for the final observed resolution. The final step in converting simulation output into observations is convolving intensity maps with the point spread function appropriate for the instrument used by astronomers to view the target object. The observed image is a density map of

$$g(x, y) = \int_{-\infty}^{\infty} \int_{-\infty}^{\infty} PSF(\alpha, \beta; x, y) I_\nu(\alpha, \beta) d\alpha d\beta + \eta(x, y) \quad (6.10)$$

where PSF is the point spread function, and η is an additive noise function.

The highest VLBA resolutions at 5GHz and 43GHz are 0.9mas and 0.1mas, respectively [16]. The Event Horizon Telescope promises to perform 1mm VLBI at an angular resolution of $25\mu\text{as}$ [34] at the Galactic Center.

Chapter 7

Application I. Comparison with M87

With a central black hole subtending $3.9\mu\text{as}$ on the sky— comparable to $5.3\mu\text{as}$ for Sgr A*— M87 is a prime target of observation for event-horizon-scale future observations due to its size and powerful jet. Our choice of mass for M87’s central black hole, derived from stellar dynamics to be $6.6 \cdot 10^9 M_\odot$ [22], is not without controversy. Walsh et al. [60] have used gas dynamical models of emission line kinematics for the inner 40 pc of M87 to arrive at a black hole mass of $3.5 \cdot 10^9 M_\odot$. M87’s viewing angle of $10^\circ - 19^\circ$ [19] is propitious for observers and simulators alike, since it is large enough to have significant projected extent on an observer plane, and small enough to exhibit relativistic Doppler beaming. Barring a preferred direction for the Universe, the distribution of orientations of astrophysical jets relative to our line of sight should be random on the scale of galaxy clusters. BL-Lacertae objects are active galactic nuclei with jets oriented towards Earthbound observers, and have been seen from radio to TeV energies [5]. We are fortunate to have the giant elliptical galaxy M87 as a nearby unbeamed BL Lac jet to study.

7.1 M87 - Prototypical Unbeamed BL-Lac

Located at the heart of the Virgo Cluster 16.7 ± 0.6 Mpc away [9], the bright active galaxy M87 (3C 274) serves as a convenient laboratory for the investigation of black hole jets. M87 is a Fanaroff-Riley (FR) I misaligned BL-Lac blazar. The one-sidedness of its inner jet suggest that it is subject to modest relativistic beaming (to a lesser extent than true blazars). We choose an inclination of the spin axis to the line of sight of $\theta = 20^\circ$, consistent with the analysis of [61] and suggesting that we are viewing outflows moving with Lorentz factors ~ 3 (our findings are not sensitive to this choice). The largest superluminal speeds from HST Knot 1 have reached $6c$ [8]. Large scale radio features

in the surrounding cluster suggest that M87 has been active for at least several Gyr although the underlying mass supply rate has probably varied significantly over this time. Tables 1, 2 and 3 summarize key properties of M87

Table 1: M87 dimensions. ¹[22], ²[19]

Schwarzschild radius	Apparent angular width ¹	Angular width of M	Jet opening angle ²
$(6.35 \times 10^{-4} \pm 3.69 \times 10^{-5})\text{pc}$ $(1.96 \times 10^{15} \pm 1.14 \times 10^{14})\text{cm}$	$3.9\mu\text{as}$	$(3.7 \pm 0.3)\mu\text{as}$	5° (@100pc) 60° (core)

Table 2: M87 location and orientation. ¹[9], ²[61]

Distance from Earth ¹	Jet viewing angle ²
$(16.7 \pm 0.6)\text{Mpc}$ $(5.15 \times 10^{25} \pm 2.78 \times 10^{24})\text{cm}$	$10^\circ - 19^\circ$

Table 3: Code scale M to physical units for M87

Unit type	M
Mass	$(6.6 \pm 0.4) \times 10^9 M_\odot$
Length	$(3.2 \times 10^{-4} \pm 1.8 \times 10^{-5})\text{pc}$
Angular width at d_{M87}	$(3.7 \pm 0.3)\mu\text{as}$
Time	$(9.1 \pm 0.8)\text{h}$

7.1.1 Radio Observations of M87

In this chapter, we focus on a 43 GHz VLBI time sequence– 11 maps made over 210 d with a beam FWHM $210\mu\text{as} \times 430\mu\text{as}$ [59]. Observations at similar frequencies include Kovalev’s 15 GHz map with beam $600\mu\text{as} \times 1300\mu\text{as}$ [30] and model-dependent intensity maps based on sparse 230 GHz Event Horizon Telescope (EHT) observational data [4]. The 43 GHz images, which extend out to ~ 25 mas in projected radius, show a slowly expanding, edge-brightened, approaching jet that is already well-collimated on the smallest scale observed. Larger scale maps that can be used to improve our understanding of the jet composition, power, speed and inclination are better understood in the self-similar model of Chapter 4.

7.2 Comparing Simulated Intensity Maps with Observations

7.2.1 Collimation

Collimation is an important aspect of jet morphology that can inform us about jet formation processes and the jet's surrounding medium. It has previously been addressed by semi-analytic models such as, Globus and Levinson [23], which compared an axisymmetric hydrodynamic jet collimated by pressure support from a shocked wind layer originating from the disk to the jet profile

$$\begin{cases} s \propto z^{0.8}, & 0M \leq z \lesssim 10^2 M \\ s \propto z^{0.58}, & 10^2 M \lesssim z \lesssim 10^5 M \\ s \propto z, & z \gtrsim 10^5 M \end{cases}$$

that the EHT and Very Long Baseline Array (VLBA) combine to observe. The “observing” jet simulations approach allows us to compare a suite of prescriptions to phenomenologically determine which is most likely to explain M87’s collimation profile. In Figure 7.1, we see that the bias model in which $u_g \sim b^0$ and $j \sim b^{3/2}$ provides a better fit to observed collimation than the β model where $j \sim b^{7/2}$.

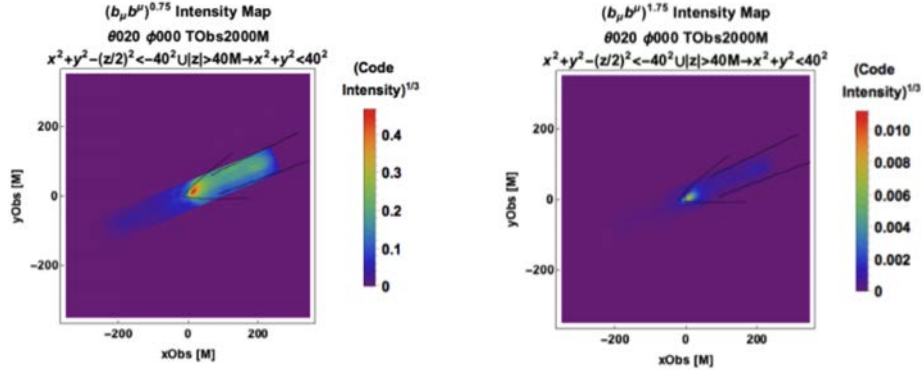


Figure 7.1: Bias model with constant gas pressure (left panel) and beta model (right panel) viewed at 20° from the jet axis. The contours are the collimation profiles deduced from VLBA and EHT data. The figures have been transformed by $(\cdot)^{1/3}$ for visual contrast.

7.2.2 Comparing Simulation and Observation Scales

Some of the intensity maps generated from our (impressionistic thus far) emissivity prescriptions have reproduced some observed features qualitatively. We perform the quantitative exercise of fitting simulated intensity maps to an observation, gaining perspective on the relative scales of simulation

and observation in the process. For bias models, whose only dynamical variable is the magnetic field, we can read off the scaling factor between physical and simulated magnetic field strengths $b = \kappa_b \tilde{b}$ by comparing intensity maps and using the Lorentz invariance of j_ν/ν^2 . Let us investigate this with the comoving fluid frame synchrotron model

$$j_\nu = K P_e P_{\text{Mag}}^{\frac{1+\alpha}{2}} \nu_{\text{Com}}^{-\alpha} \quad (7.1)$$

, where $P_{\text{Mag}} = \frac{b^2}{2\mu_0}$. The observer frame synchrotron model is then

$$(j_\nu)_{\text{Obs}} = \mathcal{D}^{2+\alpha} K P_e P_{\text{Mag}}^{\frac{1+\alpha}{2}} \nu_{\text{obs}}^{-\alpha} \quad (7.2)$$

where $\alpha = \frac{p-1}{2}$, $\nu_{\text{Obs}} = \mathcal{D} \nu_{\text{Com}}$ and P_e and P_{Mag} are in terms of comoving fluid variables. Writing

$$\begin{cases} P_e \equiv C_1 P_{\text{Mag}}^{n_1} \\ P_{\text{Mag}} \equiv C_2 b^2 \end{cases}$$

$$\implies (j_\nu)_{\text{Obs}} = \mathcal{D}^{2+\alpha} K C_1 C_2^{\frac{1+\alpha}{2} + n_1} (b^2)^{\frac{1+\alpha}{2} + n_1} \nu_{\text{Obs}}^{-\alpha} \quad (7.3)$$

Setting $A \equiv K C_1 C_2^{\frac{1+\alpha}{2} + n_1}$ and $n \equiv \frac{1+\alpha}{2} + n_1$,

$$(j_\nu)_{\text{Obs}} = \mathcal{D}^{2+\alpha} \nu_{\text{Obs}}^{-\alpha} A (b^2)^n \quad (7.4)$$

The radiative transfer equation gives

$$(I_\nu)_{\text{Obs}} = \int (j_\nu)_{\text{Obs}} ds = A \int \mathcal{D}^{2+\alpha} \nu_{\text{Obs}}^{-\alpha} (b^2)^n ds \quad (7.5)$$

where the line element is given in the observer frame. We now scale the units as follows:

$$\kappa_b = \frac{[b]}{[\tilde{b}]}, \quad \kappa_\nu = \frac{[\nu]}{[\tilde{\nu}]}, \quad \kappa_s = \frac{[s]}{[\tilde{s}]}, \quad (7.6)$$

where tildes are for simulation versions of the physical quantities. Comparing code intensity

$$(\tilde{I}_\nu)_{\text{Obs}} = A \int \mathcal{D}^{2+\alpha} \tilde{\nu}_{\text{Obs}}^{-\alpha} (\tilde{b}^2)^n d\tilde{s} \quad (7.7)$$

to Eq. 7.5 expressed in code units

$$(I_\nu)_{\text{Obs}} = A \int \mathcal{D}^{2+\alpha} (\kappa_\nu \tilde{\nu}_{\text{Obs}})^{-\alpha} (\kappa_b \tilde{b})^{2n} \kappa_s ds \quad (7.8)$$

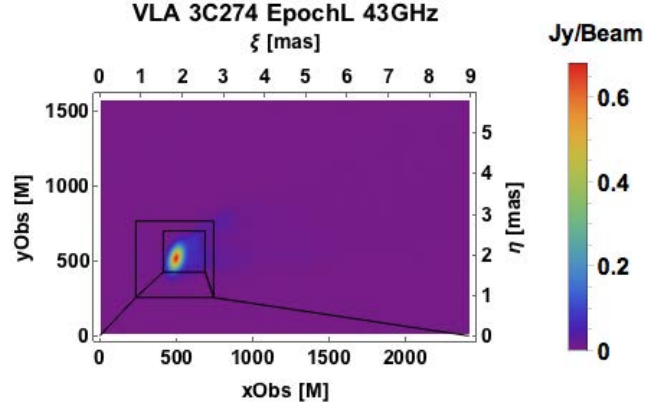
to give (dropping the "Obs" subscript)

$$\begin{aligned} [I_\nu] &= [\kappa_\nu \nu_{\text{Obs}}]^{-\alpha} [\kappa_b \nu_b]^{2n} [\kappa_s ds] = \kappa_s \kappa_\nu^{-\alpha} \kappa_b^{2n} [A \mathcal{D}^{2+\alpha} \tilde{\nu}_{\text{Obs}}^{-\alpha} \tilde{b}^{2n} d\tilde{s}] \\ &= \kappa_s \kappa_\nu^{-\alpha} \kappa_b^{2n} [\tilde{I}_\nu] \end{aligned} \quad (7.9)$$

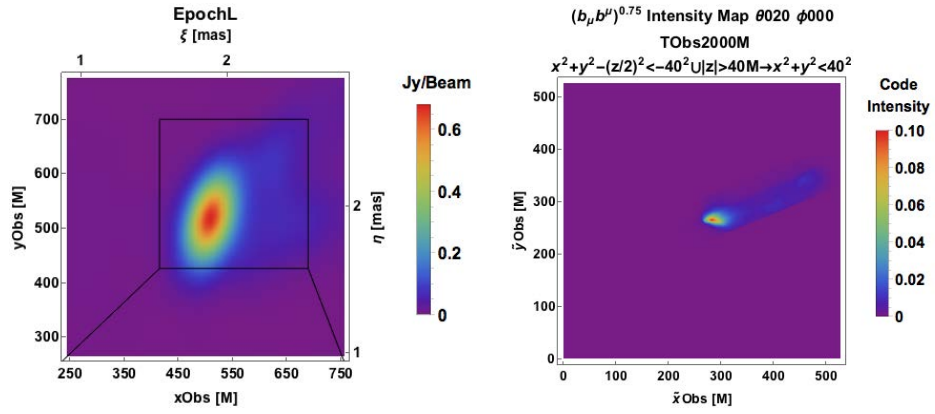
For the fiducial dipole simulation with length units of M from MTB12, $\kappa_s = (GM_{\text{source}}/c^2)_{\text{cgs}}/M$. For $(\alpha, n_1) = (0.5, 0)$, $[I_\nu]/[\tilde{I}_\nu] = \kappa_s \kappa_\nu^{-0.5} \kappa_b^{1.5} \equiv \kappa_{(0.5,0)}$; for $(\alpha, n_1) = (0.5, 1)$, $[I_\nu]/[\tilde{I}_\nu] = \kappa_s \kappa_\nu^{-0.5} \kappa_b^{3.5} \equiv \kappa_{(0.5,1)}$. Fitting simulated intensity maps with emissivity $(b_\mu b^\mu)^{\frac{3}{4}} \nu_{\text{Obs}}^{\frac{1}{2}}$ to Craig Walker's VLA 43GHz M87 Epoch L image by minimizing the statistic

$$\chi^2 = \sum_{i=1}^{N_{\text{Rows}}} \sum_{j=1}^{N_{\text{Columns}}} \frac{(I_{ij,\text{Obs}} - \kappa I_{ij,\text{Sim}})^2}{I_{ij,\text{Obs}}^2} \quad (7.10)$$

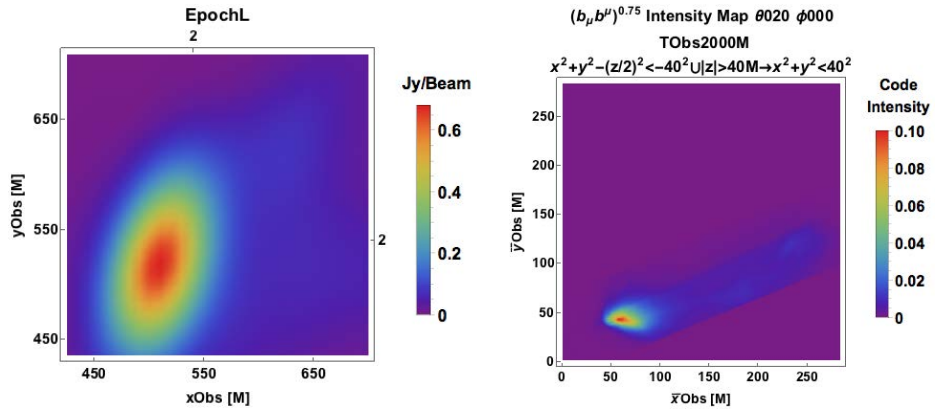
, we find $\kappa_{(0.5,0)} = 5.55$ (for the image given in $\frac{\text{Jy}}{\text{beam}}$) as in Figure 7.2



(7.11)



(7.12)



(7.13)

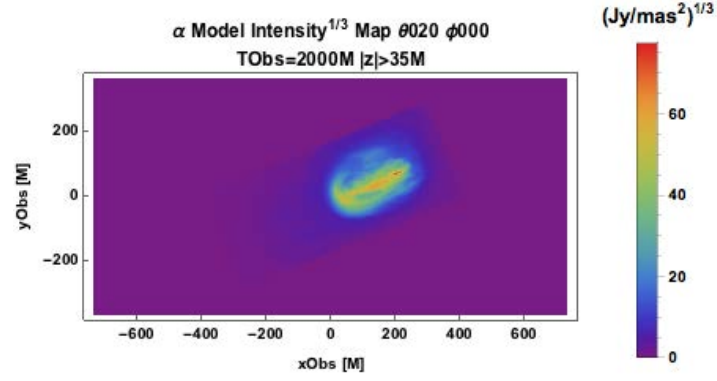
Figure 7.2: M87 VLA observations (left column) side-by-side with simulation at $2000M$ (right column) at comparable scales. The intensity maps are generated from emissivity function $j \sim (b_\mu b^\mu)^{0.75}$ with disk subtraction $x^2 + y^2 + (z/2)^2 < -40$ ($x^2 + y^2 < 40$ & $|z| > 40M$). In the top right panel, the $\hat{x}\text{Obs}-\hat{y}\text{Obs}$ -coordinate system charts a 650×650 -pixel sub-plane of the a 1731×1731 -pixel ($1404M \times 1404M$) $x\text{Obs}-y\text{Obs}$ plane with axes aligned in the same orientation and the same origin. In the bottom right panel, the $\bar{x}\text{Obs}-\bar{y}\text{Obs}$ -coordinate system charts a 350×350 -pixel sub-plane of $\hat{x}\text{Obs}-\hat{y}\text{Obs}$ with origin displaced towards Quadrant III by $(-150 \text{ pixels}, -150 \text{ pixels})$.

Alternatively, since $\frac{\text{Jy}}{\text{beam}} = 10^{-26} \frac{\text{W}}{\text{m}^2 \text{Hz}} \frac{1}{2.1 \cdot 10^{-4} \text{arcs} \cdot 4.3 \cdot 10^{-4} \text{arcs}} = \frac{4.25 \cdot 10^{-16}}{9.043 \cdot 10^{-8}} \frac{\text{W}}{\text{m}^2 \text{Hz} \cdot \text{sr}} = 4.70 \cdot 10^{-9} [I_\nu]_{\text{S.I.}} = \frac{4.25 \cdot 10^{-16}}{9.043 \cdot 10^{-8}} \frac{10^8 \text{erg}}{(100 \text{cm})^2 \text{Hz} \cdot \text{sr}} = 4.70 \cdot 10^{-6} [I_\nu]_{\text{cgs}}$, the numerical value of the scale factor $\kappa_{(0.5,0)} = 5.55 \cdot 4.70 \cdot 10^{-9} = 2.61 \cdot 10^{-8}$ (for S.I. physical observation) and $\kappa_{(0.5,0)} = 5.55 \cdot 4.70 \cdot 10^{-6} = 2.61 \cdot 10^{-5}$ (for cgs physical observation).

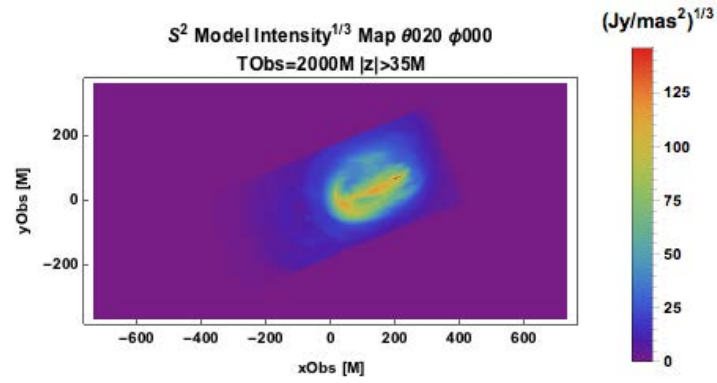
Using M87 to fix the mass, distance and time scales, we have $\kappa_s = \frac{1.96 \cdot 10^{15}}{2} = 9.73 \cdot 10^{14}$ —the ratio of M87's central black hole's Schwarzschild radius measured in cm versus measured in gravitational radii. Likewise, $\kappa_\nu = 3.08 \cdot 10^{-5}$ is the ratio of frequency measured in c^3/GM_{M87} to frequency measured in Hz. Then our fit yields magnetic field simulation-unit-to-gauss scaling factor $\kappa_b = \left(\frac{\kappa_{(0.5,0)}}{\kappa_s \kappa_\nu^{-1/2}} \right)^{2/3} = \left(\frac{2.61 \cdot 10^{-5}}{9.73 \cdot 10^{14} \cdot (3.08 \cdot 10^{-5})^{-0.5}} \right)^{2/3} = 2.81 \cdot 10^{-15}$. When using this scale to convert to physical units, one must keep in mind that intensity does not have the units of $[b]^{3/2}$, so it may be convenient to rewrite the code intensity with a prefactor containing physical constants with the appropriate units.

7.2.3 Comparing Prescriptions with Dissipation

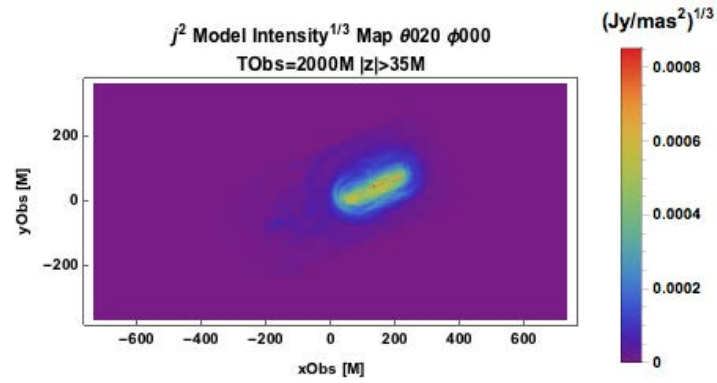
The synchrotron intensity maps exhibited thus far used simple scaling relations that dropped factors relating to magnetic field anisotropy and did not account for frequency-dependent effects such as optical thickness. The prescriptions that follow express \tilde{P}_e in the physically intuitive form of a dissipation rate per unit volume times the cooling time of the source particles. The cooling time is taken to be the minimum of the cooling and expansion times. The dissipation rate in some models will also be related to physical quantities such as shear stress τ , shear strain S , and current density j^α . In order to see accentuate structure from our synchrotron models, Figure 7.3 shows ray tracing in the case opacity is set to 0 for the α -, S^2 - and j^2 -models.



(7.14)



(7.15)



(7.16)

Figure 7.3: Intensity maps of alpha (top panel), shear (middle panel) and current density (bottom panel) models at 43GHz with parabolic disk subtraction viewed from 20° at $T_{\text{Obs}} = 2000M$. The maps are transformed by $(\cdot)^{1/3}$.

The α -model can be interpreted as relating the dissipation to momentum transport. τ is to be conceptualized as a pressure that forces momentum outward. The shear model can be interpreted as accelerating particles in regions of high shear. It is edge brightened relative to the α -model, suggesting velocity shear is prominent at the boundary. For the current density model, the spine of jet is most intense because, as in Ch. 3, the current density j takes on its highest values for a core of small cylindrical radius.

Increasing frequency to 243 GHz, we anticipate the EHT. In Figure 7.4, using the j^2 model, we see an effect predicted by our prescriptions: that one side of the jet is preferentially brighter, breaking bilateral symmetry. where values of magnetic field pitch angle make $B_e = |\vec{B} \times \hat{n}|$ very different on both sides of the jet. This effect is expected at small enough radii from the black hole that it can still be considered a prediction for the EHT.

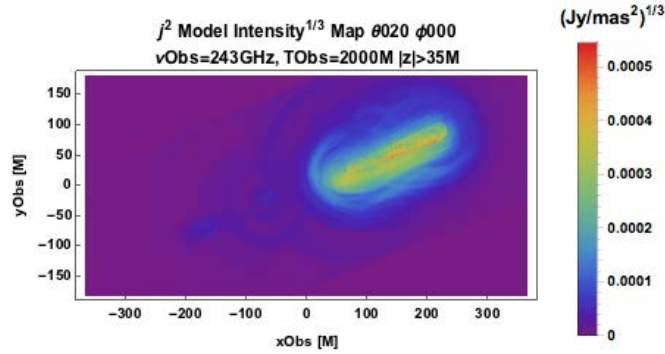


Figure 7.4: Intensity map at $T_{\text{Obs}} = 2000M$ viewed at 20° using synchrotron absorption in the j^2 prescription at 243GHz. The bottom edge of the jet appears brighter than the top edge, possibly due to a difference in magnetic field pitch angle across the jet.

Now, we include a synchrotron opacity function with partial pressure given by the j^2 -model in Figure 7.5. Though M87's inner jet is expected to be optically thin at this frequency, this prescription fails to reproduce this for model parameter $L = 1$. A force-free analytic model in which the jet footprint is set at a radius of $40M$ and the jet is modeled as a parabola $z \sim s^{0.5}$ is shown at 230 GHz and 345 GHz in Figure 7.6 for comparison.

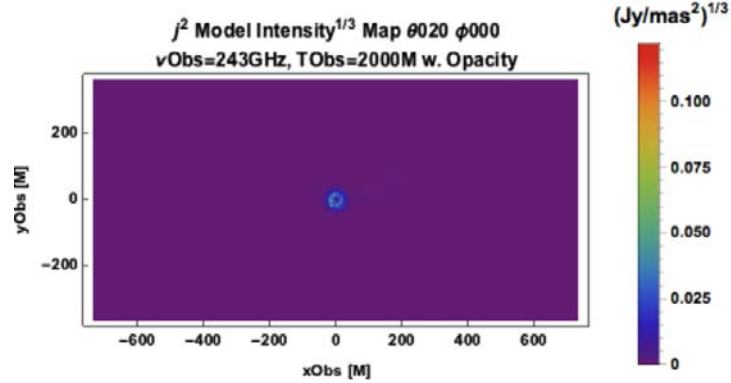


Figure 7.5: Optically thick intensity map at $T_{\text{Obs}} = 2000M$ viewed at 20° using synchrotron absorption in the j^2 prescription at 243GHz.

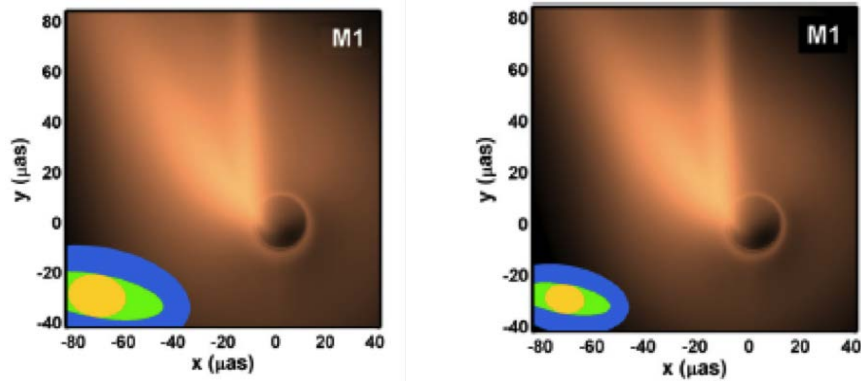
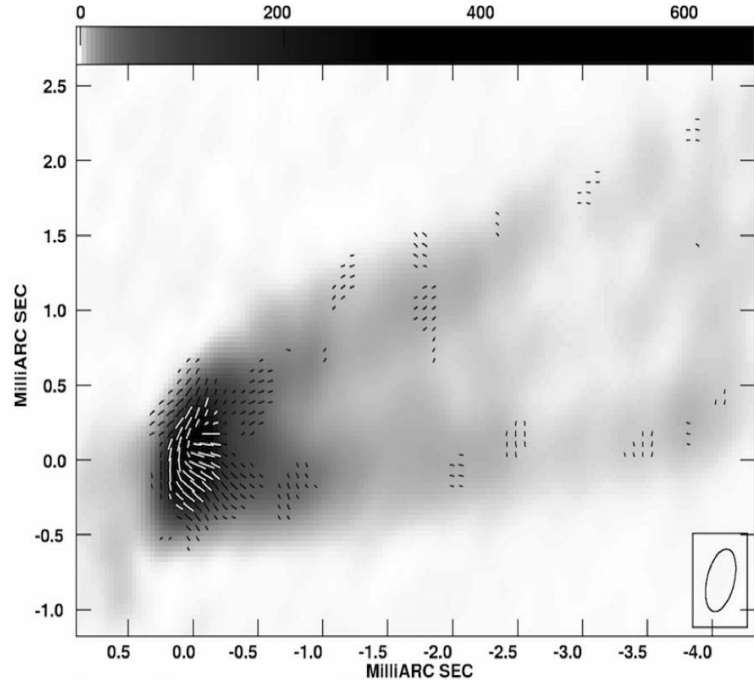


Figure 7.6: Model of EHT jet footprint at 243 GHz and 345 GHz. The beam is significantly smaller for the higher frequency observation. Courtesy of Avery Broderick and Avi Loeb [15].

7.3 Comparison with Polarization Observations

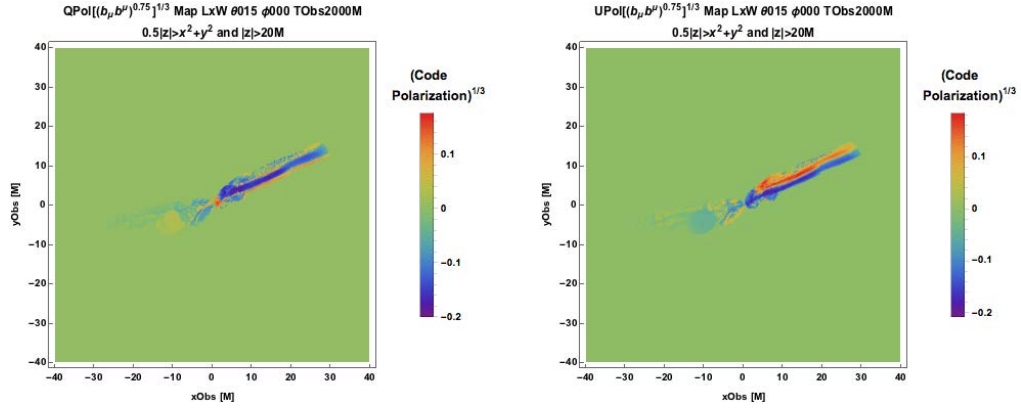
To incorporate into our comparison of the simulation with observations, let us focus on VLA-observed E -field orientations at 43GHz, which trace polarized regions in Figure 7.7. This observation suggests limb brightened polarization and a relative absence of polarization near the jet spine. We compare these to Stokes maps of linear polarizations U and Q made using our routines. In the bias model Figures 7.8 and 7.7, linear polarization is seen by observers at 15° and 20° viewing angles, respectively. Stokes Q and U change sign across the jet as the magnetic field geometry reverses. In



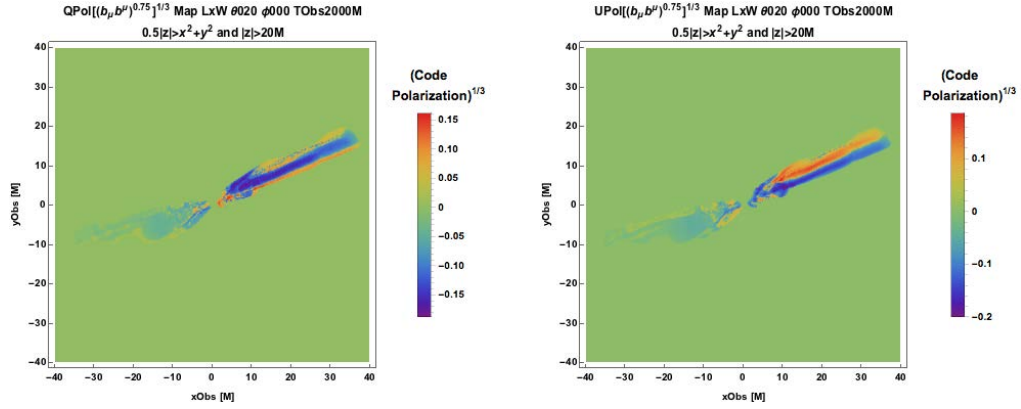
(7.17)

Figure 7.7: Polarization map of electric field vectors at Epoch G of the 43GHz VLA observation. Courtesy of Craig Walker (NRAO).

the simulated models, a pillbox $70M$ in total height was subtracted from the middle of the simulation in order to prevent contamination from emission processes from the disk that differ from those in the jets. The U maps are limb brightened and have a region of low polarization near the spine as U changes sign. The Q polarization is orthogonal to U . Interpreting observations of circular polarization V is more complicated, requiring a model for the structure of jet magnetic fields. At 243GHz— a frequency that will be accessible to the Event Horizon Telescope— emission should be optically thin the outer jet, where polarization can be measured and ray-tracing by integration can be carried out accurately by the routines in this work.



(7.18)



(7.19)

Figure 7.8: Maps of linear polarizations Q (left panels) and U (right panels) generated from emissivity function $j \sim (b_\mu b^\mu)^{\frac{3}{4}}$ with parabolic disk subtraction viewed from 15° (top panels) and 20° (bottom panels) at $T_{\text{Obs}} = 2000M$. These maps are transformed by $(\cdot)^{1/3}$ and calculated using the polarization geometry of Chapter 6.

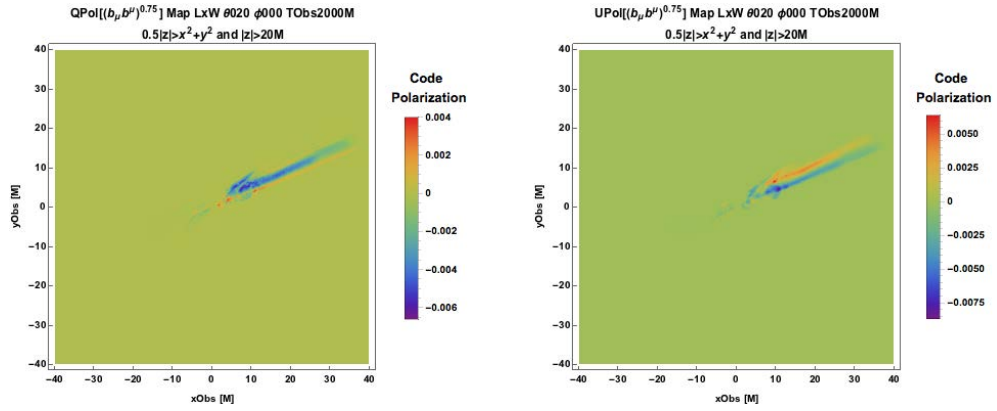
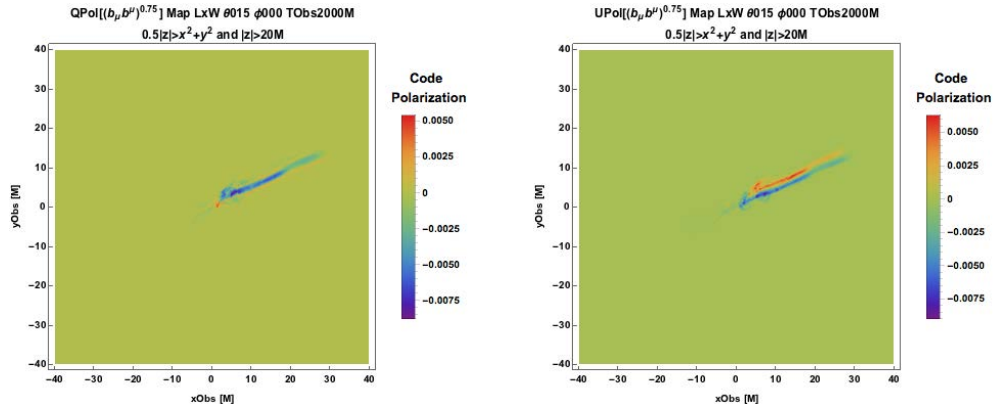


Figure 7.9: Maps of linear polarizations Q (left panels) and U (right panels) generated from emissivity function $j \sim (b_\mu b^\mu)^{\frac{3}{4}}$ with parabolic disk subtraction viewed from 15° (top panels) and 20° (bottom panels) at $T_{\text{Obs}} = 2000M$. These maps are calculated using the polarization geometry of Chapter 6.

Chapter 8

Application II. Comparison with 3C 279

In June 1991, the space-based telescope *EGRET* discovered gamma radiation from the optically violent variable (OVV) quasar 3C 279 (R.A. $12^{\text{h}}56^{\text{m}}$, decl. $-5^{\circ}47'$, $z=0.54$). The quasar’s luminosity is $M_{\text{R}} = -23.8$ in absolute magnitude, and the black hole mass/bulge luminosity relation yields a 1 billion solar mass central black hole [43]. One gamma ray component of 3C 279’s emission has been explained by the synchrotron self-Compton mechanism, in which the same electron population producing 10^{13} - 10^{16} Hz (0.041 eV-41 eV) X-rays produces inverse Compton gamma rays [35]. However, it is normally presumed for high-power quasars that the component dominating the highest energy gamma rays is external inverse Compton [27]. In 2015, the first VLBI fringes at 230 GHz of 3C 279 were seen by the Atacama Pathfinder Experiment (APEX) telescope (along with baselines including the sub-millimeter array (SMA) and sub-millimeter telescope (SMT)), and the emitting region was found to be $38 \mu\text{as}$ [58]. 3C 279 has also recently provided us with the surprise of 5-minute-scale variability in the 100 MeV-1 GeV emission band in a spectacular 2015 outburst [55]. The EHT, including ALMA, will soon constrain the size of 3C 279’s emitting region better than APEX, giving us a better understanding of its variability. Bright gamma ray intensity and variability make 3C 279 a prime target of observation for the inverse Compton modeling portion of the “Observing Jet Simulations” pipeline.

8.1 3C 279 - Flat Spectrum Radio Quasar

8.1.1 Accretion Disk

The large accretion disk surrounding 3C 279 radiates blackbody emission observed at temperature $\Theta = 20,000\text{K}$ – translating to $(1+z)20,000\text{K}=31,000\text{K}$ at the source– and powers broad line

emission [46]. The observed peak frequency is 1.6 PHz (2.5 PHz at the source). The UV luminosity from the disk can be estimated by $\nu L_\nu \approx 2 \cdot 10^{38}$ W. Several percent of the radiated photons are reprocessed by emission line clouds, free electrons in the hot inter-cloud medium, or the accreting gas itself. The disk contributes an anisotropic component to the ambient soft photon field that makes a small angle along the 3C 279 jet axis at high altitude. The soft photon field serves as both a source of emission and opacity for the jets.

8.1.2 Spectrum and Variability

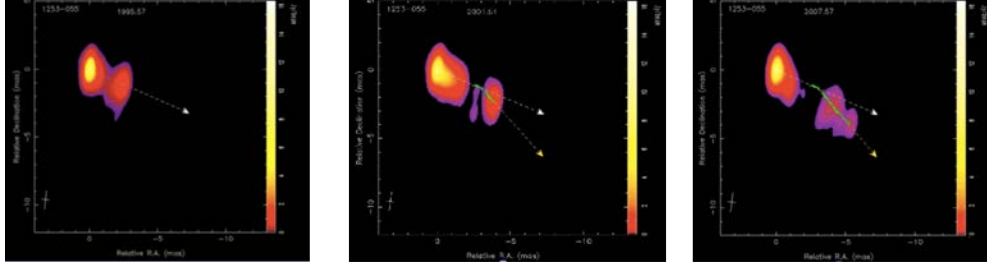
The quasar 3C 279 has a two-humped spectrum¹ (νF_ν) with local minimum $\sim 10^{16}$ Hz (or 15 PHz at the source). The spectrum is flat at low frequencies, consistent with 3C 279's classification as a flat spectrum radio quasar (FSRQ). The spectrum has a disk component peaked at $\sim 10^{15}$ Hz, disk emission Comptonized in the jet peaked at $\sim 10^{21}$ Hz, a synchrotron self-Compton component from the jet peaked near 10^{20} Hz and a more prominent peak due to BLR emission above 10^{23} Hz [27].

3C 279 is optically violently variable and more variable at higher frequencies [35]. The observed 5-minute variability of VHE gamma radiation from 3C 279 1.3 described in Chapter 1 is even shorter—3 minutes— at the source when we account for cosmology.

8.1.3 Superluminal Motion

Using the 3C 279 black hole scales of $1 \mu\text{as} = 0.0064$ pc found in [58], the angular diameter distance to 3C 279 is 1.3 Gpc (corresponding to luminosity distance a factor of $(1+z)^2$ greater, 3.1 Gpc). 3C 279 has a reported maximum jet speed of $651 \pm 25 \mu\text{as/yr}$ (or 20.58c) [37]. The jet is seen to eject a superluminal blob in the period from 1995-2007 in Figure 8.1. Simulations and our model suppose that the large speeds necessary develop superluminal motion occur at much larger radius from the black hole than considered in this work.

¹We must correct for cosmology to work in terms of quantities at the emission site.



(8.1)

Figure 8.1: Quasar 3C 279 in A.D. 1995, 2001 and 2007 shown in Panels 1, 2 and 3, respectively. [32]. For scale, 1 mas = 6.4 pc = $1.3 \cdot 10^5 M$.

8.2 Absorption and Emission Processes in 3C 279

8.2.1 Pair Production Opacity

We must understand where the opacity is high in order to understand where to focus on emission that may be observed. Consider a model soft photon distribution comprising blackbody and X-ray photons (isotropic within a cone) that emanate directly from the disk and scattered blackbody X-ray photons (isotropic at all z). The disk intensity may be given as

$$I_{\nu 0 \Omega_0} = \frac{2h\nu_0^3}{c^2 \left(e^{\frac{h\nu_0}{kT}} - 1 \right)} = 1.5 \cdot 10^{-5} \nu_{015}^3 \frac{1}{e^{1.5\nu_{015}} - 1} \text{ Wm}^{-2} \text{ Hz}^{-1} \text{ sr}^{-1} \quad (8.2)$$

(using the notation $X = X_n 10^n$ to conveniently define SI quantities). The threshold for absorption obtains at $\nu_{015} > 4.1 \cdot 10^5 E_9^{-1} z_{15}^2$. If $\nu_{015} < 10$ for the blackbody disk component, then disk absorption occurs for $z_{15} < 0.005 E_9^{1/2}$.

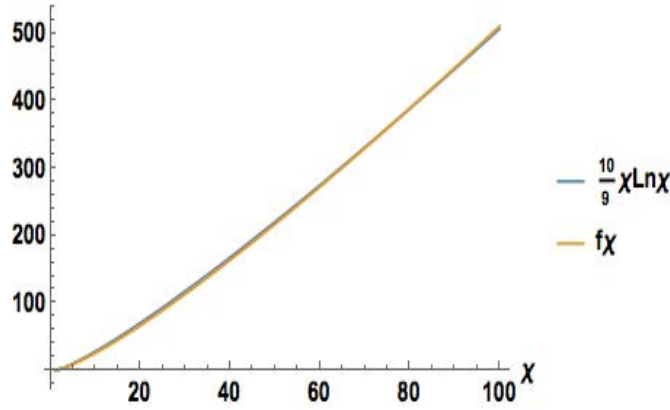
As for the X-ray disk component, assuming the fraction of disk intensity emitted as X-rays is $f = 0.1$, then

$$F_{\ln \nu_0}^X = \frac{2.5 \cdot 10^7 z_{15}^{-2} f}{\text{Log} 1000} = 3.6 \cdot 10^4 z_{15}^{-2} \text{ Wm}^{-2}, \quad \nu_{015} < 10 \quad (8.3)$$

and for $10\nu_{015} < 10^4$, $I_{\nu 0 \Omega_0} 1.8 \cdot 10^{-8} \nu_{015}^{-1} \text{ Wm}^{-2} \text{ Hz}^{-1} \text{ sr}^{-1}$.

Now consider the radiation field scattered by broad emission line (BEL) clouds. We assume here the isotropic component is

$$I_{\nu \Omega \text{Scattered}} = I_{\nu \Omega \text{Disk}} \left(\frac{1 - \mu_{0, \min}}{2} \right) f_s \quad (8.4)$$

Figure 8.2: The function f_χ and its analytic approximation.

where f_s is the (constant) fraction of photons scattering over an e-folding radius.

Turning back to the pair production opacity of Eq. 2.73, we assume $I_{\nu_0\Omega_0}$ is either 0 or constant over an outgoing cone of opening angle $\cos^{-1} \mu_0$ and define

$$f_\chi(\chi_{\max}) = \int_1^{\chi_{\max}} \frac{d\chi}{\chi^2} [(2\chi(\chi+1)-1) \ln(\chi^{1/2} + (\chi-1)^{1/2}) - \chi^{1/2}(\chi-1)^{1/2}], \quad (8.5)$$

where

$$\chi = \frac{3\pi\sigma_T}{\nu^2} \int_{\nu^{-1}}^{\infty} \frac{d\nu_0}{\nu_0^3} I_{\nu_0\Omega_0}(\nu_0) f_\chi\left(\frac{\nu\nu_0(1-\mu_{0\min})}{2}\right) \quad (8.6)$$

It turns out that $f_\chi(\chi_{\max}) \approx \frac{10}{9} \chi_{\max} \ln \chi_{\max}$ is a good analytic approximation, as shown in Figure 8.2. Putting it all together, we have an expression for the opacity

$$\chi = \frac{1.28 \cdot 10^{16}}{E_9^2} \int_{\frac{126}{E_9(1-\mu_{0,\min})}}^{\infty} \frac{d\nu_{015}}{\nu_{015}^3} f_\chi(0.0079 E_9 \nu_{015} (1 - \mu_{0\min})) \left(\frac{I_{\nu_0\Omega_0}(\nu_{015})}{1 \text{ W m}^{-2} \text{ Hz}^{-1} \text{ sr}^{-1}} \right) \text{ P m}^{-1} \quad (8.7)$$

The optical depth is plotted in Figure 8.2.1 versus altitude z and scattered photon energy.

Now that we have a picture of the pair production opacity distribution in a model JAB system, consider two following two scenarios to explain the gamma radiation emission observed in 3C 279:

8.2.2 Inverse Compton Scenario

It is commonly assumed that the high energy hump in an FSRQ spectrum is due to external inverse Compton scattering, e.g., this scenario is well studied in the case of the Crab Nebula, which is relatively free of hadrons. Gamma rays in the frame of the system that have energies $E_\gamma \lesssim 100$ MeV are then Doppler boosted to the up to 100 GeV energies observed. The electrons responsible for upscattering VHE photons are energetic enough that the Klein-Nishina limit may obtain for sufficiently small scattering angle. The cross section for pair production from photons from Section

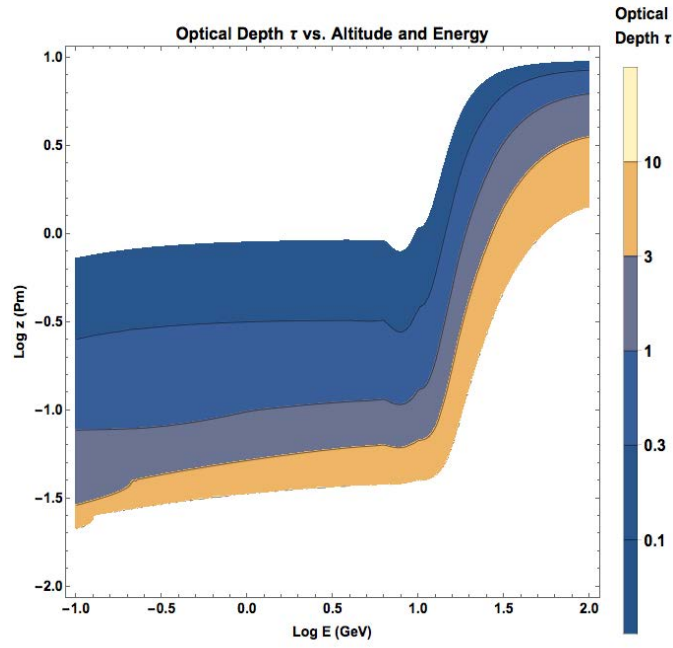


Figure 8.3: Optical depth τ decreases rapidly with altitude away from the disk and slowly increases as a function of scattered photon energy until $0.8 \text{ GeV} \lesssim E \lesssim 1.4 \text{ GeV}$, in which energy band, the variation of τ with energy is faster than that with distance. At higher scattered energies, E , the medium becomes optically thick above $7 \cdot 10^{14} \text{ m}$.

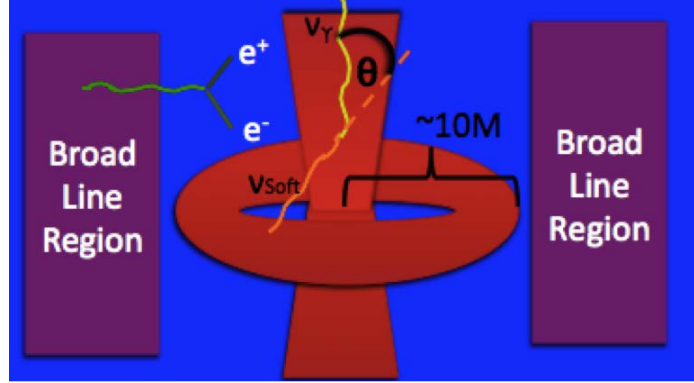


Figure 8.4: Soft photons from small cylindrical radii (the disk) are more likely to interact with longitudinally moving jet leptons than photons isotropically approaching from far out (broad line regions) since their small angle gives them a higher threshold for pair production.

2.3.4 implies a threshold for soft photon energy based on scattering angle θ

$$h\nu_{\text{soft}} \geq \frac{m_e c^2}{h\nu_\gamma(1 - \cos \theta)}, \quad (8.8)$$

where θ is given in Figure 8.2.2.

Following Pian et al. [46], it is useful to give a typical example of two soft photon sources to get a sense of the energetics involved in the inverse Compton scenario. The first source is a small cone of soft photons comprised of a blackbody component with temperature $\Theta \sim 3.1 \cdot 10^4 \text{K}$ and an X-ray component with $L_X/L_{\text{UV}} \sim 0.01$, where $\nu F_\nu \sim$ is constant for $10^{16} - 10^{19} \text{ Hz}$. This component comes directly from the disk ($R \sim 2.5 \cdot 10^{13} \text{ m}$). The second source is reprocessed radiation isotropic in a larger cone of solid angle $\Delta\Omega = \frac{\pi R^2}{z^2}$. The intensity of scattered radiation is then

$$I_{\nu\Omega, \text{Scattered}} = f \cdot I_{\nu\Omega, \text{Disk}} \frac{\Delta\Omega}{4\pi}, \quad (8.9)$$

where $f \sim 0.01$.

8.2.3 Synchrotron Scenario

A radical alternative to the inverse Compton scenario to produce $\gtrsim 100 \text{ MeV}$ gamma rays seen by *Fermi* is the synchrotron scenario. This scenario allows the emission to come from close to the black hole, as implied for rapid variability, but outside the gammasphere so that the gamma rays escape. The synchrotron radiating electrons will also emit inverse Compton radiation, which photons may not be able to escape at the same radius as their synchrotron counterpart. It also allows for the emission to originate from highly magnetized regions, consistent with the electromagnetically dominated simulation of this work. In a highly magnetized region, the inverse Compton scenario

has far greater gamma ray flux than optical synchrotron flux, which can serve as an observational constraint.

We have already calculated synchrotron radiation from the $\sim 10^{44}$ erg/s jet M87, and can compute this for it for the more powerful 10^{47} erg/s jet of 3C. Scaling from M87, with an electromagnetic luminosity 10^{-3} as large and a BH mass is 7x as great 3C 279, we infer $\Phi_H \sim 4 \cdot 10^{26}$ Wb. For ~ 300 MeV photons, the gammasphere (where optical depth $\tau \sim \mathcal{O}(1)$ in Figure 8.2.1) is at $r \sim 2 \cdot 10^{14}$ m $\approx 100M$, where the magnetic field is around 0.1 T. Then ~ 4 TeV electrons would radiate typical synchrotron gamma rays seen by *Fermi*. These electrons, with $\gamma \sim 8 \cdot 10^6$, would inverse Compton scatter the blackbody disk photons of peak frequency of a few PHz to 100 TeV energies, which scattered photons would quickly be absorbed by pair production. Such energetic photons build up the pair content of the jet to make the particle density necessary to explain the radio emission at large radius. The synchrotron cooling time of these electrons is $\sim 100 \mu\text{s}$, comparable to the acceleration time $eE/(\gamma mc)$. As these time scales are much shorter than the variability time scale, they impose no constraint on the observed variation timescale, which is determined by relativistic beaming and the extent of the emitting region.

8.3 3C 279 Gamma Ray Models

A simple model to consider is an isotropic soft photon field with electrons scattering in the Thompson limit off this field. Motivated by the inverse Compton emissivity prescription of Chapter 5, assume

$$j_{\text{IC}} \sim \mathcal{D}^4 \tilde{P}_e. \quad (8.10)$$

Figure 8.3 shows light curves generated from this model. The inverse Compton α -model is more consistent with a steady build-up and discharge of energy. The inverse Compton j^2 -model is episodic: the overall slow variation of this prescription on time scales of 10s of M (where $M \approx 5,000$ s for 3C 279) suggests the system may have been viewed mainly in “quiescent”² stages, punctuated by a couple of flares. However, there are some highly variable portions of the simulated light curves that suggest there could be comparable variability of synthetic and real observation if resolved beyond the $2M$ simulation temporal resolution limit and at small viewing angle. When considering emission regions further from the black hole, e.g., outside the inner 15% of the simulation ($|z| > 105M$) as in Figure 8.3, the intervals of high variability appear to be spread out more evenly throughout the light curve.

²Quiescent by simulation standards is wholly different than by astrophysical standards.

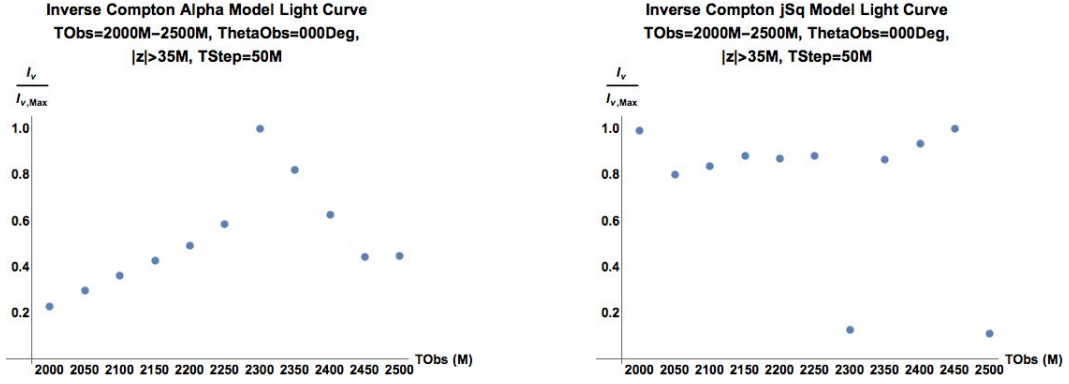


Figure 8.5: Simulated inverse Compton light curve for time series $T_{Obs} = 2000M, 2050M, 2100M, \dots, 2500M$ with only light from $|z| > 70M$ for the α -model (left) and j^2 model (right). Both models exhibit discernibly high variability around $2300M$, whereas only the j^2 model is highly variable around $2450M$.

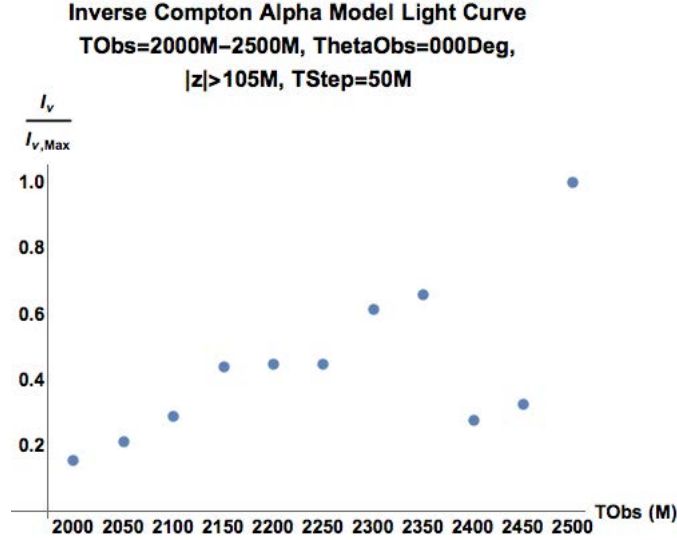


Figure 8.6: Simulated inverse Compton light curve for time series $T_{Obs} = 2000M, 2050M, 2100M, \dots, 2500M$ for the α -model with only light from $|z| > 210M$. This model is highly variable between $2300M$ and $2500M$.

We next adopt the synchrotron emissiity

$$j_{Sync} = \mathcal{D}^2 \tilde{P}_e B_e^{3/2}. \quad (8.11)$$

and consider the variability in Figure 8.3.

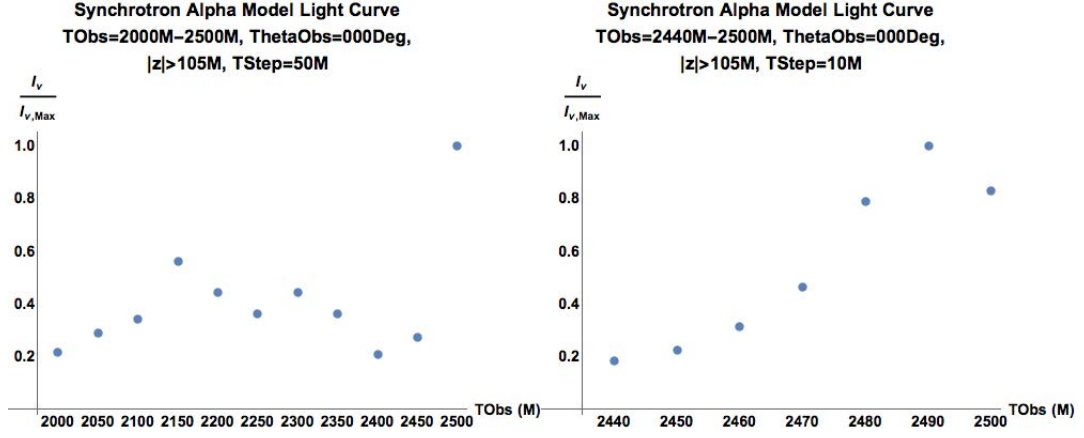


Figure 8.7: Simulated synchrotron light curve for time series $T_{\text{Obs}} = 2000M, 2050M, 2100M, \dots, 2500M$ (left panel) for α model with only light from $|z| > 210M$. This model is highly variable between $2300M$ and $2500M$. For the right panel, the interval $2440M$ - $2500M$ is resolved in $10M$ timesteps.

This prescription uses particle acceleration from the α -model like the first inverse Compton scenario explored, but the factor $B_e^{1.5}$ appears to have made the model less variable near $2300M$ and more variable near $2450M$. The extra factor seems to make this model slightly more variable overall.

A somewhat more complicated paradigm to explore in the future is synchrotron self-Compton (SSC). SSC explanations have the advantage of non-linear system response to the input of source particles relative to external inverse Compton models, in which observed radiation only doubles in response to doubling the soft photon density.

8.4 Alternative Emission Mechanisms

Even if the synchrotron scenario above is correct, it cannot account for emission of gamma rays of energies $\gg 1$ GeV. These photon energies lie well above the radiation reaction limit. Alternative particle acceleration schemes must be devised to explain such emission from blazars— including some with minute-scale variability, suggesting the emission originates from close to the black hole. Protons are not subject to the same radiative losses as the much lighter electrons, but their acceleration is limited by photo-pair production, pion-proton production in their Coulomb field or collision with surrounding protons. Given the high radiation densities within blazars, the first process seems most promising, however, the other two also deserve some consideration.

A possibility for the origin of gamma ray synchrotron radiating electrons is photo-pair production

$$p + \gamma \rightarrow p + e^- + e^+ \quad (8.12)$$

In this synchrotron scenario, the Coulomb field of PeV protons scatters eV photons to produce TeV electron-positron pairs that synchrotron radiate GeV gamma rays.

If the highest energy particles in an AGN detected at $>>1$ GeV are hadrons, the gamma radiation may originate from photo-pion production leptonic secondary products

$$\begin{aligned} \gamma + p &\rightarrow p\pi^0, n\pi^+ \\ \pi^+ &\rightarrow \nu_\mu\mu^+ \rightarrow \nu_\mu\nu_\mu\nu_\mu e^+ \rightarrow \text{synchrotron radiation} \\ \pi^0 &\rightarrow \gamma\gamma \rightarrow 2(e^+ + e^-) \rightarrow \text{synchrotron radiation} \end{aligned} \quad (8.13)$$

that synchrotron radiate from strong magnetic fields. For example, the ZeV potential difference found in a powerful source like 3C 279 can lead to > 100 MeV pions needed to lead to gamma radiating products. This process could dominate the 3C 279 high-energy spectrum if inverse Compton radiation is greatly suppressed in the Klein-Nishina regime.

Chapter 9

Data Analysis

We have seen in the previous two chapters that the simulation used is a highly versatile tool for capturing aspects of different kinds of AGN jets. We shall see here that the simulation allows us to represent an *ensemble* of jets when sampled appropriately. Having used the simulation to produce a panoply of synthetic observations from various times, angles and frequencies, it is worth re-examining the simulation data to reinforce why we have seen what we have seen.

Plots of the variation of azimuthally averaged simulation $\rho, u_g, v_x, v_y, v_z, B_x, B_y$ and B_z with cylindrical radius s at various altitudes and times (Figures 9.1, 9.2, 9.3, and 9.4) reveal a stationary flow that is force-free at low altitudes ($|z| \leq 100M$) and gradually mass-loaded outside this radius. Since the regions near the black hole appear electromagnetically dominated, we infer electron/positron plasma is injected near the black hole magnetosphere (which injection is effected in the simulation by numerical density floors). The jet is collimated at higher altitudes largely by pressure support from the disk wind and partly by hoop stress by the increasing toroidal magnetic field component. Outside of the force-free region, entrainment through "funnel walls" of the jet becomes important.

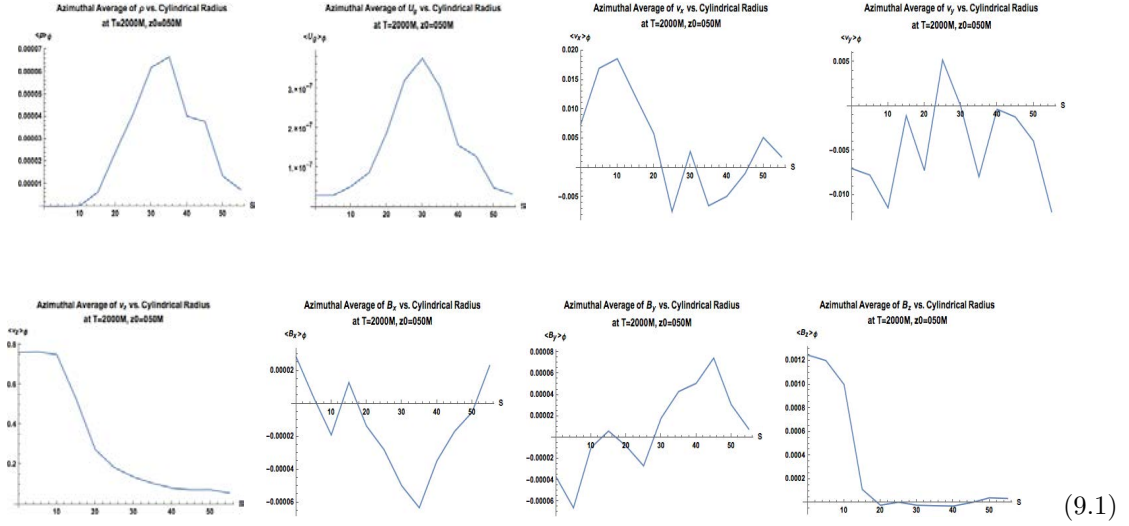


Figure 9.1: Variation of (from top left to bottom right) ρ , u_g , v_x , v_y , v_z , B_x , B_y and B_z with cylindrical radius s at simulation time $T = 2000M$ at height $z_0 = 50M$

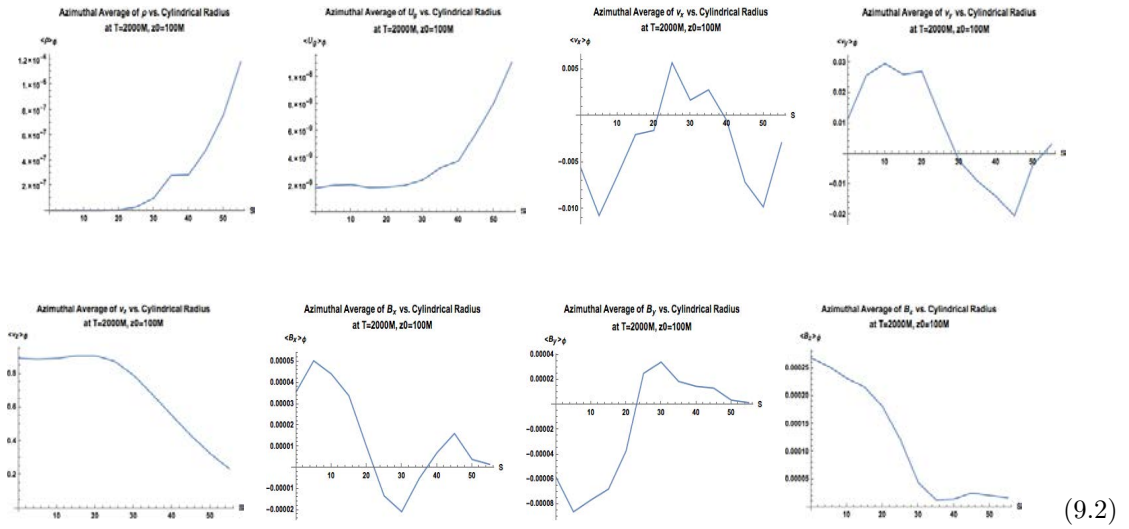


Figure 9.2: Variation of (from top left to bottom right) ρ , u_g , v_x , v_y , v_z , B_x , B_y and B_z with cylindrical radius s at simulation time $T = 2000M$ at height $z_0 = 100M$

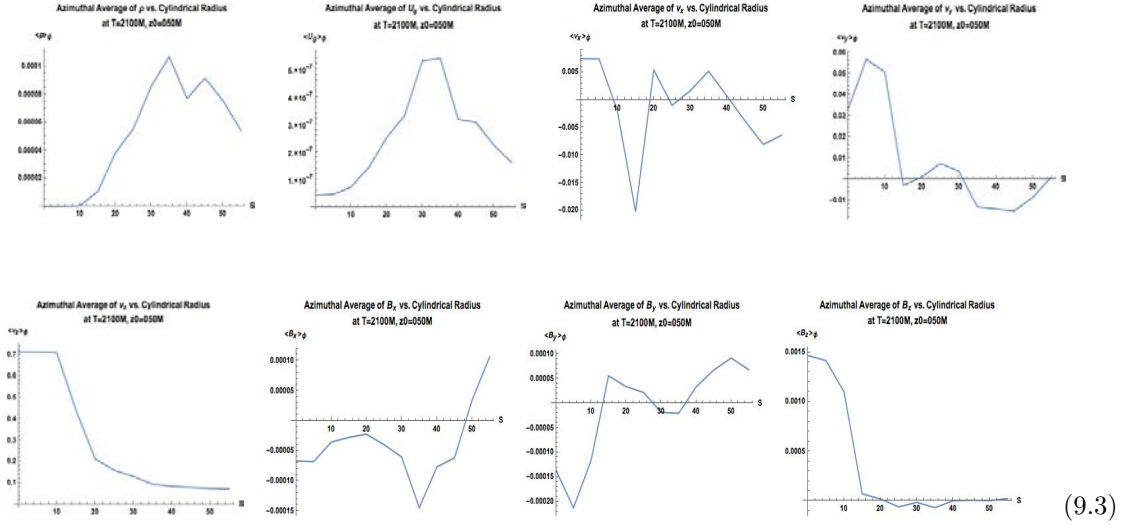


Figure 9.3: Variation of (from top left to bottom right) ρ , u_g , v_x , v_y , v_z , B_x , B_y and B_z with cylindrical radius s at simulation time $T = 2100M$ at height $z_0 = 050M$

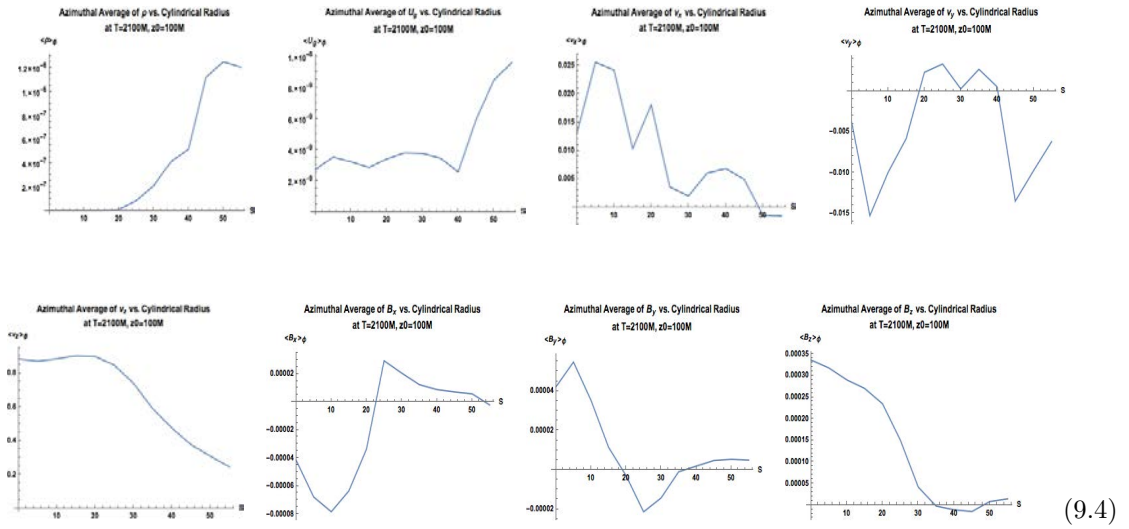


Figure 9.4: Variation of (from top left to bottom right) ρ , u_g , v_x , v_y , v_z , B_x , B_y and B_z with cylindrical radius s at simulation time $T = 2100M$ at height $z_0 = 100M$

9.1 Stationary Axisymmetric Model from Velocity and Magnetic Field Fits

As we have seen in Chapter 4, in a stationary axisymmetric model, analytic forms for jet variables such as \vec{B} , \vec{v} , \vec{E} , V , I , \vec{j} and Ω in the near-jet force-free regime can be derived from electromagnetic theory and the simulation. In this section, we attempt to investigate models where the fundamental quantities are \vec{B} and \vec{v} and we relax the self-similarity assumption. It is natural to model the electromagnetically dominated inner jet as powered by the Blandford-Znajek mechanism. In this setting, the quantities $V(\Phi)$, $I(\Phi)$ and $\Omega(\Phi)$ are constant on surfaces of constant flux Φ threading the black hole (measured outward from the axis). Ferraro's law for stationary axisymmetric MHD flows implies that \vec{B} field lines are equipotentials

$$B_z ds = -B_s dz = \frac{d\Phi}{ds} \quad (9.5)$$

Ampere's law gives

$$B_\phi = \frac{\mu_0 I}{2\pi s} \quad (9.6)$$

The electric field satisfies

$$E_s ds = E_z dz = -dV \quad (9.7)$$

$$E_\phi = 0 \quad (9.8)$$

In force-free MHD,

$$\vec{E} = -\vec{v} \times \vec{B} = \{v_z B_\phi - v_\phi B_z, v_s B_z - v_z B_s, v_\phi B_s - v_s B_\phi\} \quad (9.9)$$

Thus, we can compute Φ using

$$\begin{cases} \frac{d\Phi}{ds} = 2\pi s B_z \\ \frac{d\Phi}{dz} = -2\pi s B_s \end{cases} \quad (9.10)$$

Using

$$\frac{dV}{ds} = v_\phi B_z - B_\phi v_z = B_z \left(v_\phi - \frac{B_\phi v_z}{B_s} \right) = \frac{1}{2\pi s} \frac{d\Phi}{ds} \quad (9.11)$$

we can relate V to Φ with the differential equation

$$\frac{dV}{d\Phi} = \frac{1}{2\pi s} \left(v_\phi - \frac{B_\phi v_z}{B_s} \right) \quad (9.12)$$

This equation can be integrated numerically from the simulation for $V(\Phi)$.

Now take $z_0 = 50M$ as a reference altitude and use the azimuthally averaged quantities to incorporate the current density \vec{j} and total current I through a disk of cylindrical radius s in the

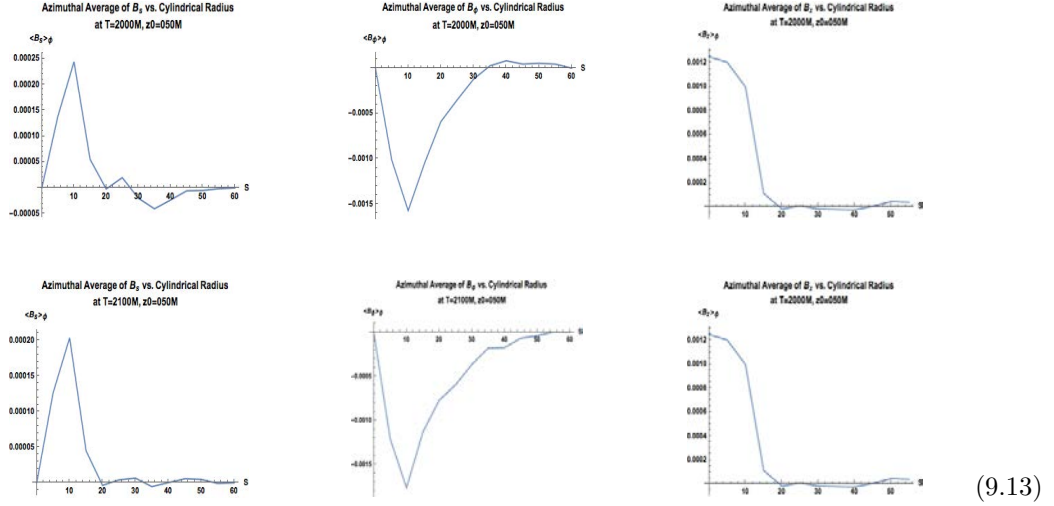


Figure 9.5: Variation of (from left to right) B_s , B_ϕ and B_z with cylindrical radius s at simulation time $T = 2000M$ (top) and $T = 2100M$ (bottom) at height $z_0 = 50M$.

axisymmetric model. To this end, it is convenient to transform \vec{B} from the above plots to cylindrical coordinates, as in the plots of B_s , B_ϕ and B_z in Figure 9.5. These are well-represented by the fitting forms for the code magnetic field in cylindrical coordinates

$$\langle B_s, B_\phi, B_z \rangle \sim \langle 5 \cdot 10^{-4} (s/15) e^{-(s/15)^6}, -4 \cdot 10^{-3} (s/15) e^{-(s/15)^2}, 1.4 \cdot 10^{-3} e^{-(s/15)^6} \rangle \quad (9.14)$$

The current setting up this toroidal field is along the longitudinal (jet) axis and given by Ampère's law to be

$$I = \frac{2\pi s B_\phi}{\mu_0}. \quad (9.15)$$

The magnetic flux through the horizon, or, almost equivalently, the magnetic flux through one hemisphere, is given in the simulation by $\Phi = 2\pi \int ds s B_z = 10^{26} \text{Wb}$.

Next for this semi-analytic model is the current density, given by

$$\vec{j} = \frac{1}{\mu_0} \vec{\nabla} \times \vec{B} \quad (9.16)$$

Using the following analytic forms

$$\langle v_s, v_\phi, v_z \rangle \sim \langle 7.0 \cdot 10^{-1} (s/18) e^{-(s/18)^2}, 7.5 \cdot 10^{-1} e^{-(s/18)^2}, \frac{B_s}{B_z} v_\phi \rangle, \quad (9.17)$$

based on the code velocity in cylindrical coordinates (see Figure 9.6) electric field \vec{E} , fieldline angular

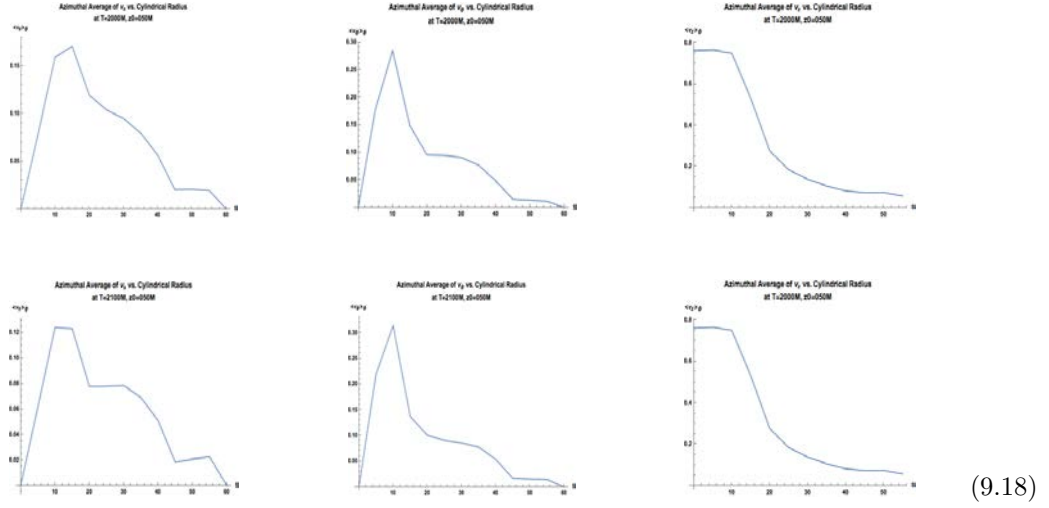


Figure 9.6: Variation of (from left to right) v_s , v_ϕ and v_z with cylindrical radius s at simulation time $T = 2000M$ (top) and $T = 2100M$ (bottom) at height $z_0 = 50M$.

speed $\Omega = -\frac{E_s}{sB_z}$ and the dynamic quantities $F_{\text{EM}} = \frac{1}{\mu_0} \vec{E} \times \vec{B}$, $L_{\text{EM}} = 2\pi \int ds F_{\text{EM}} s$ and $G_{\text{EM}} = \frac{E_{\text{EM}}}{\Omega}$ can be included in the model.

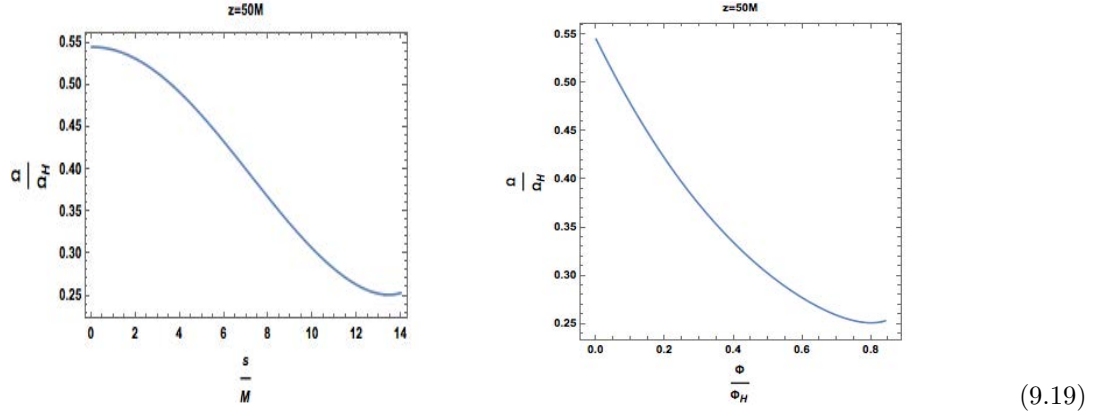


Figure 9.7: Fieldline angular speed at $z_0 = 50M$ as a function of cylindrical radius (left). On right panel, the angular velocity is plotted as an implicit function of the fraction of total flux enclosed by a disk of radius s .

Because the simulation's numerical density floors are put in by hand, it is natural to take \vec{B} and \vec{v} as fundamental quantities. In this model, the fieldline angular velocity at the z -axis is about twice the angular velocity at cylindrical radius $=M$ (see Figure 9.7), in accordance with the prediction for

Blandford-Znajek jets. This exercise has shown we can make useful analytic forms from a small set of assumptions by “observing” the simulation without invoking self-similarity.

9.2 Individual Source Statistics

9.2.1 Radio versus Gamma-Ray Light Curves

After accounting for full radiation transport in the simulations, we will produce synthetic light curves and time-dependent spectra to compare with observations. Peaks in observed radio AGN intensity tend to lag peaks in gamma ray intensity. The modest number (~ 2000) of AGN observed in both radio and gamma ray wavelength admits large uncertainties in estimated lag duration. The “Observing Jet Simulations” approach can generate a virtually unlimited sample size by varying azimuthal direction.

9.2.2 Stationarity

A stationary quantity is one whose time average equals its azimuthal average

$$\langle \rangle_t = \langle \rangle_\phi$$

Tests of stationarity help us to determine whether JAB system features are time-independent or disrupted by global instabilities. At observer times $T_{\text{Obs}} = 2000M, 2100M$, the simulation appears free of transients, and temporal averages of output state variables at altitude $z = 100M$, azimuth $\phi = 0$ and various cylindrical radii s are shown in Figure 9.8.

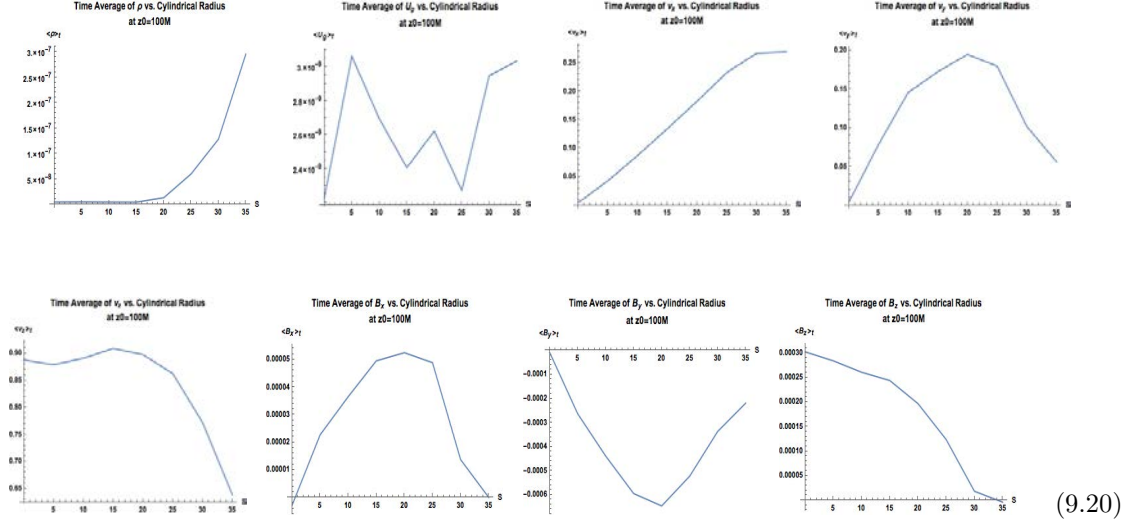


Figure 9.8: Variation of (from top left to bottom right) ρ , u_g , v_x , v_y , v_z , B_x , B_y and B_z with cylindrical radius s averaged over simulation times $T = 2000M$ and $T = 2100M$ at height $z_0 = 100M$ and azimuth $\phi = 0^\circ$. The cylindrical radius is cut off just before the minimum cylindrical radius $s_{\min} = 40M$ in the simulation region.

These values can be compared to azimuthal averages in the next section to verify stationarity.

9.3 Survey Statistics

9.3.1 Azimuthal Variation and Averages

GRMHD simulations that are fully 3D can be used to simulate surveys of sources throughout the sky. We observe significant variation in observed intensity maps generated from the same emissivity prescription at the same inclination angle in Figure 9.9. We have used the azimuthal averages to construct an axisymmetric model relating jet voltage, current and field line angular velocity to flux.

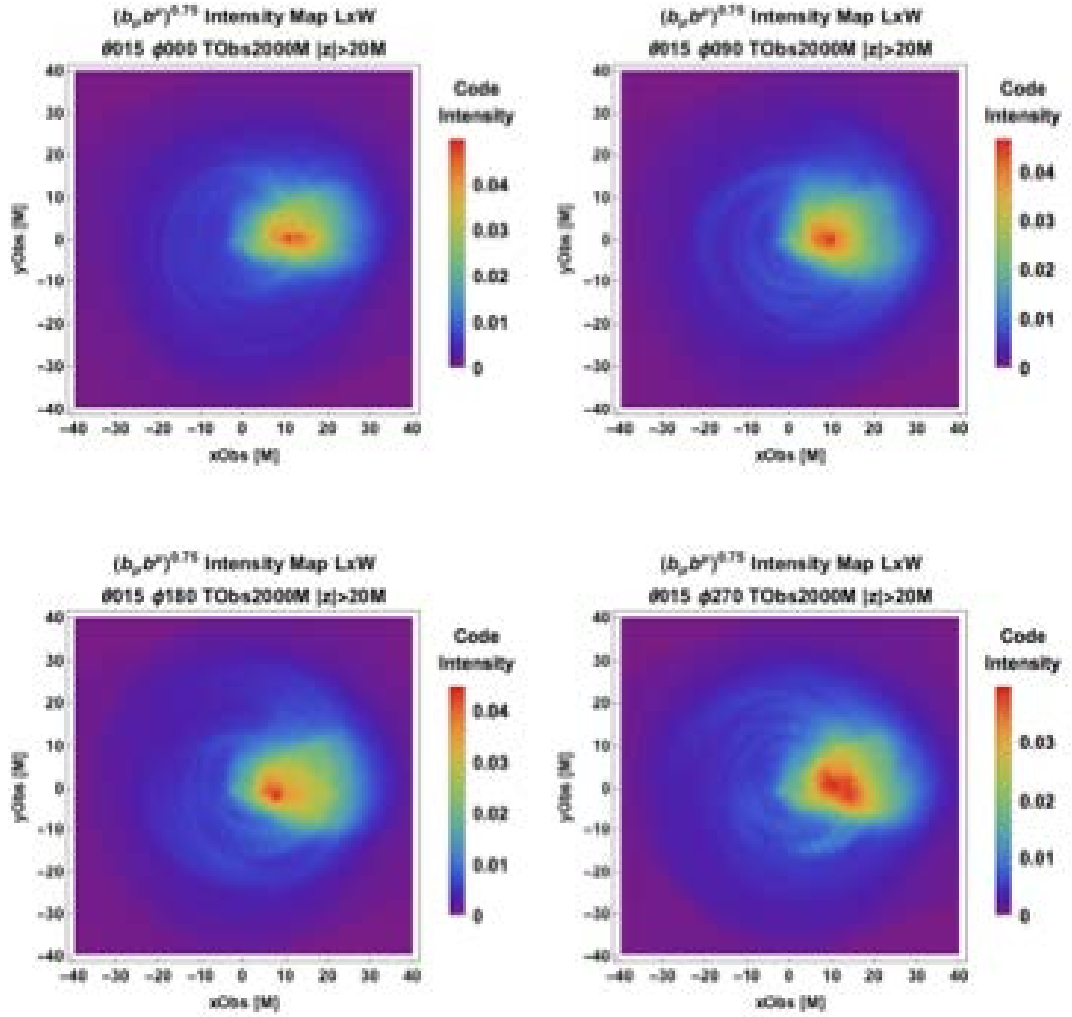


Figure 9.9: Image maps generated from emissivity function $j \sim (b_\mu b^\mu)^{0.75}$ with $|z| > 20$ viewed at (clockwise from top left) $\phi_{\text{Obs}} = 0^\circ, 90^\circ, 180^\circ$ and 270° .

9.3.2 Polar Variation

We see the polar variation from 15° - 20° of the observer plane intensity for $j \sim (b^2)^{3/4}$ in Figure 9.11

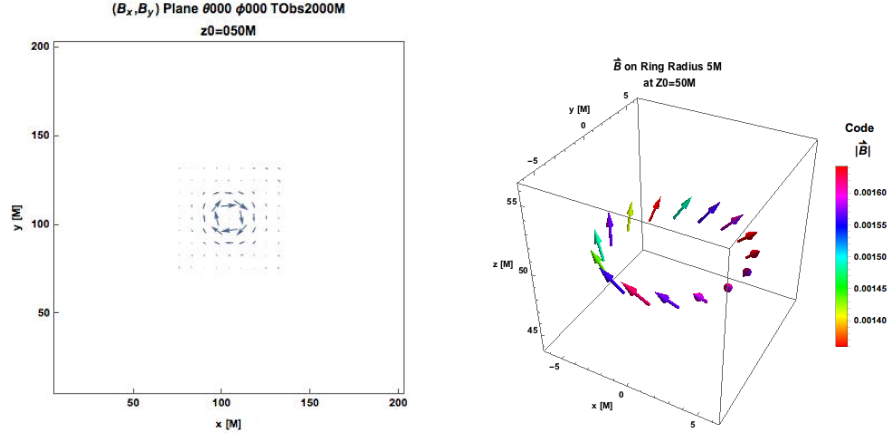


Figure 9.10: Component of \vec{B} on $z = 50M$ (left panel). Magnetic field 3D vectors at 16 points on a ring in the $z = 50M$ plane centered at $(0, 0, 50M)$ (right panel).

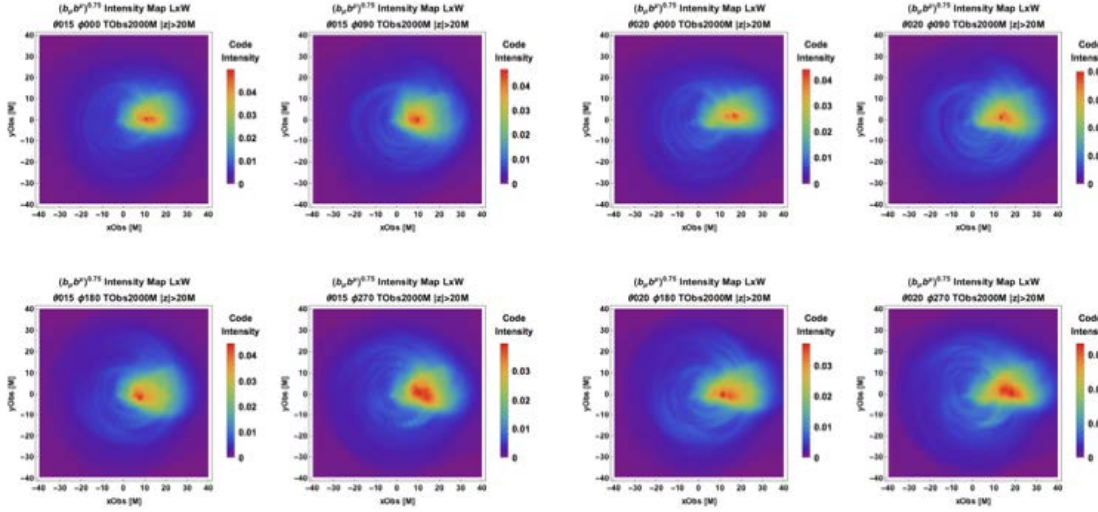


Figure 9.11: Image maps generated from emissivity function $j \sim (b_\mu b^\mu)^{0.75}$ with $|z| > 20$ viewed at (clockwise from top left) $\phi_{\text{Obs}} = 0^\circ, 90^\circ, 180^\circ$ and 270° and viewing angle 15° (left panel) and 20° (right panel).

9.3.3 Flux Limited Samples

The question of how many orientations to consider for “Observing Jet Simulations” may be linked to how many AGN are visible in a flux-limited sample. AGN have luminosity between 10^8 and $10^{14} L_\odot$ (and one can assume 10% host jets).

Let the bolometric luminosity function $n(L)dL$ give the number of sources per unit volume with

luminosity between L and $L + dL$. Flux and luminosity are related by

$$S_\nu = \frac{L_\nu}{4\pi r^2}.$$

Surveys are flux limited. The number of sources with flux greater than S_{\min} equals the sum over distance of the number of sources with luminosity $L_{S_{\min}}(r) = 4\pi r^2 S_{\min}$ at distance r . This can be computed as

$$\begin{aligned} N(S > S_{\min}) &= \int_0^\infty 4\pi r^2 \left(\int_{4\pi r^2 S_{\min}}^\infty n(L) dL \right) dr \\ &= \int_0^\infty n(L) \left(\int_0^{\sqrt{\frac{L}{4\pi S_{\min}}}} 4\pi r^2 dr \right) dL \end{aligned}$$

Assuming a distribution of standard candles $n = n_0 \delta(L - L_0)$,

$$\begin{aligned} N(S > S_{\min}) &= \int_0^\infty n_0 \delta(L - L_0) \left(4\pi \int_0^{\sqrt{\frac{L}{4\pi S_{\min}}}} r^2 dr \right) dL \\ &= n_0 \frac{4\pi}{3} \left(\frac{L_0}{4\pi S_{\min}} \right)^{3/2}. \end{aligned}$$

An important issue not addressed by our simulations and routines is the cosmological evolution, which must be taken into account for future comparisons to more distant sources than 3C 279.

Chapter 10

Future Directions

Our investigation of jet simulations with application to M87 and 3C 279 have well prepared us to apply the pipeline to compare sources that may combine various properties of each of the aforementioned sources, as well as to account for idiosyncratic features such as spectral bumps. Optical wavelength observations quickly come to mind as an intermediate regime between the prototypical radio source M87 and the prototypical gamma ray source 3C 279. Some future directions are outlined below.

10.1 Observing Accretion Disk Simulations

Disks of accreting matter may be found orbiting gravitating bodies from planetary to stellar to galactic scales throughout the observable universe. Located at our Galactic Center, Sagittarius A* is a prime target of observation due to its proximity. Disk emission from Sgr A* has been observed and modeled throughout the electromagnetic spectrum: the X-ray bremsstrahlung emission originates from hot gas at large radii according to [42]; the inverse Compton component is near the horizon [40]; the cyclo-synchrotron sub-mm emission originates close to the black hole [53]. However, semi-analytical models of the disk, e.g., [41] and GRMHD simulations of Sgr A* to date fall short of a unifying framework of particle acceleration, emission and radiative transfer as has been done with jets in this work on “observing” simulations of MB09 and MTB12.

10.2 Incorporating General Relativity into Radiative Transfer

For Kerr (rotating) black holes such as M87, the inner and outer horizons occur at the singularities of the line element induced by the Kerr metric

$$ds^2 = - \left(1 - \frac{r_S}{\rho^2} r \right) c^2 dt^2 - \frac{a r_S^2 \sin^2 \theta}{\rho^2} r c dt d\phi + \frac{\rho^2}{r^2 - r r_S + \frac{a^2 r_S^2}{4}} dr^2 + \rho^2 d\theta^2 + \left(r^2 + \frac{a^2 r_S^2}{4} + \frac{r r_S a^2 \sin^2 \theta}{\rho^2} r \right) \sin^2 \theta d\phi^2 \quad (10.1)$$

, where $\rho^2 = r^2 + \frac{a^2 r_S^2}{4} \cos^2 \theta$, i.e., at $r = r_{\pm} = \frac{(1 \pm \sqrt{1 - a^2}) r_S}{2}$. Thus, for M87

$$0.5 r_{S, M87} < r_+ < \left(\frac{1}{2} + \sqrt{\frac{1}{4} - \frac{(.2)^2}{4}} \right) r_{S, M87} = 0.99 r_{S, M87} \quad (10.2)$$

The time required for light to traverse apparent width of M87 is $3.20 \times 10^4 \text{s} = 8.8 \text{h}$, and the light crossing time for the M87 Schwarzschild radius is $(6.53 \times 10^4 \pm 3.80 \times 10^3) \text{s} = (18.1 \pm 1.5) \text{h}$.

In addition to the distortion of the event horizon, the Kerr metric makes ray tracing more challenging than adding contributions from parallel planes up to a fixed observer plane. The “Observing Jet Simulations” integration routines must now be modified to solve for the locus of points on curved geodesic lines of sight corresponding to the same observer time.

10.3 Mrk 421 - Beamed Version of M87

Markarian (Mrk) 421 (R.A. $11^{\text{h}}4^{\text{m}}$, decl. $38^{\circ}12'$, $z = 0.03$) is a giant elliptical galaxy and BL Lac blazar whose emission is greatly beamed due to its small viewing angle. It has exhibited optical, X-ray and gamma ray variability on minute timescales, and has also exhibited dramatic flares in recent years, most recently in 2013 [45]. Because of gaps in the observation of Mrk 421 in its low-activity state and—due to lack of detector sensitivity before *Fermi*—lack of analysis of the gamma rays portion of its spectrum, there remains great uncertainty in the emission mechanisms that power this source [1] at observed TeV energies. Thus, Mrk 421 is a prime target for the modeling of multi-wavelength emission using jet simulations.

10.4 Observing Jet Simulations To-Do List

The following list provides immediate extensions of this dissertation:

- Incorporating circular polarization into the polarized radiative transfer equations: Circular polarization allows us to compute the phase difference accumulated due to Faraday pulsation, which, along with Faraday rotation, can help us distinguish electron-positron plasma from ionic plasma.
- Increasing the temporal resolution of intensity map movies from tens to hundreds of frames to better track moving features, especially corkscrew instabilities and superluminal bulk flows
- Enhancing the significance of the statistical analysis by including more jet viewing angles to simulate more source types (e.g., Seyfert galaxies versus blazars), and including more azimuthal angles to simulate larger surveys
- Using a larger computational volume to facilitate acceleration of jet bulk flows to ultra-relativistic speeds
- Comparing observations across the electromagnetic spectrum with simulations
- Cross-correlating light curves at different frequencies

10.5 What's Next?

As of this writing, first fringes of Sgr A* and M87 have been detected at 1.3 mm by the EHT, with sub-mm observations to come [20]. Negotiations are being finalized to construct the CTA in Chile and the Canary Islands, while existing gamma ray observatories such as *Fermi* amass more and more exposure time. Jet simulations are expanding to the outer portions of jets to shed light on the Faranohoff-Riley dichotomy while increasing resolution to determine the morphology of jet instabilities [54]. So what to expect next?

The agreement between simulation and observation in this work, admittedly, are impressionistic at best. However, upon reflection, this outcome should have been expected. These preliminary prescriptions used for this work were used because of their convenient physical interpretations, for example, equipartition or Newtonian shear. Future prescriptions will almost undoubtedly be more messy, combining these and other fundamental prescriptions. Though in this work, several observational signatures such as collimation, Doppler boosting, bulk flow motion and differential brightening of the jet edges have been observed, many more have not been. Superluminal motion, realistic jet dimensions, edge brightening and overall qualitative appearance have all been wanting. However, the simulation we started with was rather generic, and was not fine-tuned to have high Lorentz factors or artificially perturbed by instabilities. However, here the development of a robust

pipeline has been laid out in detail, and the choices displayed in the models here can now be readily optimized. It is also worth stating that a significant– though unintended– benefit of this work is an efficient method for generating aesthetic images of relativistic jets. I hope you have enjoyed observing this process unfold much as I enjoy “observing” jet simulations.

Appendix A

Checks of Observing Jet Simulations Computational Pipeline

The robustness of our methodology of observing simulation to reverse engineer observations can be checked by increasing spatiotemporal resolution or modulating the azimuthal observer angle to ascertain ranges of resolution and angle values in which images remain stable. The integration routine, essential to projecting a 3D-simulation onto a 2D-observer plane, can be checked using mock data with simple geometric shapes.

A.1 Projection of Doppler Factor Test

For Hubble expansion, the spatial part of four velocity $u^\mu = \gamma(c, \vec{v})$ is proportional to the displacement from a center of expansion. Taking $\gamma v = cr/r_0$, we have

$$\gamma\beta = u_r = \frac{r}{r_0}.$$

For an observer plane a distance z from the center of expansion, we may evaluate the Doppler factor for rays incident on the plane at impact parameter b and inclination $\theta = \tan^{-1}(b/z) = \cos^{-1}(z/r)$, where $r = \sqrt{b^2 + z^2}$. Using, $u_r^2 + 1 = \gamma^2$, the Doppler factor

$$D = \frac{1}{\gamma(1 - \beta \cos \theta)}$$

simplifies to

$$D = \frac{r_0}{\sqrt{r_0^2 + b^2 + z^2} - z}.$$

In the figures below, we show the radial profile of the projection of spherically symmetric emissivity functions with Doppler factor of the Hubble expansion velocity field.

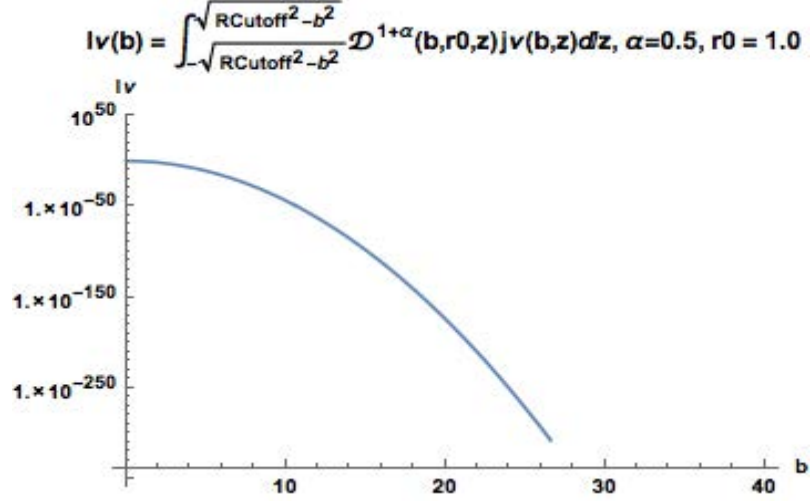


Figure A.1: Projection of spherical Gaussian emissivity with Hubble expansion velocity field

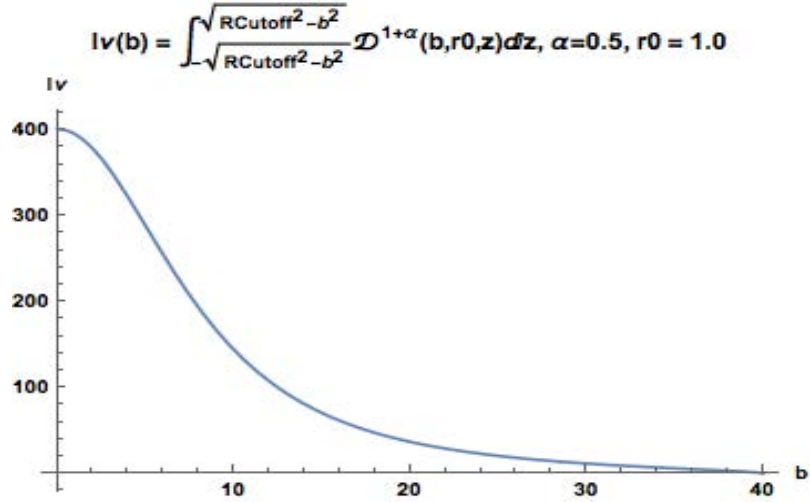


Figure A.2: Projection of constant emissivity with Hubble expansion velocity field

The analytic profiles obtained enable us to check the ObservingJetSimulations routines for

integration along a line of sight

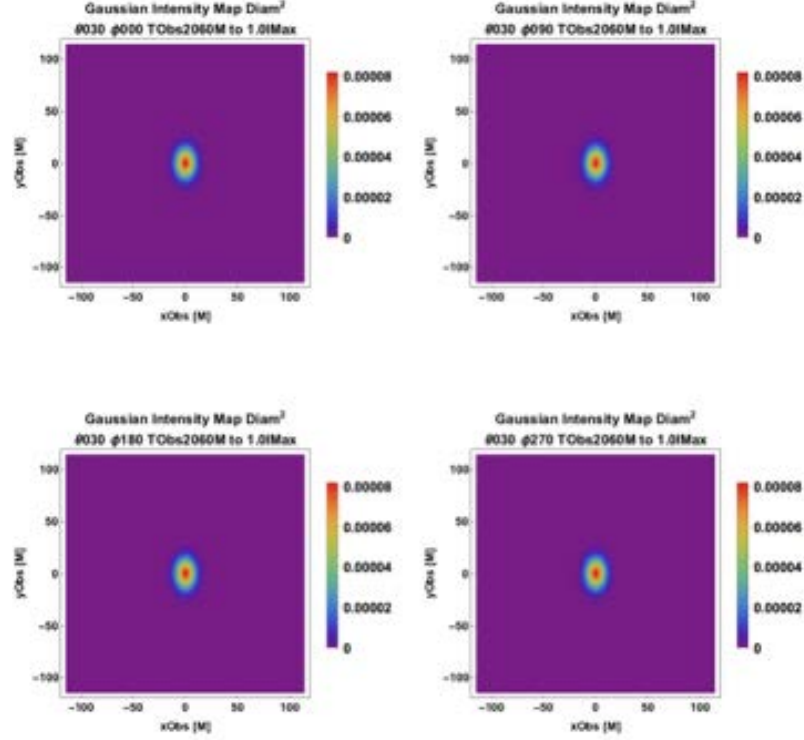
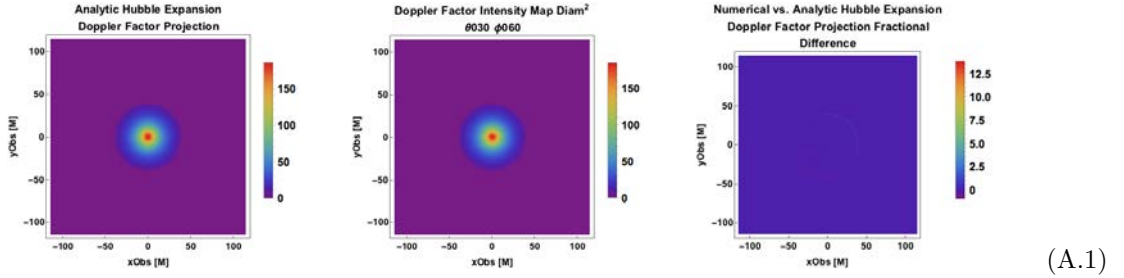


Figure A.3: 3D Gaussian density plots constructed from replacing Ug and bSq in DataList with Gaussian3D, setting $j \sim \sqrt{U_g b_\mu b^\mu}$ and projecting from four orientations of the observer plane.



(A.1)

Figure A.4: Projection of Gaussian emissivity with Hubble expansion velocity field from integrating analytic form in Mathematica (left), from simulation with $j \sim \rho \sim \text{Gaussian}$ and Hubble expansion velocity field with C++ routines (middle) and the difference between them (right).

Appendix B

UNIX and Python Guides for Observing Jet Simulations

Documentation providing UNIX programming background and commonly performed UNIX tasks for this project is provided below.

B.1 UNIX Guide for Observing Jet Simulations

What is UNIX?

- UNIX Structure

- UNIX Tips

- UNIX Help

Frequently Performed UNIX Operations for Observing Jets Project

- Remotely Accessing KIPAC Computer ki-ls via Secure Shell

- Change Owner or Moderator

- Secure Copy

- Editing File w./Midnight Commander and Submitting Job Using Bsub

Using UNIX on a Cluster

- Running Jobs in Parallel on a Supercomputer

UNIX Guide References

%What is UNIX

UNIX is a primitive operating system (collection of software managing computer hardware) developed at AT&T's Bell Labs in 1969. For historical background on the creation and development of the UNIX-based operating system Linux, see Linux vs. Windows (B) case. UNIX is programmed in the C language can be operated by a user using a shell. To get acquainted with UNIX syntax, see Table 1 for some frequently used commands (in *italics*) and UNIX output structure

Table 1: Common UNIX commands

Command	Purpose
<i>pwd</i>	Show the "present working directory", or current directory.
<i>ls</i>	List directory contents.
<i>mkdir</i> <i>Directory1</i>	Make directory "Directory1".
<i>rmdir</i> <i>Directory1</i>	Remove directory "Directory1".

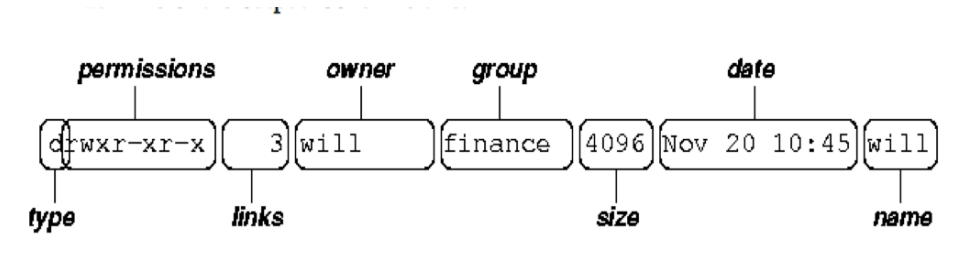


Figure B.1: Syntax for UNIX commands.

%UNIX Structure

A UNIX operating system is a filesystem containing directories, devices (block-oriented or data-oriented), links and ordinary files. The filesystem is conveniently graphically represented as a tree starting with the root directory "/" (see Fig. 2).

Figure 2. (cf. [3]).

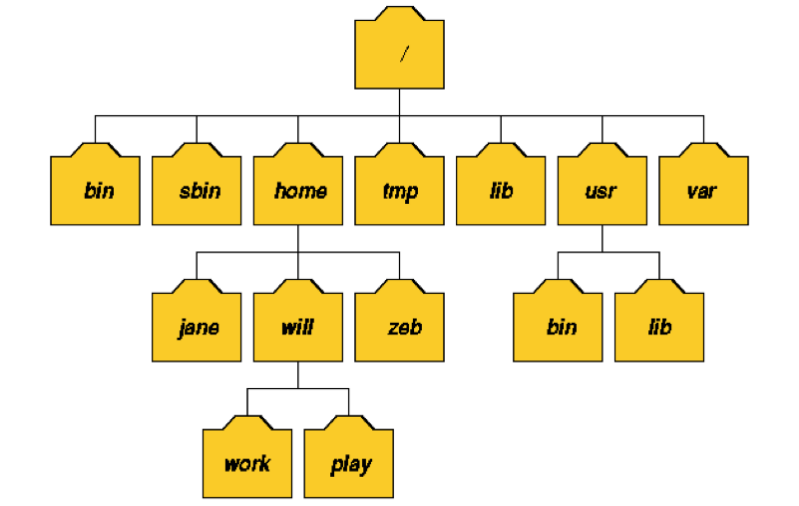


Figure B.2: Tree diagram of the file structure for a UNIX operating system.

To navigate the UNIX filesystem, the following commands in the table below are useful

Table 1. Moving around filesystem (cf. [4])

Table 2: More UNIX commands

Command	Function or Example
<code>cd</code>	Change current directory to your HOME directory.
<code>cd /usr/STRIM100</code>	Change current directory to /usr/STRIM100.
<code>cd bob</code>	Change the current directory to the user bob's home directory (if you have permission).

%UNIX Tips

If you forget your current username, use the command `whoami`

Richards-MacBook-Air-3:Documents richardanantuahome\$ `whoami` richardanantuahome

-bash-4.1\$ `whoami` ranantua

UNIX differs from most operating systems by: not including extensions in ordinary file names

Use underscores instead of spaces in file names

An asterisk (*) denotes a wildcard, or placeholder in a larger phrase. For example, to securely copy (see %To Securely Copy) all files beginning with “ranantua@corn.stanford.edu:rt/math/Shcherbakov”, perform the commands below:

dhcpvisitor220136:math richardanantua\$ `scp ranantua@corn.stanford.edu:rt/math/Shcherbakov*`

Password :

Shcherbakov Penna McKinney 2012.nb 100% 3689KB 3.6MB/s 00:01

%UNIX Help

To look at the UNIX manual (documentation center) for a command, type the blue text after the command line prompt:

Richards-MacBook-Air-3:~ richardanantuahome\$ *man command*

(see To Change Owner Section for example of output of *man* for the command *chown*)

Frequently Performed UNIX Operations for Observing Jets Project

% Remotely Accessing KIPAC Computer ki – ls via Secure Shell

Follow the prompts and commands below to access KIPAC computer ki-ls via secure shell

Richards-MacBook-Air-3:~ richardanantuahome\$ *ssh -X ranantua@ki-ls.slac.stanford.edu*

% To Change Owner

To change the owner of `/var/run/httpd.pid` to 'root' (the standard name for the Superuser).

\$ *chown root/var/run/httpd.pid*

Richards-MacBook-Air-3:~ richardanantuahome\$ *help -s cp*

-bash: help: no help topics match 'cp'. Try 'help help' or 'man -k cp' or 'info cp'.

Richards-MacBook-Air-3:~ richardanantuahome\$ *man chown*

CHOWN(8) BSD System Manager's Manual CHOWN(8)

NAME chown – change file owner and group

SYNOPSIS chown [-fhv] [-R [-H — -L — -P]] owner[:group] file ... chown [-fhv] [-R [-H — -L — -P]] :group file ...

DESCRIPTION The chown utility changes the user ID and/or the group ID of the specified files. Symbolic links named by arguments are silently left unchanged unless -h is used.

The options are as follows:

-f Don't report any failure to change file owner or group, nor modify the exit status to reflect such failures.

-H If the -R option is specified, symbolic links on the command line are followed. (Symbolic links encountered in the tree traversal are not followed.) -h If the file is a symbolic link, change the user ID and/or the group ID of the link itself.

-L If the -R option is specified, all symbolic links are followed.

-P If the -R option is specified, no symbolic links are followed. Instead, the user and/or group

ID of the link itself are modified. This is the default. Use `-h` to change the user ID and/or the group of symbolic links.

`-R` Change the user ID and/or the group ID for the file hierarchies rooted in the files instead of just the files themselves.

`-v` Cause `chown` to be verbose, showing files as the owner is modified.

The `-H`, `-L` and `-P` options are ignored unless the `-R` option is specified. In addition, these options override each other and the command's actions are determined by the last one specified.

The owner and group operands are both optional; however, at least one must be specified. If the group operand is specified, it must be preceded by a colon (":") character.

The owner may be either a numeric user ID or a user name. If a user name is also a numeric user ID, the operand is used as a user name. The group may be either a numeric group ID or a group name. If a group name is also a numeric group ID, the operand is used as a group name.

For obvious security reasons, the ownership of a file may only be altered by a super-user. Similarly, only a member of a group can change a file's group ID to that group.

DIAGNOSTICS The `chown` utility exits 0 on success, and !=0 if an error occurs.

COMPATIBILITY

Previous versions of the `chown` utility used the dot (".") character to distinguish the group name. This has been changed to be a colon (":") character, so that user and group names may contain the dot character.

On previous versions of this system, symbolic links did not have owners.

The `-v` option is non-standard and its use in scripts is not recommended.

LEGACY DESCRIPTION In legacy mode, the `-R` and `-RP` options do not change the user ID or the group ID of symbolic links.

SEE ALSO `chgrp(1)`, `find(1)`, `chown(2)`, `fts(3)`, `compat(5)`, `symlink(7)`

STANDARDS The `chown` utility is expected to be IEEE Std 1003.2 ("POSIX.2") compliant.

HISTORY A `chown` utility appeared in Version 1 AT&T UNIX.

BSD March 31, 1994 BSD

% To Secure Copy

Below is the syntax for secure copy (*scp*) [6]

```
scp[options]
username1@source_host : directory1 /filename1
username2@destination_host : directory2 /filename2
```

The location of the source file is specified by

username1@source_host : directory1 /filename1

, which includes the:

- Name of the account on the host computer (username1)
- Hostname of the computer on which the source file resides (source_host)
- Name of the directory containing the source file (directory1)
- Filename of the source file (filename1)

The location to which the source file will be copied is specified by

username2@source_host : directory2 /filename2

, which includes the:

- Name of the account on the host computer (username1)
- Hostname of the computer to which the source file will be copied (destination_host)
- Name of the directory to which the source file will be copied (directory2)
- Filename of the copy (filename2)

Here is the example of securely copying the file “sample.m” from my laptop home directory to a KIPAC computer

```
% -bash-4.1$ scp sample.m
```

```
Richards-MacBook-Air-3:Documents richardanantuahome$ scp mathrun.sh ranantua@1xx:~/
```

(securely copies mathrun.sh from present working directory (Documents richardanantuahome) to user ranantua at IP address)

Another example of copying a file from a KIPAC computer to my local computer using a Bash shell

```
>scp ranantua@ki-jmck.slac.stanford.edu:
```

```
/data1/ranantua/runlocaldipole3dfiducial/idumps
```

```
/fieldline1005.cart.bin.boxzh100.box256x256x256.out20.modelrunlocaldipole3dfiducial.txt
```

```
/Users/richardanantuahome/Documents
```

% Editing File w.Midnight Commander and Submitting Job Using Bsub

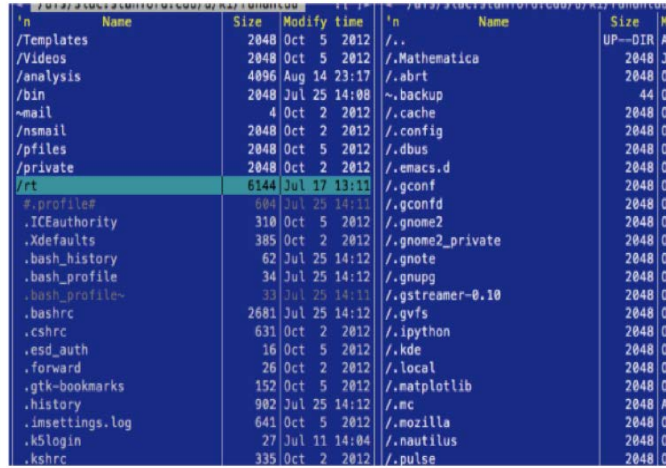
To enter Midnight Commander, a program enabling one to edit files by typing in a subshell,

```
-bash-4.1$ mc
```

An example of editing a file to change the name of the user in the filename is illustrated below:

–Within Midnight Commander

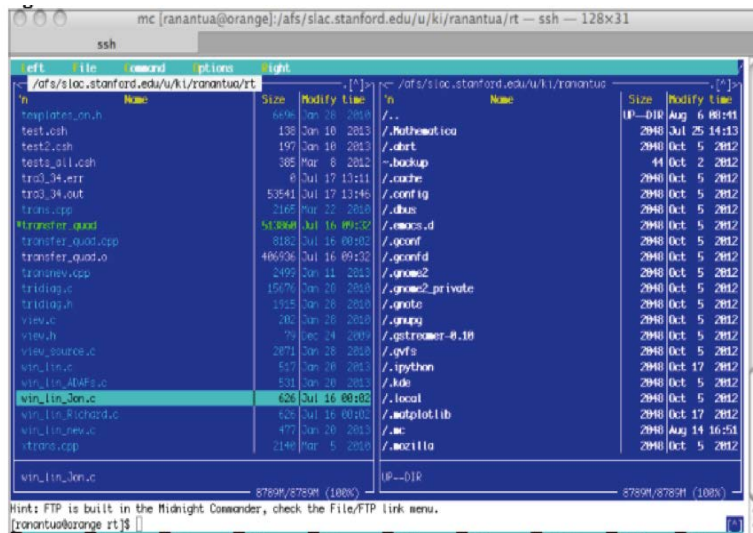
Scroll down using the down arrow until the highlight is on `rt` (see Figure 3) and press [Enter]



Size	Modify time	Name
2048	Oct 5 2012	/Templates
2048	Oct 5 2012	/Videos
4096	Aug 14 23:17	/analysis
2048	Jul 25 14:08	/bin
4	Oct 2 2012	~mail
2048	Oct 2 2012	/nsmail
2048	Oct 5 2012	/pfiles
2048	Oct 2 2012	/private
6144	Jul 17 13:11	rt
604	Jul 25 14:11	.profile
310	Oct 5 2012	.ICEauthority
385	Oct 2 2012	.Xdefaults
62	Jul 25 14:12	.bash_history
34	Jul 25 14:12	.bash_profile
33	Jul 25 14:11	.bash_profile~
2681	Jul 25 14:12	.bashrc
631	Oct 2 2012	.cshrc
16	Oct 5 2012	.esd_auth
26	Oct 2 2012	.forward
152	Oct 5 2012	.gtk-bookmarks
902	Jul 25 14:12	.history
641	Oct 5 2012	.imsettings.log
27	Jul 11 14:04	.k5login
335	Oct 2 2012	.kshrc

Figure B.3: Location of `rt` in midnight commander.

In Midnight Commander's `rt`, scroll down to `win.lin_Jon.c` (see Figure 4) and to edit this file, press [fn]+[F4] (see Figure 5)



Size	Modify time	Name
6496	Jan 28 2013	templates.cn.h
138	Jan 10 2013	test1.csh
197	Jan 10 2013	test2.csh
385	Mar 8 2012	test3_all.csh
8	Jul 17 13:11	tro3_34.err
53541	Jul 17 13:14	tro3_34.out
2165	Mar 22 2013	trans.csh
513948	Jul 16 09:02	transfer_quad
8182	Jul 16 09:02	transfer_quad.csh
406996	Jul 16 09:02	transfer_quad.o
2499	Jan 11 2013	transnew.csh
15676	Jan 28 2013	tridiag.c
1515	Jan 28 2013	tridiag.h
20	Jan 28 2013	view.c
79	Dec 24 2009	view.h
2071	Jan 28 2013	view_source.c
517	Jan 28 2013	win_lin.c
531	Jan 28 2013	win_lin_4DAs.c
626	Jul 16 00:02	win_lin_Jon.c
628	Jul 16 00:02	win_lin_Richard.c
477	Jan 28 2013	win_lin_new.c
2148	Mar 5 2010	trans.csh

Figure B.4: Location of `win.lin_Jon.c` in Midnight Commander.

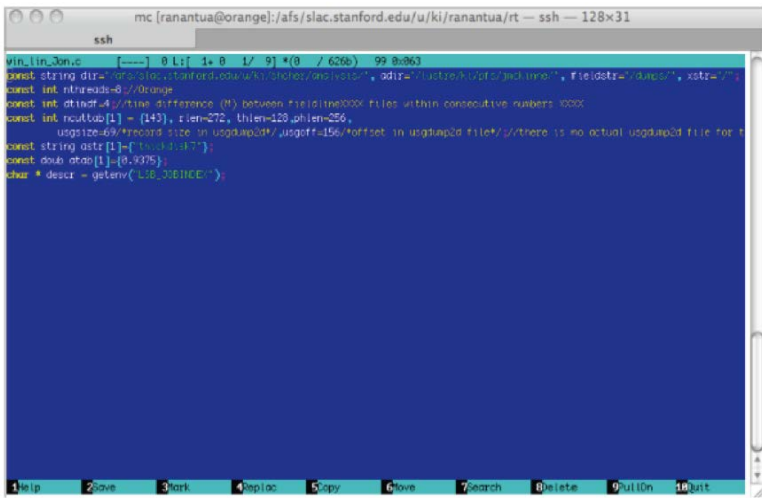


Figure B.5: Inside the file win_lin_Jon.c in Midnight Commander

–Make the change “shcher“ \rightarrow “ranantua” and press [fn]+[F2] to save the change. You will see Figure 6 asking you to confirm the save

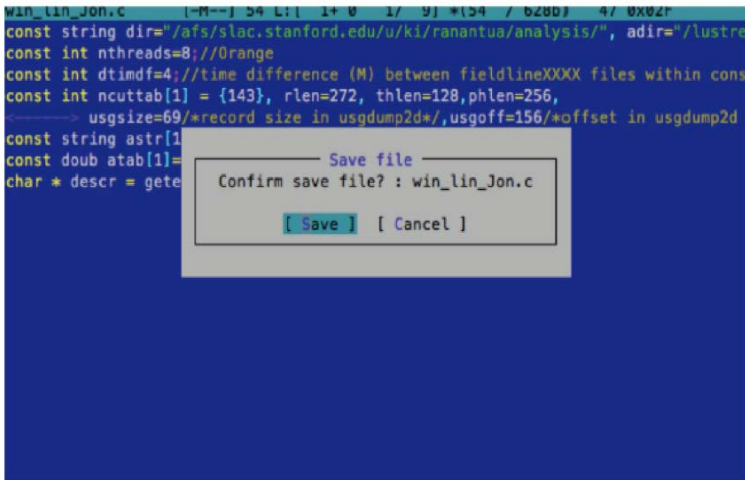


Figure B.6: Saving a file with Midnight Commander.

–Press [Enter] – Escape the screen by pressing the Quit command [fn]+[F10] 4.) In the folder “rt”, compile the code [ranantua@orange rt]\$ *make -B* The result should be Figure 7

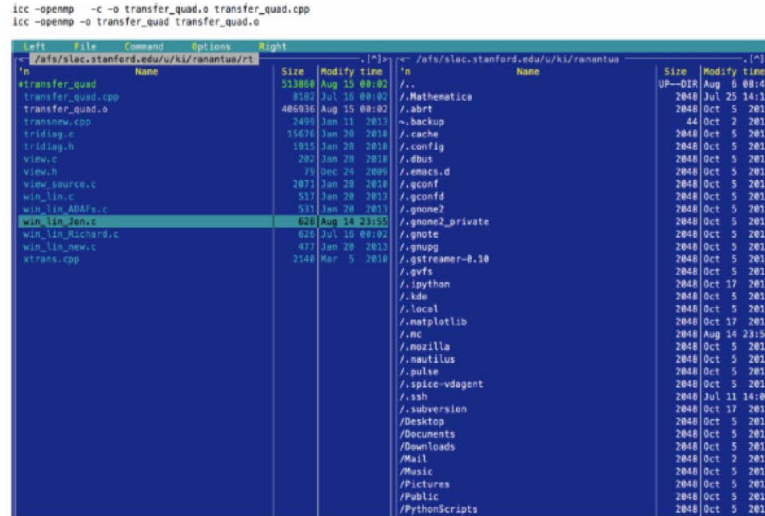


Figure B.7: Directory in Midnight Commander.

5.) – Make the change (see Figure 8) “roman@astro.umd.edu” → “ranantua@stanford.edu” and press [fn]+[F2] to save the change. You will see Figure 7 asking you to confirm the save

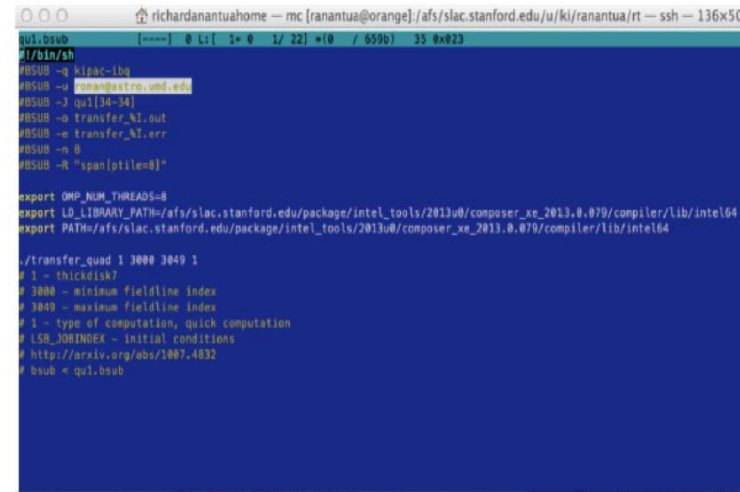


Figure B.8: Modifying q1.bsub file within Midnight Commander.

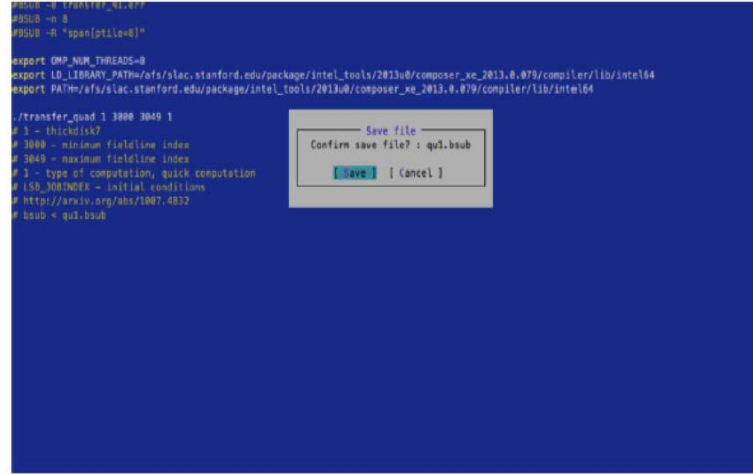


Figure B.9: Saving modified q1.bsub file within Midnight Commander.

–Press [Enter] – Escape the screen by pressing the Quit command [fn]+[F10] 6.) Submit the job to kipac-ibq by doing `bsub [ranantua@orange rt]$ bsub < qu1.bsub`

The result should be:

Job < 295619 > is submitted to queue <kipac-ibq>.

Using UNIX on a Cluster

% Running Jobs in Parallel on a Supercomputer

To run a command several times for different files in parallel on a supercomputing cluster, place (nohup COMMAND &) around the command for each file except the last one and press enter each time.

Example

`ranantua@ki-jmck:/data1/ranantua$ (nohup sh howtouse_joninterp.sh 1011 0 &)`

`ranantua@ki-jmck:/data1/ranantua$ nohup : appending output to 'nohup.out'`

`(nohup sh howtouse_joninterp.sh 1012 0 &)`

`ranantua@ki-jmck:/data1/ranantua$ nohup : appending output to 'nohup.out'`

`(nohup sh howtouse_joninterp.sh 1013 0 &)`

`nohup sh howtouse_joninterp.sh 1020 0`

`nohup: ignoring input and appending output to 'nohup.out'`

UNIX Appendix References

- [1] Retrieved Jan 5, 2014 from <http://en.wikipedia.org/wiki/Unix>
- [2] Anantua, R. (May 1, 2014). Linux vs. Windows (B). Harvard Business School. Retrieved May 17, 2014 from <https://drive.google.com/?tab=mo&authuser=0#folders/0B4x-8qMgWLG1NWRLSkhrYm9iTjg>
- [3] Knottenbelt, W. (2001). Introduction to UNIX: Ch. 2. Imperial College London. Retrieved Jan 5, 2014 from <http://www.doc.ic.ac.uk/~wjk/UnixIntro/Lecture2.html>
- [4] Johnson, C. (2006). Learn UNIX in 10 min, version 1.3. Free Engineer. Retrieved Jan 8, 2014 from <http://freeengineer.org/learnUNIXin10minutes.html>
- [5] Wikipedia. (n.d.). Chown. Retrieved Jan 5, 2014 from <http://en.wikipedia.org/wiki/Chown>
- [6] Indiana University Information Technology Services. (December 12, 2012). In Unix, how do I use SCP to securely transfer files between two computers? Retrieved Feb 12, 2014 from <https://kb.iu.edu/data/agye.html>

B.2 Python Guide for Observing Jet Simulations

Python Guide for Observing Jet Simulations

What is Python?

Python Tips

Python Help?

Frequently Performed Python Operations for Observing Jets Project

Reading Binary File

Reading Header and Body of Binary Datablock

Plotting Physical Quantities Using Matplotlib and Mayavi Packages

Contour Plot

Plot3D

Python Guide References

#What is Python

Python is a general-purpose, high-level programming language supporting object-oriented, imperative and functional programming styles [1]. Python is well-interfaced for reading potentially faster code, e.g., C, but itself is slow.

#Python Tips

One can run Python from Terminal shell using the command

```
ipython -pylab
```

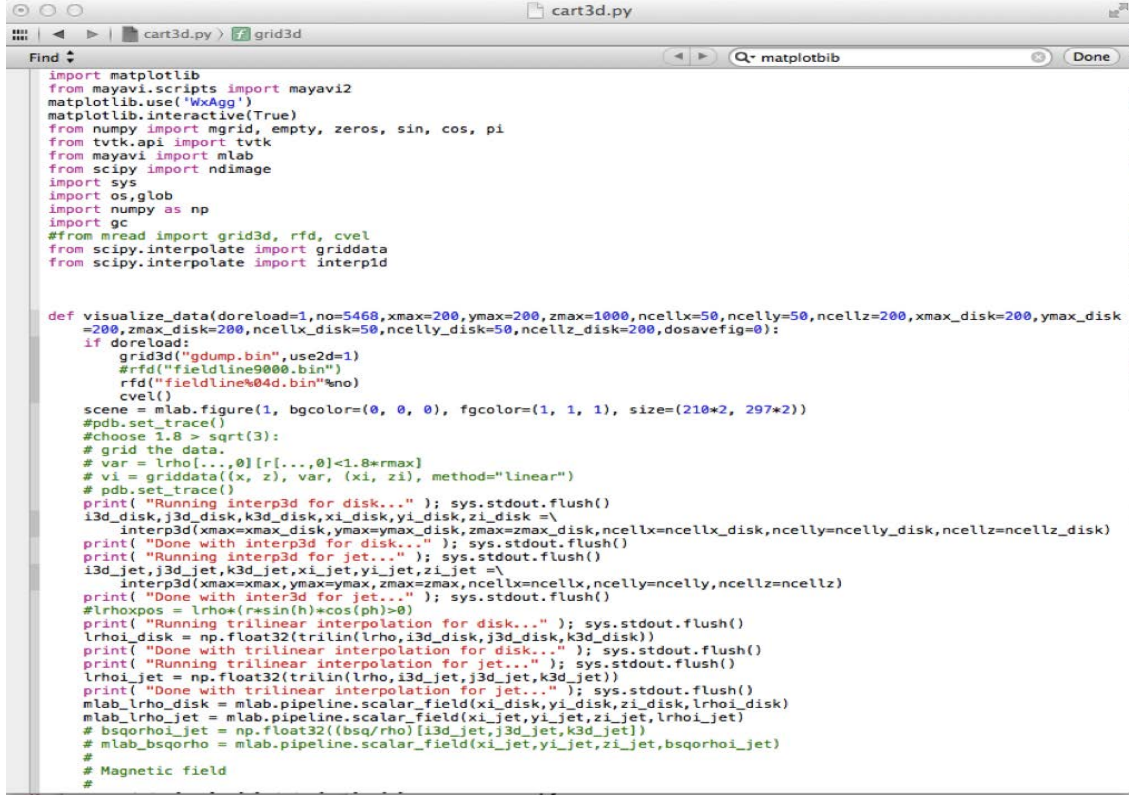
if which Python is known (if there aren't duplicates of the application Python)

#Python Help?

```
help([object])
```

#Example of Running a Jet Movie Using Python

Having downloaded a Python file `cart3d.py` (See Figure B.10)



```

import matplotlib
from mayavi.scripts import mayavi2
matplotlib.use('WxAgg')
matplotlib.interactive(True)
from numpy import mgrid, empty, zeros, sin, cos, pi
from tvtk.api import tvtk
from mayavi import mlab
from scipy import ndimage
import sys
import os, glob
import numpy as np
import gc
# from mread import grid3d, rfd, cvel
from scipy.interpolate import griddata
from scipy.interpolate import interp1d

def visualize_data(doreload=1, no=5468, xmax=200, ymax=200, zmax=1000, ncellx=50, ncelly=50, ncellz=200, xmax_disk=200, ymax_disk=200, zmax_disk=200, ncellx_disk=50, ncelly_disk=50, ncellz_disk=200, dosavefig=0):
    if doreload:
        grid3d("gdump.bin", use2d=1)
        # rfd("fieldline9000.bin")
        rfd("fieldline%04d.bin"%no)
        cvel()
    scene = mlab.figure(1, bgcolor=(0, 0, 0), fgcolor=(1, 1, 1), size=(210*2, 297*2))
    # pdb.set_trace()
    # choose 1.8 > sqrt(3):
    # grid the data.
    # var = lrho[...][r[...][0]<1.8*rmax]
    # v1 = griddata((x, z), var, (xi, zi), method="linear")
    # pdb.set_trace()
    print( "Running interp3d for disk..." ); sys.stdout.flush()
    i3d_disk, j3d_disk, k3d_disk, xi_disk, yi_disk, zi_disk = \
        interp3d(xmax=xmax_disk, ymax=ymax_disk, zmax=zmax_disk, ncellx=ncellx_disk, ncelly=ncelly_disk, ncellz=ncellz_disk)
    print( "Done with interp3d for disk..." ); sys.stdout.flush()
    print( "Running interp3d for jet..." ); sys.stdout.flush()
    i3d_jet, j3d_jet, k3d_jet, xi_jet, yi_jet, zi_jet = \
        interp3d(xmax=xmax, ymax=ymax, zmax=zmax, ncellx=ncellx, ncelly=ncelly, ncellz=ncellz)
    print( "Done with interp3d for jet..." ); sys.stdout.flush()
    # lrho_xpos = lrho*(r*sin(h)+cos(ph)>0)
    print( "Running trilinear interpolation for disk..." ); sys.stdout.flush()
    lrhoi_disk = np.float32(trilin(lrho, i3d_disk, j3d_disk, k3d_disk))
    print( "Done with trilinear interpolation for disk..." ); sys.stdout.flush()
    print( "Running trilinear interpolation for jet..." ); sys.stdout.flush()
    lrhoi_jet = np.float32(trilin(lrho, i3d_jet, j3d_jet, k3d_jet))
    print( "Done with trilinear interpolation for jet..." ); sys.stdout.flush()
    mlab.lrho_disk = mlab.pipeline.scalar_field(xi_disk, yi_disk, zi_disk, lrhoi_disk)
    mlab.lrho_jet = mlab.pipeline.scalar_field(xi_jet, yi_jet, zi_jet, lrhoi_jet)
    # bsqorhoi_jet = np.float32((bsq/rho)[i3d_jet, j3d_jet, k3d_jet])
    # mlab.bsqorho = mlab.pipeline.scalar_field(xi_jet, yi_jet, zi_jet, bsqorhoi_jet)
    #
    # Magnetic field

```

Figure B.10: A jet simulation file, cart3d.py runs faster on smaller simulation regions (the size of which can be adjusted by changing $xmax = 200$, $ymax = 200$ and $zmax = 1000$ above).

to run a GRMHD simulation and simulation data in a099.bin, here is how I ran it on my MacBook Air. A possible directory structure to run this is as follows:

Place “gdump.bin”

and

“fieldline5468.bin”

in a folder called “dumps”,

and “dumps” in a directory with

cart3d.py

I chose /Users/richardanantuahome/Downloads/ as the directory with cart3d.py and dumps

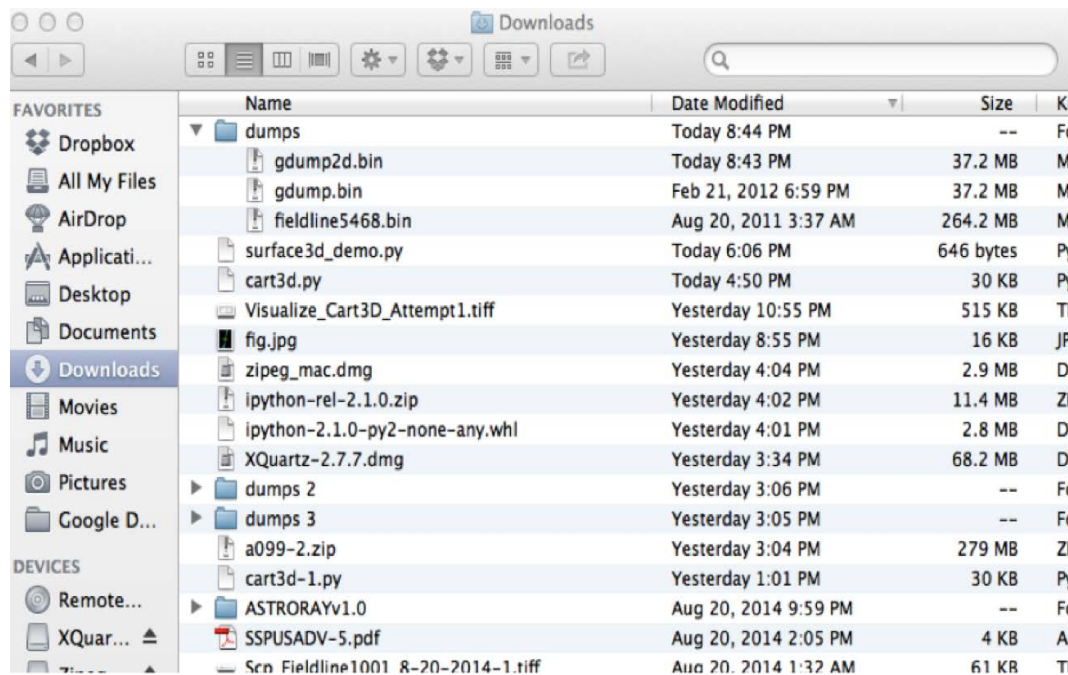


Figure B.11: This directory structure for will allow one to run a Python movie.

The command

```
ipython --pylab
```

previously failed because I had several versions of Python installed on my computer and none of them had a current subscription under which I could install Mayavi. Setting

which ipython

to the version installed through Canopy, renewing my subscription and getting Mayavi enabled me to do from Terminal

```

Last login: Fri Aug 22 20:01:59 on ttys010
dn51sk0k:~ richardanantuahome$ pwd
/Users/richardanantuahome
dn51sk0k:~ richardanantuahome$ cd ~/Downloads
dn51sk0k:Downloads richardanantuahome$ ipython --pylab
Python 2.7.3 | 64-bit | (default, Aug 8 2013, 05:37:06)
Type "copyright", "credits" or "license" for more information.

IPython 2.2.0 -- An enhanced Interactive Python.
?                -> Introduction and overview of IPython's features.
%quickref        -> Quick reference.
help             -> Python's own help system.
object?         -> Details about 'object', use 'object??' for extra details.
Using matplotlib backend: MacOSX

In [1]: pwd
Out[1]: u'/Users/richardanantuahome/Downloads'

In [2]: run -i ~/Downloads/cart3d.py
/Users/richardanantuahome/Library/Enthought/Canopy_64bit/User/lib/python2.7/site-packages/matplotlib/__init__.py:1155: UserWarning: This call to matplotlib.use()
) has no effect
because the backend has already been chosen;
matplotlib.use() must be called *before* pylab, matplotlib.pyplot,
or matplotlib.backends is imported for the first time.

warnings.warn(_use_error_msg)

In [3]: visualize_data()
Reading grid from dumps/gdump2d.bin ... done!
Opening fieldline5468.bin ...
Found 30 header items, reading them in and setting EP3=THETAROT=0.0

Loading gdetB data...
No data on gdetF, setting it to None.
No data on Bstag, setting it to B.
Running interp3d for disk...
Done with interp3d for disk...
Running interp3d for jet...
Done with interp3d for jet...
Running trilinear interpolation for disk...
Done with trilinear interpolation for disk...
Running trilinear interpolation for jet...
Done with trilinear interpolation for jet...
Running trilinear interpolation for Bx...
Done with trilinear interpolation for Bx...
Running trilinear interpolation for By...
Done with trilinear interpolation for By...
Running trilinear interpolation for Bz...
Done with trilinear interpolation for Bz...
Running volume rendering for disk...
Done with volume rendering of disk...
Running volume rendering for jet...
Done with volume rendering of jet...
Running rendering of streamLine #1...

```

Figure B.12: This code will allow one to run a Python movie.

which produced the movie (four of whose frames are shown from earliest to latest below)

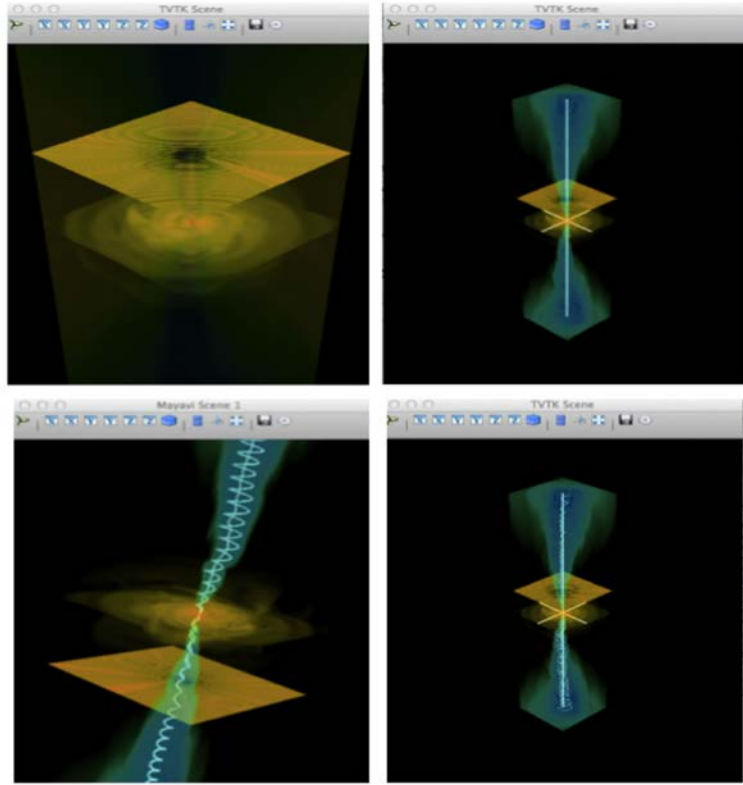
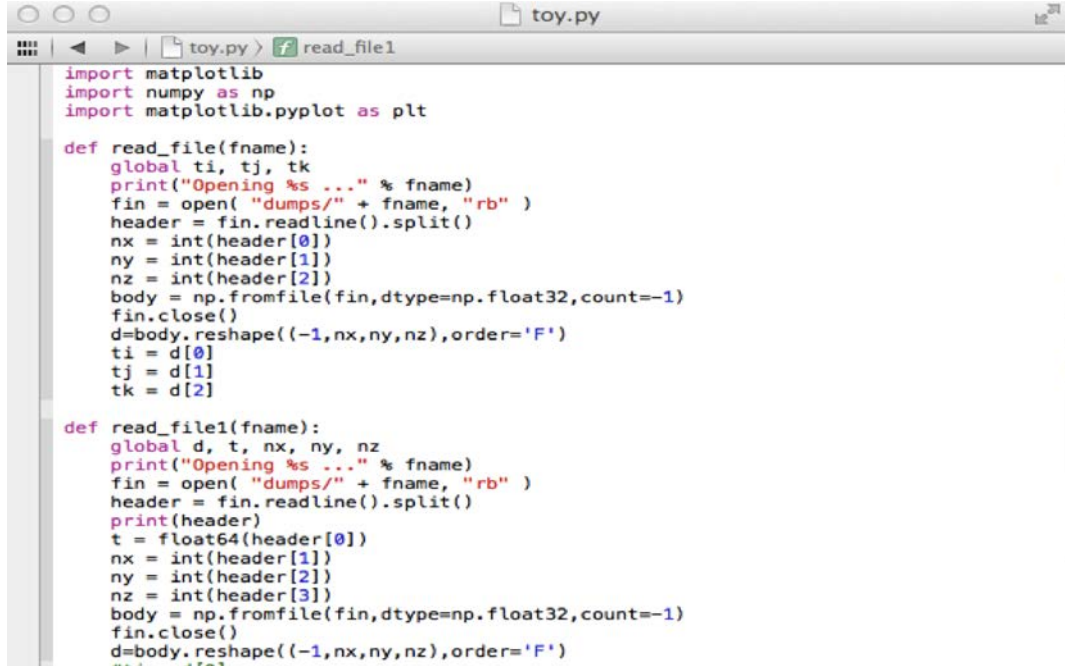


Figure B.13: Frames from Python movie of jet.

#Reading Header and Body of Binary Datablock

Using a Python editor such as Canopy, here is how we made a Python file for a data block reading routine.



```

toy.py
read_file1

import matplotlib
import numpy as np
import matplotlib.pyplot as plt

def read_file(fname):
    global ti, tj, tk
    print("Opening %s ..." % fname)
    fin = open( "dumps/" + fname, "rb" )
    header = fin.readline().split()
    nx = int(header[0])
    ny = int(header[1])
    nz = int(header[2])
    body = np.fromfile(fin, dtype=np.float32, count=-1)
    fin.close()
    d=body.reshape((-1,nx,ny,nz),order='F')
    ti = d[0]
    tj = d[1]
    tk = d[2]

def read_file1(fname):
    global d, t, nx, ny, nz
    print("Opening %s ..." % fname)
    fin = open( "dumps/" + fname, "rb" )
    header = fin.readline().split()
    print(header)
    t = float64(header[0])
    nx = int(header[1])
    ny = int(header[2])
    nz = int(header[3])
    body = np.fromfile(fin, dtype=np.float32, count=-1)
    fin.close()
    d=body.reshape((-1,nx,ny,nz),order='F')

```

Figure B.14: Python script for reading in a file .

Directory structure to run toy.py:

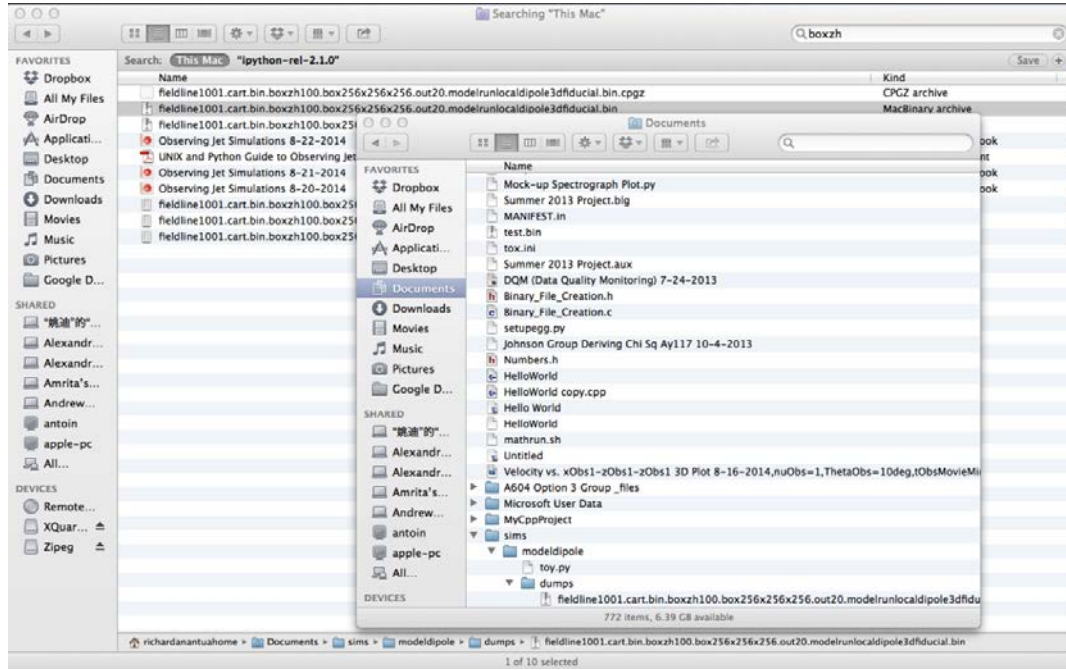
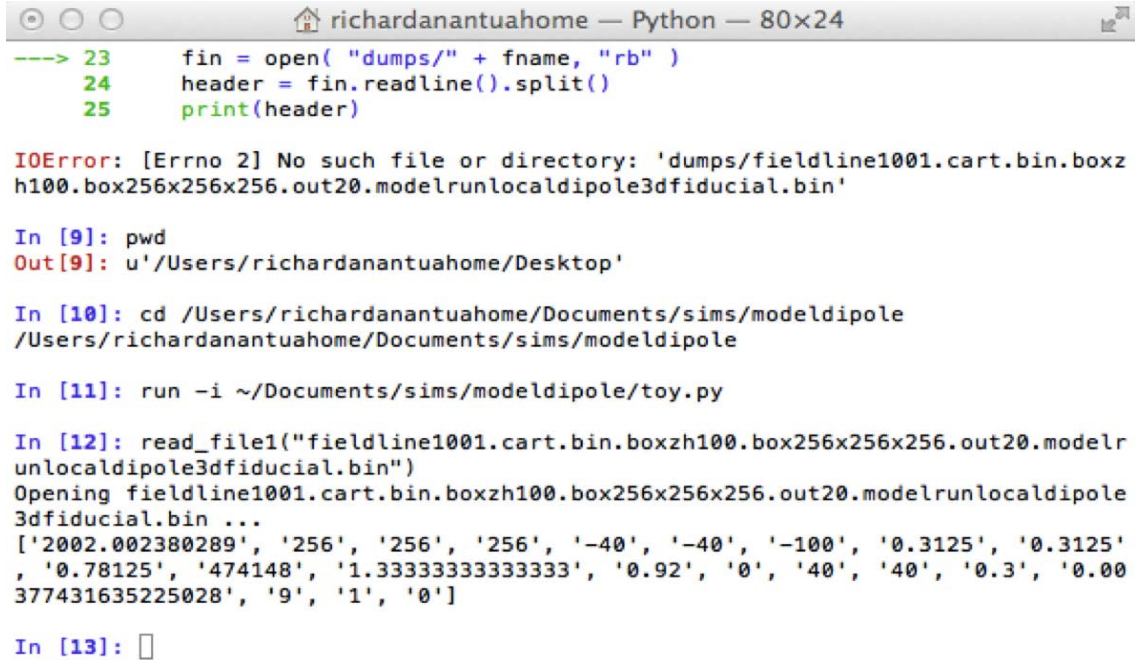


Figure B.15: Python script to run toy.py .

Terminal command to read the header of a fieldline file:



```

richardanantuahome — Python — 80x24

----> 23     fin = open( "dumps/" + fname, "rb" )
      24     header = fin.readline().split()
      25     print(header)

IOError: [Errno 2] No such file or directory: 'dumps/fieldline1001.cart.bin.boxzh100.box256x256x256.out20.modelrunlocaldipole3dfiducial.bin'

In [9]: pwd
Out[9]: u'/Users/richardanantuahome/Desktop'

In [10]: cd /Users/richardanantuahome/Documents/sims/modeldipole
/Users/richardanantuahome/Documents/sims/modeldipole

In [11]: run -i ~/Documents/sims/modeldipole/toy.py

In [12]: read_file1("fieldline1001.cart.bin.boxzh100.box256x256x256.out20.modelrunlocaldipole3dfiducial.bin")
Opening fieldline1001.cart.bin.boxzh100.box256x256x256.out20.modelrunlocaldipole3dfiducial.bin ...
['2002.002380289', '256', '256', '256', '-40', '-40', '-100', '0.3125', '0.3125', '0.78125', '474148', '1.3333333333333333', '0.92', '0', '40', '40', '0.3', '0.00377431635225028', '9', '1', '0']

In [13]: 

```

Figure B.16: Using Python Terminal to read the header from a file.

Terminal command to read the body of a fieldline file

```

In [8]: read_file1("fieldline1001.cart.bin.boxzh100.box256x256x256.out20.modelrunlocaldipole3dfiducial.bin")
Opening fieldline1001.cart.bin.boxzh100.box256x256x256.out20.modelrunlocaldipole3dfiducial.bin ...

In [9]: d.shape
Out[9]: (14, 256, 256, 256)

In [10]: run -i ~/Desktop/toy.py

In [11]: read_file1("fieldline1001.cart.bin.boxzh100.box256x256x256.out20.modelrunlocaldipole3dfiducial.bin")
Opening fieldline1001.cart.bin.boxzh100.box256x256x256.out20.modelrunlocaldipole3dfiducial.bin ...
['2002.002380289', '256', '256', '256', '-40', '-40', '-100', '0.3125', '0.3125', '0.70125', '474140', '1.3333333333333333', '0.92', '0', '40', '40', '0.3', '0.00377431635225028', '9', '1', '0']

In [12]: d
Out[12]:
array([[[[ 3.03468596e-06,  3.01895147e-06,  3.01173600e-06, ...,
           1.81369967e-06,  1.62459526e-06,  1.44242063e-06],
          [ 3.14353656e-06,  3.12950056e-06,  3.12066913e-06, ...,
           1.71789009e-06,  1.53036365e-06,  1.34681522e-06],
          [ 3.25533438e-06,  3.23981999e-06,  3.22925348e-06, ...,
           1.62242259e-06,  1.43651675e-06,  1.25399356e-06],
          ...,
          [ 2.63874813e-06,  2.73965793e-06,  2.79575784e-06, ...,
           1.76999083e-06,  1.60443119e-06,  1.44797480e-06],
          [ 2.75966158e-06,  2.84453404e-06,  2.88531419e-06, ...,
           1.85708700e-06,  1.68839085e-06,  1.52901589e-06],
          [ 2.88778301e-06,  2.95572659e-06,  2.98139321e-06, ...,
           1.94310405e-06,  1.77136815e-06,  1.61053606e-06]],
        [[ 3.13281453e-06,  3.12023462e-06,  3.11258555e-06, ...,
           1.74672391e-06,  1.55836790e-06,  1.37386269e-06],
          [ 3.24480129e-06,  3.23086601e-06,  3.22158212e-06, ...,
           1.64085101e-06,  1.46700708e-06,  1.27067170e-06]]]])

```

Figure B.17: Using Python Terminal to read the body from a file.

#Plotting Physical Quantities Using Matplotlib and Mayavi Packages

After downloading and installing Mayavi, Matplotlib, Numpy and SciPy, I ran toy.py using Terminal and made some Python contour and 3D density plots of datablock physical quantities.

With Matplotlib installed, one can use the following command to make a contour plot over a plane in the data array

```

In [13]: import matplotlib.pyplot as plt
In [14]: plt.contour(d[0,:,128,:].T)
Out[14]: <matplotlib.contour.QuadContourSet instance at 0x1507bbd40>

```

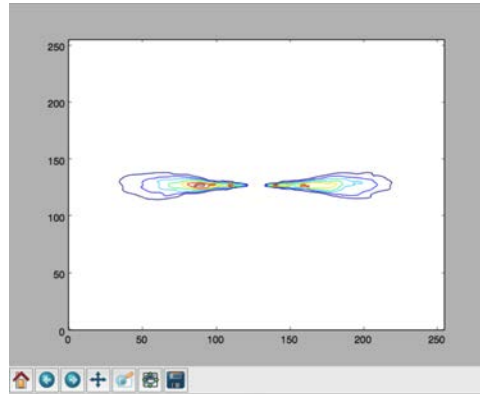


Figure B.18: Code to run contour plot of the scalar field $d[0]$ at $t_{\text{Gal}} = 1001 \times 2M$ and the 128th y-lattice point over the entire 256 x-values and 256 z-values (light travel time effects not considered here). The shorthand “:” indicates plot over all lattice values in a particular direction.

```

In [43]: import numpy as np
In [44]: delta = 1
In [45]: x = np.arange(0, 127, delta)
In [46]: y = np.arange(128, 256, delta)
In [47]: X,Y = np.meshgrid(x,y)
In [48]: plt.contour(d[0,X,Y,128])
Out[48]: <matplotlib.contour.QuadContourSet instance at 0x1555574d0>

```

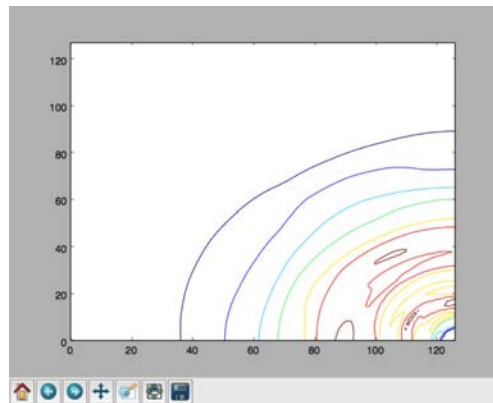


Figure B.19: Code to run contour plot of the scalar field $d[0]$ at $t_{\text{Gal}} = 1001 \times 2M$ and the 128th y-lattice point on the upper left quadrant of the central xy slice of the simulation region.

```

richardanantuahome — Python — 117x34
Last login: Sun Aug 24 15:45:58 on ttys010
dn51sk0k:~ richardanantuahome$ ipython --pylab
Python 2.7.3 | 64-bit | (default, Aug 8 2013, 05:37:06)
Type "copyright", "credits" or "license" for more information.

IPython 2.2.0 -- An enhanced Interactive Python.
?                -> Introduction and overview of IPython's features.
%quickref        -> Quick reference.
help             -> Python's own help system.
object?         -> Details about 'object', use 'object??' for extra details.
Using matplotlib backend: MacOSX

In [1]: cd /Users/richardanantuahome/Documents/sims/modeldipole
/Users/richardanantuahome/Documents/sims/modeldipole

In [2]: from mayavi import mlab

In [3]: run -i toy.py

In [4]: read_file1("fieldline1001.cart.bin.boxzh100.box256x256x256.out20.modelrunlocaldipole3dfiducial.bin")
Opening fieldline1001.cart.bin.boxzh100.box256x256x256.out20.modelrunlocaldipole3dfiducial.bin ...
['2002.002380289', '256', '256', '256', '-40', '-40', '-100', '0.3125', '0.3125', '0.78125', '474148', '1.333333333333333', '0.92', '0', '40', '40', '0.3', '0.00377431635225028', '9', '1', '0']

In [5]: mlab.pipeline.volume(mlab.pipeline.scalar_field(np.log10(d[0])))
Out[5]: <mayavi.modules.volume.Volume at 0x116ace530>

In [6]: 2014-08-24 16:05:15.561 Python[1144:f0f] -_continuousScroll is deprecated for NSScrollWheel. Please use -hasPreciseScrollingDeltas.
2014-08-24 16:05:15.567 Python[1144:f0f] -deviceDeltaX is deprecated for NSScrollWheel. Please use -scrollingDeltaX.
2014-08-24 16:05:15.567 Python[1144:f0f] -deviceDeltaY is deprecated for NSScrollWheel. Please use -scrollingDeltaY.
In [6]:

```

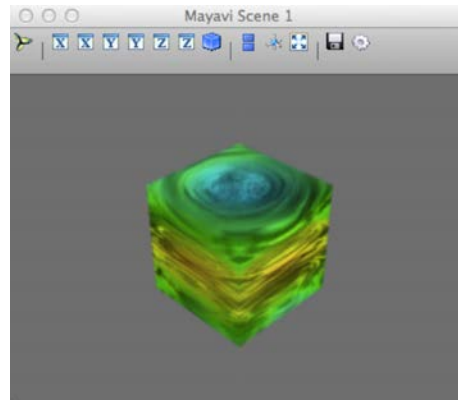


Figure B.20: Code to run 3D plot of the scalar field $d[0]$ at $t_{\text{Gal}} = 1001x2M$ (light travel time effects not considered here).

Python Appendix References

- [1] Wikipedia. (n.d.). Python (programming language). Retrieved Aug 25, 2014 from http://en.wikipedia.org/wiki/Python_%28programming_language%29

Bibliography

- [1] A. A. Abdo, M. Ackermann, M. Ajello, L. Baldini, J. Ballet, G. Barbiellini, D. Bastieri, K. Bechtol, R. Bellazzini, B. Berenji, and the Fermi LAT Collaboration. Fermi Large Area Telescope Observations of Markarian 421: The Missing Piece of its Spectral Energy Distribution. *The Astrophysical Journal*, 736:131, August 2011.
- [2] B. S. Acharya, M. Actis, T. Aghajani, G. Agnetta, J. Aguilar, F. Aharonian, M. Ajello, A. Akhperjanian, M. Alcubierre, J. Aleksić, and e. a. Introducing the CTA concept. *Astroparticle Physics*, 43:3–18, March 2013.
- [3] M. Ackermann, M. Ajello, W. B. Atwood, L. Baldini, and The Fermi LAT Collaboration. The Third Catalog of Active Galactic Nuclei Detected by the Fermi Large Area Telescope. *The Astrophysical Journal*, 810:14, September 2015.
- [4] K. Akiyama, R.-S. Lu, V. L. Fish, S. S. Doeleman, A. E. Broderick, J. Dexter, K. Hada, M. Kino, H. Nagai, M. Honma, M. D. Johnson, J. C. Algaba, K. Asada, C. Brinkerink, R. Blundell, G. C. Bower, R. Cappallo, G. B. Crew, M. Dexter, S. A. Dzib, R. Freund, P. Friberg, M. Gurwell, P. T. P. Ho, M. Inoue, T. P. Krichbaum, L. Loinard, D. MacMahon, D. P. Marrone, J. M. Moran, M. Nakamura, N. M. Nagar, G. Ortiz-Leon, R. Plambeck, N. Pradel, R. A. Primiani, A. E. E. Rogers, A. L. Roy, J. SooHoo, J.-L. Tavares, R. P. J. Tilanus, M. Titus, J. Wagner, J. Weintroub, P. Yamaguchi, K. H. Young, A. Zensus, and L. M. Ziurys. 230 GHz VLBI Observations of M87: Event-horizon-scale Structure during an Enhanced Very-high-energy γ -Ray State in 2012. *The Astrophysical Journal*, 807:150, July 2015.
- [5] R. Anantua and O. K. Baker. TeV gamma rays from distant BL Lacs and photon-paraphoton kinetic mixing. *Physics Letters B*, 690:25–28, June 2010.
- [6] U. Barres de Almeida. Status of the Cherenkov telescope array project. In *American Institute of Physics Conference Series*, volume 1693 of *American Institute of Physics Conference Series*, page 060005, December 2015.
- [7] V. Berestetskii, E. Lifshitz, and L. Pitaevskii. *Quantum Electrodynamics*, volume 4. Elsevier, The address, 1982.

- [8] J. A. Biretta, W. B. Sparks, and F. Macchetto. Hubble Space Telescope Observations of Superluminal Motion in the M87 Jet. *The Astrophysical Journal*, 520:621–626, August 1999.
- [9] J. P. Blakeslee, A. Jordán, S. Mei, P. Côté, L. Ferrarese, L. Infante, E. W. Peng, J. L. Tonry, and M. J. West. The ACS Fornax Cluster Survey. V. Measurement and Recalibration of Surface Brightness Fluctuations and a Precise Value of the Fornax-Virgo Relative Distance. *The Astrophysical Journal*, 694:556–572, March 2009.
- [10] R. D. Blandford and A. Levinson. Pair cascades in extragalactic jets. 1: Gamma rays. *The Astrophysical Journal*, 441:79–95, March 1995.
- [11] R. D. Blandford and R. L. Znajek. Electromagnetic extraction of energy from Kerr black holes. *Monthly Notices of the Royal Academy of Sciences*, 179:433–456, May 1977.
- [12] M. Boettcher, D. E. Harris, and H. Krawczynski. *Relativistic Jets from Active Galactic Nuclei*. January 2012.
- [13] M. Böttcher. Leptonic jet models of blazars: Broadband spectra and spectral variability. In B. L. Dingus, M. H. Salamon, and D. B. Kieda, editors, *American Institute of Physics Conference Series*, volume 515 of *American Institute of Physics Conference Series*, pages 31–40, June 2000.
- [14] W. Brinkmann, S. A. Laurent-Muehleisen, W. Voges, J. Siebert, R. H. Becker, M. S. Brotherton, R. L. White, and M. D. Gregg. Radio and X-ray bright AGN: the ROSAT - FIRST correlation. *Astronomy and Astrophysics*, 356:445–462, April 2000.
- [15] A. E. Broderick and A. Loeb. Imaging the Black Hole Silhouette of M87: Implications for Jet Formation and Black Hole Spin. *The Astrophysical Journal*, 697:1164–1179, June 2009.
- [16] A. E. Broderick and J. C. McKinney. Parsec-scale Faraday Rotation Measures from General Relativistic Magnetohydrodynamic Simulations of Active Galactic Nucleus Jets. *The Astrophysical Journal*, 725:750–773, December 2010.
- [17] J. A. Castro-Almazán, C. Muñoz-Tuñón, R. Sanz, R. García-López, I. Puerto, A. M. Varela, and M. Serra. Application of climatological monitoring for the candidate CTA site at Izaña (Tenerife). *Journal of Physics Conference Series*, 595(1):012008, April 2015.
- [18] H. D. Curtis. Descriptions of 762 Nebulae and Clusters Photographed with the Crossley Reflector. *Publications of Lick Observatory*, 13:9–42, 1918.
- [19] S. S. Doeleman, V. L. Fish, D. E. Schenck, C. Beaudoin, R. Blundell, G. C. Bower, A. E. Broderick, R. Chamberlin, R. Freund, P. Friberg, M. A. Gurwell, P. T. P. Ho, M. Honma, M. Inoue, T. P. Krichbaum, J. Lamb, A. Loeb, C. Lonsdale, D. P. Marrone, J. M. Moran, T. Oyama, R. Plambeck, R. A. Primiani, A. E. E. Rogers, D. L. Smythe, J. SooHoo, P. Strittmatter, R. P. J.

- Tilanus, M. Titus, J. Weintraub, M. Wright, K. H. Young, and L. M. Ziurys. Jet-Launching Structure Resolved Near the Supermassive Black Hole in M87. *Science*, 338:355, October 2012.
- [20] V. L. Fish, K. Akiyama, K. L. Bouman, A. A. Chael, M. D. Johnson, S. S. Doeleman, L. Blackburn, J. F. C. Wardle, W. T. Freeman, and the Event Horizon Telescope Collaboration. Observing—and Imaging—Active Galactic Nuclei with the Event Horizon Telescope. *ArXiv e-prints*, July 2016.
- [21] C. F. Gammie, J. C. McKinney, and G. Tóth. HARM: A Numerical Scheme for General Relativistic Magnetohydrodynamics. *The Astrophysical Journal*, 589:444–457, May 2003.
- [22] K. Gebhardt, J. Adams, D. Richstone, T. R. Lauer, S. M. Faber, K. Gültekin, J. Murphy, and S. Tremaine. The Black Hole Mass in M87 from Gemini/NIFS Adaptive Optics Observations. *The Astrophysical Journal*, 729:119, March 2011.
- [23] N. Globus and A. Levinson. The collimation of magnetic jets by disc winds. *Monthly Notices of the Royal Academy of Sciences*, 461:2605–2615, September 2016.
- [24] F. Govoni and L. Feretti. Magnetic Fields in Clusters of Galaxies. *International Journal of Modern Physics D*, 13:1549–1594, 2004.
- [25] K. Hada, A. Doi, M. Kino, H. Nagai, Y. Hagiwara, and N. Kawaguchi. An origin of the radio jet in M87 at the location of the central black hole. *Nature*, 477:185–187, September 2011.
- [26] K. Hada, M. Kino, A. Doi, H. Nagai, M. Honma, K. Akiyama, F. Tazaki, R. Lico, M. Giroletti, G. Giovannini, M. Orienti, and Y. Hagiwara. High-sensitivity 86 GHz (3.5 mm) VLBI Observations of M87: Deep Imaging of the Jet Base at a Resolution of 10 Schwarzschild Radii. *The Astrophysical Journal*, 817:131, February 2016.
- [27] R. C. Hartman, M. Böttcher, G. Aldering, H. Aller, M. Aller, D. E. Backman, T. J. Balonek, D. L. Bertsch, S. D. Bloom, H. Bock, P. Boltwood, M. T. Carini, W. Collmar, G. De Francesco, E. C. Ferrara, W. Freudling, W. K. Gear, P. B. Hall, J. Heidt, P. Hughes, S. D. Hunter, S. Jogee, W. N. Johnson, G. Kanbach, S. Katajainen, M. Kidger, T. Kii, M. Koskimies, A. Kraus, H. Kubo, O. Kurtanidze, L. Lanteri, A. Lawson, Y. C. Lin, U. Lisenfeld, G. Madejski, F. Makino, L. Maraschi, A. P. Marscher, J. P. McFarland, I. McHardy, H. R. Miller, M. Nikolashvili, K. Nilsson, J. C. Noble, G. Nucciarelli, L. Ostorero, E. Pian, T. Pursimo, C. M. Raiteri, W. Reich, R. Rekola, G. M. Richter, E. I. Robson, A. Sadun, T. Savolainen, A. Sillanpää, A. Smale, G. Sobrito, P. Sreekumar, J. A. Stevens, L. O. Takalo, F. Tavecchio, H. Teräsranta, D. J. Thompson, M. Tornikoski, G. Tosti, H. Ungerechts, C. M. Urry, E. Valtaoja, M. Villata, S. J. Wagner, A. E. Wehrle, and J. W. Wilson. Multiepoch Multiwavelength Spectra and Models for Blazar 3C 279. *THE Astrophysical Journal*, 553:683–694, June 2001.

- [28] J. Holder. Ground-Based Gamma Ray Astronomy. *Brazilian Journal of Physics*, 44:450–464, October 2014.
- [29] J. D. Jackson. *Classical Electrodynamics, 3rd Edition*. July 1998.
- [30] Y. Y. Kovalev, M. L. Lister, D. C. Homan, and K. I. Kellermann. The Inner Jet of the Radio Galaxy M87. *The Astrophysical Journal Letters*, 668:L27–L30, October 2007.
- [31] T. P. Krichbaum, D. A. Graham, A. Witzel, J. A. Zensus, A. Greve, M. Grewing, M. Bremer, S. Doeleman, R. B. Phillips, A. E. E. Rogers, H. Fagg, P. Strittmatter, and L. Ziurys. *Towards the Event Horizon: High Resolution VLBI Imaging of Nuclei of Active Galaxies*, page 189. Springer-Verlag, 2007.
- [32] Matt Lister. MOJAVE Time Lapse Movies of AGN Jets kernel description, 2015.
- [33] M. S. Longair. *High Energy Astrophysics*. February 2011.
- [34] R.-S. Lu, A. E. Broderick, F. Baron, J. D. Monnier, V. L. Fish, S. S. Doeleman, and V. Pankratius. Imaging the Supermassive Black Hole Shadow and Jet Base of M87 with the Event Horizon Telescope. *The Astrophysical Journal*, 788:120, June 2014.
- [35] L. Maraschi, G. Ghisellini, and A. Celotti. A jet model for the gamma-ray emitting blazar 3C 279. *The Astrophysical Journal Letters*, 397:L5–L9, September 1992.
- [36] A. P. Marscher and S. G. Jorstad. Rapid Variability of Gamma-ray Emission from Sites near the 43 GHz Cores of Blazar Jets. *ArXiv e-prints*, May 2010.
- [37] P. Marziani, J. W. Sulentic, D. Dultzin-Hacyan, M. Calvani, and M. Moles. Comparative Analysis of the High- and Low-Ionization Lines in the Broad-Line Region of Active Galactic Nuclei. *The Astrophysical Journal Supplement*, 104:37, May 1996.
- [38] J. C. McKinney and R. D. Blandford. Stability of relativistic jets from rotating, accreting black holes via fully three-dimensional magnetohydrodynamic simulations. *Monthly Notices of the Royal Astronomical Society*, 394:L126–L130, March 2009.
- [39] J. C. McKinney, A. Tchekhovskoy, and R. D. Blandford. General relativistic magnetohydrodynamic simulations of magnetically choked accretion flows around black holes. *Monthly Notices of the Royal Astronomical Society*, 423:3083–3117, July 2012.
- [40] M. Mościbrodzka, C. F. Gammie, J. C. Dolence, H. Shiokawa, and P. K. Leung. Radiative Models of SGR A* from GRMHD Simulations. *The Astrophysical Journal*, 706:497–507, November 2009.
- [41] R. Narayan and I. Yi. Advection-dominated Accretion: Underfed Black Holes and Neutron Stars. *The Astrophysical Journal*, 452:710, October 1995.

- [42] R. Narayan, I. Yi, and R. Mahadevan. Explaining the spectrum of Sagittarius A* with a model of an accreting black hole. *Nature*, 374:623–625, April 1995.
- [43] K. Nilsson, T. Pursimo, C. Villforth, E. Lindfors, and L. O. Takalo. The host galaxy of 3C 279. *Astronomy and Astrophysics*, 505:601–604, October 2009.
- [44] K.-I. Nishikawa, C. B. Hededal, P. E. Hardee, G. J. Fishman, C. Kouveliotou, and Y. Mizuno. 3-D Rpic Simulations of Relativistic Jets: Particle Acceleration, Magnetic Field Generation, and Emission. *Astrophysics and Space Science*, 307:319–323, January 2007.
- [45] V. S. Paliya, M. Böttcher, C. Diltz, C. S. Stalin, S. Sahayanathan, and C. D. Ravikumar. The Violent Hard X-Ray Variability of Mrk 421 Observed by NuSTAR in 2013 April. *The Astrophysical Journal*, 811:143, October 2015.
- [46] E. Pian, C. M. Urry, L. Maraschi, G. Madejski, I. M. McHardy, A. Koratkar, A. Treves, L. Chiappetti, P. Grandi, R. C. Hartman, H. Kubo, C. M. Leach, J. E. Pesce, C. Imhoff, R. Thompson, and A. E. Wehrle. Ultraviolet and Multiwavelength Variability of the Blazar 3C 279: Evidence for Thermal Emission. *The Astrophysical Journal*, 521:112–120, August 1999.
- [47] M. J. Rees. New Interpretation of Extragalactic Radio Sources. *Nature*, 229:312–317, January 1971.
- [48] A. Ricarte and J. Dexter. The Event Horizon Telescope: exploring strong gravity and accretion physics. *Monthly Notices of the Royal Academy of Sciences*, 446:1973–1987, January 2015.
- [49] J. L. Richards, W. Max-Moerbeck, V. Pavlidou, O. G. King, T. J. Pearson, A. C. S. Readhead, R. Reeves, M. C. Shepherd, M. A. Stevenson, L. C. Weintraub, L. Fuhrmann, E. Angelakis, J. A. Zensus, S. E. Healey, R. W. Romani, M. S. Shaw, K. Grainge, M. Birkinshaw, K. Lancaster, D. M. Worrall, G. B. Taylor, G. Cotter, and R. Bustos. Blazars in the Fermi Era: The OVRO 40 m Telescope Monitoring Program. *The Astrophysical Journal Supplement Series*, 194:29, June 2011.
- [50] G.B. Rybicki and A.P. Lightman. *Radiative Processes in Astrophysics*. A Wiley-Interscience publication. Wiley, 1979.
- [51] A. Sądowski, R. Narayan, A. Tchekhovskoy, D. Abarca, Y. Zhu, and J. C. McKinney. Global simulations of axisymmetric radiative black hole accretion discs in general relativity with a mean-field magnetic dynamo. *Monthly Notices of the Royal Academy of Sciences*, 447:49–71, February 2015.
- [52] N. I. Shakura and R. A. Sunyaev. Black holes in binary systems. Observational appearance. *Astronomy and Astrophysics*, 24:337–355, 1973.

- [53] R. V. Shcherbakov, R. F. Penna, and J. C. McKinney. Sagittarius A* Accretion Flow and Black Hole Parameters from General Relativistic Dynamical and Polarized Radiative Modeling. *The Astrophysical Journal*, 755:133, August 2012.
- [54] A. Tchekhovskoy and O. Bromberg. Three-dimensional relativistic MHD simulations of active galactic nuclei jets: magnetic kink instability and Fanaroff-Riley dichotomy. *Monthly Notices of the Royal*, 461:L46–L50, September 2016.
- [55] The Fermi LAT Collaboration: Ackermann e. a. Minute-timescale $\gtrsim 100$ MeV γ -Ray Variability during the Giant Outburst of Quasar 3C 279 Observed by Fermi-LAT in 2015 June. *Astrophysical Journal Letters*, 824:L20, June 2016.
- [56] E. Torresi and F. D’Ammand. Fermi LAT detection of a GeV flare from a possible new extragalactic gamma-ray source FERMI J1350-1140. *The Astronomer’s Telegram*, 3788, November 2011.
- [57] V. Vincenzo. FERMI/GLAST and the Future of High Energy Gamma Ray Astronomy. *SLAC eConference Proceedings*, 2008.
- [58] J. Wagner, A. L. Roy, T. P. Krichbaum, W. Alef, A. Bansod, A. Bertarini, R. Güsten, D. Graham, J. Hodgson, R. Märten, K. Menten, D. Muders, H. Rottmann, G. Tuccari, A. Weiss, G. Wieching, M. Wunderlich, J. A. Zensus, J. P. Araneda, O. Arriagada, M. Cantzler, C. Duran, F. M. Montenegro-Montes, R. Olivares, P. Caro, P. Bergman, J. Conway, R. Haas, J. Johansson, M. Lindqvist, H. Olofsson, M. Pantaleev, S. Buttaccio, R. Cappallo, G. Crew, S. Doleman, V. Fish, R.-S. Lu, C. Ruszczyk, J. SooHoo, M. Titus, R. Freund, D. Marrone, P. Strittmatter, L. Ziurys, R. Blundell, R. Primiani, J. Weintraub, K. Young, M. Bremer, S. Sánchez, A. P. Marscher, R. Chilson, K. Asada, and M. Inoue. First 230 GHz VLBI fringes on 3C 279 using the APEX Telescope. *Astronomy and Astrophysics*, 581:A32, September 2015.
- [59] R. C. Walker, C. Ly, W. Junor, and P. J. Hardee. A VLBA movie of the jet launch region in M87. *Journal of Physics Conference Series*, 131(1):012053, October 2008.
- [60] J. L. Walsh, A. J. Barth, L. C. Ho, and M. Sarzi. The M87 Black Hole Mass from Gas-dynamical Models of Space Telescope Imaging Spectrograph Observations. *The Astrophysical Journal*, 770:86, June 2013.
- [61] Chun-Cheng Wang and Hong-Yan Zhou. Determination of the intrinsic velocity field in the m87 jet. *Monthly Notices of the Royal Astronomical Society*, 395(1):301–310, 2009.